ISSP

ACTIVITY REPORT OF SYNCHROTRON RADIATION LABORATORY

2018

Preface

The Synchrotron Radiation Laboratory (SRL) of the Institute for Solid State Physics (ISSP) has been cooperating with the Synchrotron Radiation Research Organization of the University of Tokyo since 2006 to operate the BL07LSU soft X-ray beamline and experimental end-stations at SPring-8. The beamline has a 27-m-long polarization-controlled undulator and a monochromator covering the photon energy range from 250 eV to 2 keV with an average photon flux of 10^{12} photons/sec. As one of the central facilities for promoting advanced materials science and development of unique spectroscopic methods in the soft X-ray region, the SRL fully opened the beamline to public users in 2009. Since then, SRL staff members have played an essential role in promoting both domestic and international joint research. Three end-stations, a time-resolved photoelectron spectroscopy, a 3D nanoESCA, and a high-resolution soft x-ray emission spectroscopy stations, have the world’s best time resolution (~50 ps), spatial resolution (~70 nm), and energy resolution ($E/\Delta E \approx 10{,}000$), respectively. They have been permanently installed in the beamline to accept joint-research proposals, while a free-port station equipped with a focusing mirror is available to outside users. In 2018, an ambient-pressure *operando* X-ray photoemission spectroscopy station was promoted as one of the end-stations accepting joint-research proposals.

In addition to the cutting-edge activities using synchrotron radiation, SRL joined the Laser and Synchrotron Research (LASOR) Center as a member in 2012. Since then, we have promoted soft X-ray science using high-harmonic lasers in the vacuum ultra-violet and soft X-ray regions at the Kashiwa Campus E-building. In 2014, SRL constructed a new high-resolution laser spin- and angle-resolved photoelectron spectroscopy (SARPES) apparatus that is designed to provide high-energy and -angular resolutions and high-efficiency spin detection for various types of solids, such as spin-orbit coupled materials and ferromagnetic materials. Since FY 2015, the SARPES system has been open for users and accepting joint-research proposals.

Our goal is to provide users with a soft X-ray platform that uses both synchrotron radiation and high-harmonic lasers by strong collaboration with other LASOR group members.

June 30, 2019
Yoshihisa Harada
Director of SRL-ISSP

Activity Report 2018

TABLE OF CONTENTS

5 **Activities**

Synchrotron Radiation Experiments (SPring-8)

Experiments at E-labo

1. Status of Beamline BL07LSU at SPring-8

The University-of-Tokyo high-brilliance synchrotron soft X-ray outstation beamline BL07LSU at SPring-8 has been maintained by the permanent staff members with adjuncts for user operations. A scientific aim of the beamline is to promote advanced spectroscopy for solid state and soft (including bio) materials. There are four regular endstations: time-resolved soft X-ray spectroscopy (TR-SX spectroscopy), soft X-ray diffraction, 3D-scanning photoelectron microscope (3D nano-ESCA) and ultrahigh resolution soft X-ray emission spectroscopy (HORNET) that are open for users. There is also a free port station for users who bring their own experimental apparatus. In 2018, we have completed commissioning of the ambient pressure X-ray photoelectron spectroscopy station at the free port station and opened the system for general users.

The beamline BL07LSU is equipped with a segmented cross-type undulator. By using phase shifter among the undulator segments, a polarization control of soft X-ray was started since 2016. Circularly and linearly polarized soft X-rays at full energy range (250 – 2000 eV) have been available by tuning the permanent magnet type phase shifter. In 2018, we have introduced a soft X-ray chopper that can transmit only a selected pulse of the incident beam in order to improve signal to noise ratio of specific experiments like time-resolved spectroscopy of slow dynamics, operando spectroscopy under applied bias or to reduce radiation induced damages.

At the beamline endstations, various scientific researches were carried out by both the laboratory staffs and general users (G-type application). Below are brief introduction of recent activities at each station.

(1) Time-Resolved soft X-ray spectroscopy station (TR-SX spectroscopy)

The station is to perform time-resolved photoemission spectroscopy experiments by synchronizing the high-brilliant soft X-ray and the ultra-short laser pulses. A two-dimensional angle-resolved time-of-flight (ARTOF) analyzer has been equipped for the efficient time-resolved measurements and the measurement temperature can be controlled from 15 K to 1150K. The station adopts two different optical laser systems synchronized with synchrotron soft X-ray; low repetition rate and high pulse energy (1 kHz, mJ) and high repetition rate and low pulse energy (208 kHz, μJ). In addition, an optical parametric amplifier (OPA) has been installed for both laser systems to cover a wider spectrum range of optical laser.

In 2018, time-resolved photoelectron diffraction experiments were performed on a monatomic two-dimensional layer of Si, Silicene. Two-dimensional detection of photoelectron diffraction patterns and a chemical shift in high energy resolution measurements by ARTOF allow us to trace temporal evolution of Si atom positions in a site-specific manner.

Photo-excited carrier dynamics in a model organic phovoltaic system was studied using time-resolved soft X-ray photoelectron spectroscopy. Monolayer-thick *p*-type metal phthalocyanine (CuPc) and *n*-type fullerene (C_{60}) layers were deposited on a $TiO_2(110)$ surface. Electrons excited in the unoccupied states of CuPc and C_{60} are swiftly transferred to the conduction band of TiO_2 substrate, leaving the molecules in transient cationic states. The cationic states have long lifetime of the order of microseconds, suggesting that an electron-hole recombination is efficiently suppressed at the organic/TiO_2 interface.

(2) 3D-scanning photoelectron microscope (3D nano-ESCA)

3D-nano-ESCA can be used for sub-100 nm range microscopic 2D mapping and depth profile of the chemical structure of functional materials and devices.

In 2018, we have devised new technique enabling to probe the electronics states of buried interfaces of GaN-HEMT in academia-industry collaboration with Sumitomo Electric Industries, by combing 3D nano-ESCA with advanced device technologies. This work was published in Scientific Reports in 2018. As a joint research with Dr. Asakura and Dr. Hosono at AIST group, we also combined 3D nano-ESCA with optical microscope images, and studied Li ion diffusion mechanism in a μm sized SnO_2 wire and local Li insertion/extraction process in a $Li_4Ti_5O_{12}$ (LTO) negative electrode active material under operando (electrochemically operating) condition. The result on LTO was published in Journal of Electron Spectroscopy and Related Phenomena. As collaboration with Department of Materials Engineering, the University of Tokyo, we performed operando nano-spectroscopy on device structures of transition metal dichalcogenide tunnel field effect transistors (TMD-TFETs) and found difference in gate and drain voltage dependence of the potential distribution between MoS_2 on highly- and low- doped p^+-WSe_2. Furthermore, we also conducted academia-industry collaboration research on process-induced defects in SiC trench MOSFETs based on the previous results published in e-JSSNT in 2018.

(3) Ambient-pressure X-ray photoelectron spectroscopy (AP-XPS)

This station allows *Operando* observation of catalysts under reaction conditions using AP-XPS. The AP-XPS station was constructed in 2014 by an external funding (JST ACT-C project), and was opened to external users in 2018.

The AP-XPS system is equipped with a differentially pumped electron analyzer

(SPECS, PHOIBOS 150 NAP) and an ambient-pressure gas cell. XPS measurements can be performed both under ultrahigh vacuum and in near-ambient gas pressure up to 20 mbar. Catalytic activity is monitored by mass spectrometer, and simultaneous evaluation of adsorbate and catalyst electronic states is performed by AP-XPS. In addition to the experiments at the free port station using synchrotron soft X-ray, off-line experiments using a twin-anode X-ray source can be performed.

A variety of research projects are now in progress at the AP-XPS station: (i) Methanol synthesis on Cu-Zn catalysts, (ii) Sabatier reaction on Ni catalysts, (iii) H_2 adsorption/absorption in Pd nanoparticles and Pd alloys (PdAg and PdCu), (iv) CH_4 partial oxidation on Pd catalysts, (v) CO_2 adsorption on graphene support, (vi) band alignment at a semiconductor photoelectrode and electrolyte interface, (vii) development of time-resolved AP-XPS.

(4) Ultra high-resolution soft X-ray emission spectroscopy (HORNET)

The station is dedicated for soft X-ray emission (or resonant inelastic X-ray scattering: RIXS) spectroscopy measurements with ultrahigh-resolution ($E/\Delta E > 10{,}000$) and under various environmental conditions (gas, liquid, and solid). The number of applications to the HORNET station is increasing. In 2018, we have performed 15 collaborative research using the HORNET station: two S-type proposals, five proposals for molecular systems, four for condensed matter physics, and four for electrochemistry of batteries. In molecular systems, the behavior of water in a variety of circumstances was studied, such as water around disaccharide, water at the interface of biocompatible polymers, and hydration to plasma treated carbon nanotube and boron nitride. Jet system was installed in order to discuss pure vibrational spectra without the contribution from an X-ray filter. In condensed matter physics, characteristic experiments were carried out using the advantages of RIXS. Charge excitation due to hole doped at oxygen sites in $La_{2-x}Sr_xNiO_{4+\delta}$, $La_{2-2}xSr_{1+2x}Mn_3O_7$, and $La_{1-x}Sr_{1+x}MnO_4$ was investigated in comparison with $La_{2-x}Sr_xCuO_4$ using elementary selectivity of O *K*-edge RIXS. Photon-in/photon-out process of RIXS enabled to probe electronic structure change due to metal-insulator transition in Ca_2RuO_4 induced by electronic field. Angle-resolved RIXS allowed us to measure the dispersion of elementary excitation in VO_2 and resonant inelastic X-ray diffraction from $La_{1/3}Sr_{2/3}FeO_3$. In electrochemistry of batteries, we have continuously studied mechanism of charge/discharge process and explored new electrode materials by ex-situ and operand RIXS. In order to clarify the effect of charge transfer between metal and oxygen, oxygen-free electrolyte battery cell is being developed. In 2018, several results for condensed matter physics were published, such as Fe *L*-edge RIXS of FeS model complexes and low-spin ferrous and ferric iron complexes, V and Mn *L*-edge RIXS of half-metallic ferrimagnet Mn_2VAl, Cr *L*-edge RIXS of ruby, and Co *L*-edge RIXS of $LaCoO_3$.

(4) Free-port station

The station is equipped with a focusing mirror chamber, and users can connect their own experimental chambers. In 2018, the following experiments were performed: time resolved soft X-ray diffraction of $Ba_3CuSb_2O_9$; time resolved X-ray absorption spectroscopy of Eu compounds with valence fluctuations; N *K*-edge near-edge X-ray absorption fine structure of 2D organic hetero-bilayer Cat-TTF/Im-SAM on Au; evaluation of spatial coherence of synchrotron radiation using coherent diffraction imaging technique; ambient-pressure X-ray photoemission spectroscopy of H_2 adsorption/absorption in Pd alloys and CO_2 hydrogenation reactions on Ni-based catalysts; element-selective analysis of 3D atomic structures of quasi-crystal $BaTiO_3$(111)/Pt(111) thin film with photoelectron holography technique using Display type ELlipsoidal Mesh Analyzer (DELMA).

Status of spin- and angle-resolved photoelectron spectroscopy with laser light at Laser and Synchrotron Research Laboratory

Spin- and angle-resolved photoelectron spectroscopy (SARPES) is a powerful technique to investigate the spin-dependent electronic states in solids. For example, one looks at the exchange splitting of ferromagnetic materials. Also, recently, strongly spin-orbit coupled materials, such as Rashba spin-split systems and topological insulators have been intensively studied. We developed a SARPES apparatus with a vacuum-ultraviolet (VUV) laser at Laser and Synchrotron Research Laboratory in the Institute for Solid State Physics, named LOBSTER (Laser-Optics-Based Spin-vecTor Experimental Research) machine. The LOBSTER machine is utilized to obtain precise information on spin-dependent electronic structures near the Fermi level in solids. We started a project to construct the LOBSTER machine from FY 2014 and joint researches at this station have started from FY 2015.

Figure 1 represents an overview of the LOBSTER machine [1]. The apparatus consists of an analysis chamber, a sample-bank chamber connected to a load-lock chamber, and a molecular beam epitaxy (MBE) chamber, which are kept in an ultra-high vacuum (UHV) environment and are connected with each other via UHV gate valves. The hemispherical electron analyzer is a

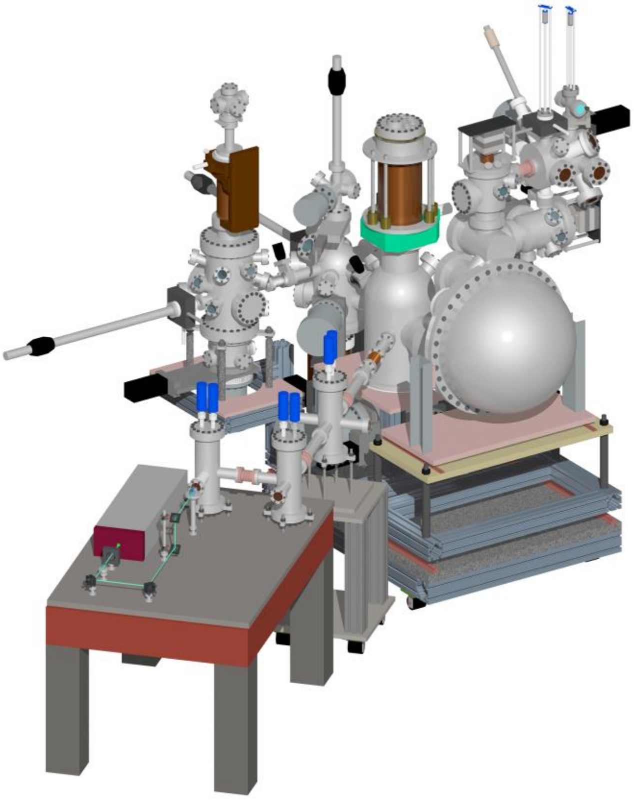

Fig. 1. Overview of the LOBSTER machine developed at the Laser and Synchrotron Research Laboratory at the Institute for Solid State Physics [1].

custom-made ScientaOmicron DA30-L, modified to attach the very-low-energy-electron-diffraction type spin detectors. The electrons are excited by 6.994-eV photons, yielded by 6th harmonic of a Nd:YVO_4 quasi-continuous wave laser with repetition rate of 120 MHz. A helium discharge lamp (VG Scienta, VUV5000) is also available as a photon source. At the MBE chamber, samples can be heated by a direct current heating or electron bombardment. The surface evaluating and preparing instruments, such as evaporators, low energy electron diffraction, sputter-gun and quartz microbalance, can be installed. At the carousel chamber, 16 samples can be stocked in the UHV environment.

In FY 2018, eight research papers were published. Among these, one of the most significant papers is the discovery of a weak topological insulator (WTI) state in a bismuth iodide, reported by Prof. Kondo group [2]. In this study, the authors were performed ARPES and SARPES with high-energy and spatial resolutions using the VUV laser for the bismuth iodide. They demonstrated a quasi-one-dimensional Dirac surface state. They also found that a crystal transition from the β-phase to the α-phase drives a topological phase transition from a nontrivial WTI to a normal insulator at roughly room temperature. The authors concluded that the weak topological phase can open a new pathway for developing novel spintronic devices that benefits from highly directional, dense spin currents that are protected against backscattering.

Reference

[1] K. Yaji, A. Harasawa, K. Kuroda, S. Toyohisa, M. Nakayama, Y. Ishida, A. Fukushima, S. Watanabe, C.-T. Chen, F. Komori and S. Shin, Rev. Sci. Instrum. **87**, 053111 (2016).

[2] R. Noguchi, T. Takahashi, K. Kuroda, M. Ochi, T. Shirasawa, M. Sakano, C. Bareille, M. Nakayama, M. D. Watson, K. Yaji, A. Harasawa, H. Iwasawa, P. Dudin, T. K. Kim, M. Hoesch, S. Shin, R. Arita, T. Sasagawa and T. Kondo, Nature **588**, 518-522 (2019).

Upshift in the Soft X-ray Science of Synchrotron Radiation

Date: 2018/11/30 (Fri.) , 2018/12/01 (Sat.)
Place: Lecture Room (A632), 6th Floor, ISSP, the University of Tokyo

Program

2018/11/30

13:00 **Opening Address** Hatsumi Mori (ISSP, the University of Tokyo)
Guest Address Atsushi Oku (MEXT)
Guest Address Wataru Utsumi (QST)
Guest Address Tadahiro Hayasaka (Tohoku University)

13:15 **To Map the Next Generation SR Facility in the Academic Community in IMRAM, Tohoku Univ.**
Atsushi Muramatsu (Institute of Multidisciplinary Research for Advanced Materials, Tohoku University)

13:45 **A Role of Next Generation Synchrotron Radiation Facility to Build a New Range of Innovation**
Masaki Takata (PhoSIC / Institute of Multidisciplinary Research for Advanced Materials, Tohoku University)

14:15 **Activities of the University of Tokyo for the next-generation synchrotron radiation facility**
Taka-hisa Arima (Department of Advanced Materials Science, University of Tokyo)

14:45 **Future of coherent diffractive imaging pioneered by the next-generation synchrotron radiation source**
Yukio Takahashi (Graduate School of Engineering, Osaka University)

15:15 **Photo & Coffee break**

15:30 **Facilitating protein microcrystallography by automated data processing**
KeitaroYamashita (The University of Tokyo / RIKEN SPring-8 Center)

16:00 **Expectation for Next Generation Synchrotron Radiation Facilities:**
From the Viewpoint of Physical Chemistry and Surface Science
Jun Yoshinobu (The Institute for Solid State Physics, The University of Tokyo)

16:30 **The potential of next generation light sources to promote the soft X-ray science**
Yusuke Tamenori (Japan Synchrotron Radiation Research Institute (JASRI) / Tohoku University)

17:00 **Contributing advanced technology through precision manufacturing**
Yuko Akabane (TDC Corporation)

18:00 **Banquet**

2018/12/01

9:30 **Transfers of the Techniques from SPring-8 BL07LSU**
Iwao Matsuda (The institute for Solid State Physics, the University of Tokyo)

10:00 **Current status of development of micro- and nano- focusing mirrors for soft x-rays**
Hidekazu Mimura (Graduate school of engineering, The University of Tokyo)

10:30 **A two-color BL brings new colors of a SR facility**
Hitoshi Abe (Institute of Materials Structure Science, High Energy Accelerator Research Organization / Dept. of Materials Structure Science, Sch. of High Energy Accelerator Science, SOKENDAI)

11:00 **Development of soft x-ray polarization switching for studying spin dynamics**
Hiroki Wadati (Institute for Solid State Physics, University of Tokyo)

11:30 **Lunch**

13:00 **Combining Nano-focus, Operando, Machine Learning, Enough for further progress?**
Hirokazu Fukidome (Research Institute of Electrical Communication,
Tohoku University)

13:30 **Catalysis science by *operando* soft X-ray spectroscopy:**
Present status and future prospect at next generation synchrotron radiation facility
Susumu Yamamoto (The Institute for Solid State Physics, The University of Tokyo)

14:00 **Solid state physics and its future development with nano-spin ARPES**
Takeshi Kondo (ISSP, The University of Tokyo)

14:30 **Poster Session**

15:00 **Coffee Break**

15:30 **Crystal structure prediction by data assimilation**
Synge Todo (Department of Physics, University of Tokyo / Institute for Solid State Physics, University of Tokyo / MaDIS, National Institute for Materials Science)

16:00 **Recent status and future of a scanning transmission X-ray microscope in UVSOR-III)**
Takuji Ohigashi (UVSOR Synchrotron Facility, Institute for Molecular Science / Sokendai)

16:30 **Development for high-speed magnetic imaging by fusion of coherent soft X-ray and information technology)**
Yuichi Yamasaki (NIMS-MaDIS, JST-PRESTO, RIKEN-CEMS)

17:00 **Strategy for resonant inelastic soft X-ray scattering using next-generation synchrotron radiation)**
Yoshihisa Harada (Institute for Solid State Physics, University of Tokyo)

17:30 **Closing Address** Nobuhiro Kosugi (JSSRR)

The conference was organized on November 30 and December 1 to promote scientific and technological innovations of soft X-ray synchrotron radiation, motivated by the announcement on the next-generation facility by the Minister of Education, Culture, Sports, Science and Technology on July 3, 2018. It has successfully brought together more than 200 participants, including the presidents and the outstanding researchers of synchrotron radiation institutes and societies from all over Japan. The presentations at the ISSP lecture room were broadcast live to a conference room in SPring-8 through the internet. On the first day, the program focused on science and technology to be evolved at the new facility, while, on the second day, it featured experimental methods and information technologies to be developed toward researches with the light source.

With the next-generation soft X-ray synchrotron radiation, measurements are expected to be made with multi-dimensional data acquisitions or with ultra-high resolutions that have never been possible at the existing facilities. The attendance interdisciplinarily argued research topics to respond to needs in academic and industrial fields today. There was also vigorous discussion on the cutting-edge informatics to be applied in the data analysis. We were confident that the workshop was very timely and that all the arguments would become seeds of the novel science and technology.

The conference was hosted by the Institute for Solid State Physics (the University of Tokyo), Synchrotron Radiation Research Organization (the University of Tokyo), Tohoku University, and User Community of VUV･SX high-brilliant light sources.

(I. Matsuda, T. Arima, Y. Harada, H. Wadati, T. Kondo, S. Shin)

4. Seminar

Date: May 30, 2018
Title: Spin-texture in image potential state and optical spincurrent control at surface
Speaker: Dr. Ryuichi Arafune
（National Institute for Materials Science）

Date: June 19, 2018
Title: Electron dynamics at nanoscale organic surfaces and interfaces studied by time-resolved photoelectron microspectroscopy
Speaker: Dr. Masahiro Shibuta
（Graduate School of Science and Technology, Keio University）

Date: December 19, 2018
Title: Micro-Nano bubble Properties and the Acceleration Effect on Gas Hydrate Formation
Speaker: Dr. Tsutomu Uchida
（Graduate School of Engineering, Hokkaido University）

OBSERVATION OF Li DIFFUSION AND ELECTRONIC-STRUCTURE DISTRIBUTION IN THE ACTIVE MATERIAL OF ALL-SOLID-STATE Li-ION BATTERY BY *OPERANDO* PHOTOELECTRON SPECTROMICROSCOPY

Keishi Akada[1], Takaaki Sudayama[2], Daisuke Asakura[2,3], Hirofumi Matsuda[2,3],
Naoka Nagamura[4], Masaharu Oshima[5], Eiji Hosono[2,3], Yoshihisa Harada[1,3]

[1]*Institute for Solid State Physics, The University of Tokyo,*
[2]*Research Institute for Energy Conservation,*
National Institute of Advanced Industrial Science and Technology (AIST),
[3]*AIST-UTokyo Advanced Operando-Measurement Technology Open Innovation Laboratory (OPERANDO-OIL),*
[4] *Research Center for Advanced Measurement and Characterization,*
National Institute for Materials Science (NIMS),
[5]*Synchrotron Radiation Research Organization, The University of Tokyo*

For a sustainable modern society, Li-ion-batteries (LIBs) play a more important role as an energy storage of electric vehicles. Understanding the operation mechanisms of LIBs is necessary to improve their properties, such as energy density, safety operation, and thermal stability, etc. Therefore, an elucidation of lithiation/delithiation phenomena by detailed electronic-state analysis under potential control is essential.

For this purpose, there are many reports about *operando* measurements on the electronic properties of the constituent elements. However, most of the *operando* synchrotron x-ray spectroscopy techniques typically provide average information in the region of tens or hundreds of μm which is larger than the particle size of the active materials. A spectroscopic microscopy with high spatial resolution is particularly important to further understand the charge/discharge mechanisms. This is because the method can detect changes in various electronic structures of elements closely correlated with lithiation/delithiation in single particle.

Here, we have developed *operando* photoelectron spectromicroscopy to obtain spatially resolved information to the electronic structure of a few μm single crystal LIB active materials. For this purpose, we have developed an all-solid-state LIB cell that can operate under ultra-high-vacuum conditions, and measured *operando* photoelectron spectra of $LiCoO_2$ (LCO) cathode material and $Li_4Ti_5O_{12}$ (LTO) anode material in charge/discharge state by using SPring-8 BL07LSU 3DnanoESCA having sub-100 nm spatial resolution [1].

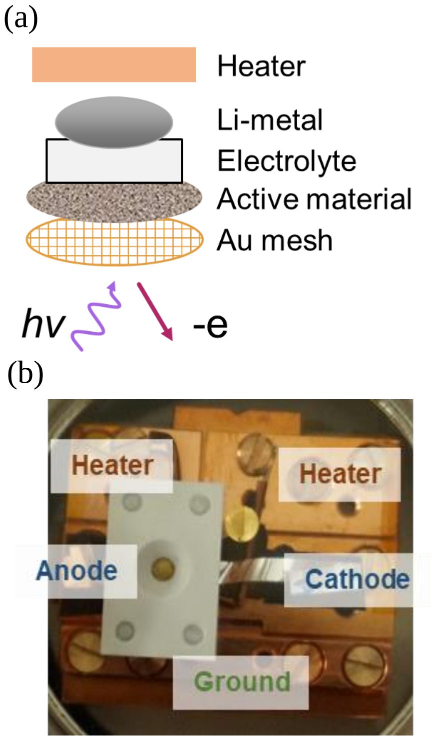

Fig. 1 (a) Schematic details of all solid-state LIBs for *Operando* photoelectron spectromicroscopy system of 3DnanoESCA. (b) Optical image of operando cell on sample holder with five terminals.

Fig. 1 shows the *operando* photoelectron spectromicroscopy system for the all-solid-state LIBs. In preparation of *operando* cell, an LCO slurry was dropped onto micro-grid/Au-mesh, and placed on a solid electrolyte after slurry drying. The *operando* cell was fabricated in an Ar-filled glovebox using Li metal as an anode material, and all of component were fixed by ceramics jigs which has a hole for exposing LCO particles. A photoelectron intensity mapping could be obtained by scanning a soft X-ray beam, which is focused on a sample by using a Fresnel zone plate.

In an experiment, we obtained the Co 3p and Li 1s spectral mapping on LCO single crystal after Li extraction. Integrated spectra form each facet shows that atomic ratios of Li: Co were different depending on the facets. This result indicates that Li extraction varies with the facets, and guaranteed the reliability of our *operando* photoelectron spectromicroscopy[2].

Furthermore, this *operando* measurement was applied to $Li_4Ti_5O_{12}$ anode material, which has excellent performance for rapid charging and cycle stability. Fig. 2 (a-c) shows spectral mapping of LTO single particle comparing with optical and SEM images. As Fig. 2 (d), we compared Ti 3p changes after charging and discharging on the LTO particle, and found that SEI was formed and Li 3p was hidden during Li insertion. During LTO charge/discharge, lithium insertion and extraction proceed between two coexisting phases, spinel $Li_4Ti_5O_{12}$ and the rock salt $Li_7Ti_5O_{12}$ (Li-rich phase). In additional experiments conducted after this beamtime, we found that the Ti 3p peak shows chemical shifts as a result of phase change during the Li desertion [3].

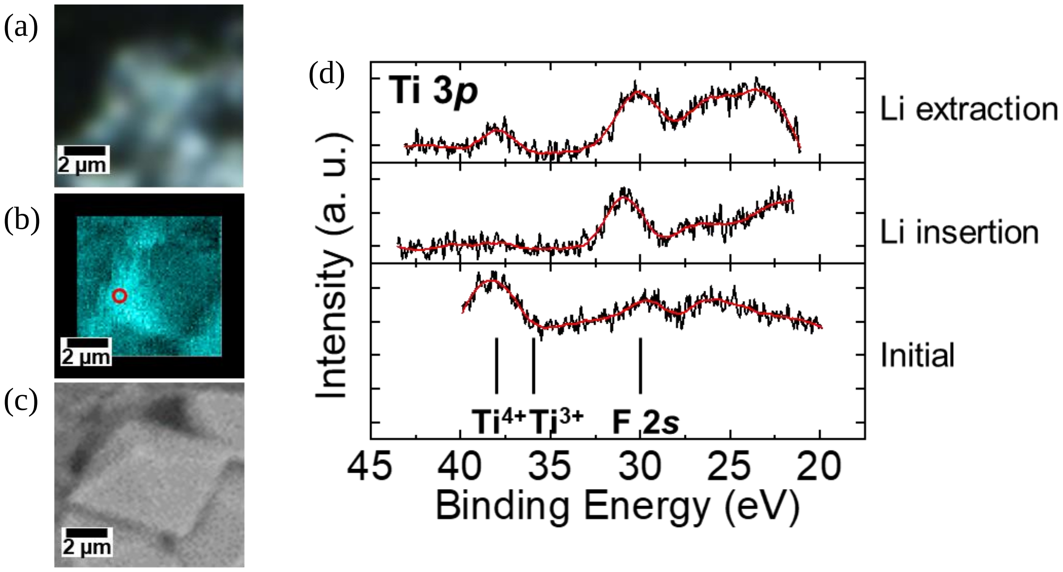

Fig. 2 Optical microscopy (a), photoelectron intensity mapping (b), and SEM (c) images of LTO single particle. (d) Ti 3p XPS spectra from LTO particle in (b).

REFERENCES

[1] K. Horiba, Y. Nakamura, N. Nagamura, S. Toyoda, H. Kumigashira, M. Oshima, K. Amemiya, Y. Senba, and H. Ohashi, Rev. Sci. Instrum. **82**, 113701 (2011).

[2] K. Akada, T. Sudayama, D. Asakura, H. Kitaura, N. Nagamura, K. Horiba, M. Oshima, E. Hosono, and Y. Harada, Submitted.

[3] K. Akada, T. Sudayama, D. Asakura, H. Kitaura, N. Nagamura, K. Horiba, M. Oshima, E. Hosono, and Y. Harada, J. Electron Spectros. Relat. Phenomena **233**, 64 (2019).

X-RAY PHOTOELECTRON SPECTROMICROSCOPY OF LITHIUM STORAGE IN SnO_2 SINGLE-PARTICLE MICROWIRE ANODE MATERIAL

Keishi Akada[1], Takaaki Sudayama[2], Daisuke Asakura[2,3], Hirofumi Matsuda[2,3],
Naoka Nagamura[4], Masaharu Oshima[5], Eiji Hosono[2,3], Yoshihisa Harada[1,3]

[1]Institute for Solid State Physics, The University of Tokyo,
[2]Research Institute for Energy Conservation,
National Institute of Advanced Industrial Science and Technology (AIST),
[3]AIST-UTokyo Advanced Operando-Measurement Technology Open Innovation Laboratory (OPERANDO-OIL),
[4] Research Center for Advanced Measurement and Characterization,
National Institute for Materials Science (NIMS),
[5]Synchrotron Radiation Research Organization, The University of Tokyo

To develop innovative materials for lithium-ion batteries (LIBs), which are rapidly increasing in demand, intensive research has been carried out in the research fields of cathode and anode materials. While novel materials have been eagerly sought for cathodes, anode materials have been focused on the use of metallic Li and alloy materials such as silicon and tin oxide (SnO_2). Compared with commonly used graphite-based anode materials, alloy-based materials are expected to increase in capacity by several to dozens of times. However, the low cycle characteristics of alloy materials are a problem, because a large volume change occurs with lithiation/delithiation during charge/discharge processes.

To overcome this problem, we propose *in situ* photoelectron spectromicroscopy with high spatial resolution in SnO_2 wire during lithiation. We analyze the detail electronic states of each element in the electrode, and reveal the charge/discharge mechanism such as lithium diffusion and volume/shape change. This study aims to develop a cycle degradation control technique based on the understanding these phenomena. Therefore, we conducted an *in situ* measurement during lithiation into single particle anode material by using 3DnanoESCA[1].

By the proposed method, the lithiation reaction in SnO_2 single crystal can be visualized with spectral mapping, and the effect from crystal orientation and facet on lithiation and diffusion will be clarified [2,3]. Since detailed changes of chemical states are revealed from photoelectron spectroscopy measurement, discrimination between conversion reaction of SnO_2 and alloying reaction of Sn and Li is also expected. The findings obtained by the proposed experiments will greatly contribute to the future development of Li-ion batteries.

In the sample preparation, we embedded SnO_2 wires on metal Li in Ar-filled glovebox. This sample was put on the heater, which was connected to the terminal of the sample holder. This sample and sample holder was transferred into the 3DnanoESCA chamber without air exposure, and the SnO_2 wire was observed with photoelectron mapping. The sample was heated to promote the Li reaction, and the morphological and chemical changes were observed from mapping and photoelectron spectroscopy. Observed SnO_2 wires were observed before and after beamtime without air exposure using high resolution optical microscope and compared with the results of 3DnanoESCA.

Fig. 1 (a, b) shows obtained images of optical microscopy and photoelectron intensity mapping of SnO_2 after Li reaction enhanced at 50°C. Li diffused from the left side of the images and reacted with SnO_2, and the reacted area was strongly expanded in the left region. The photoelectron spectra (Fig. 2) of Sn 3d showed that the Sn^{4+} peak on SnO_2 wire (red) was shifted to Sn^0 peak on the reacted region (green), which means SnO_2 wire was reduced and changed to metal Sn and/or Sn-Li alloy. The Li 1s also showed that components of Li_2O and Li_xSn are detected in the reacted region. These results clearly shows that the conversion reaction and the alloying reaction proceeded in the reacted region.

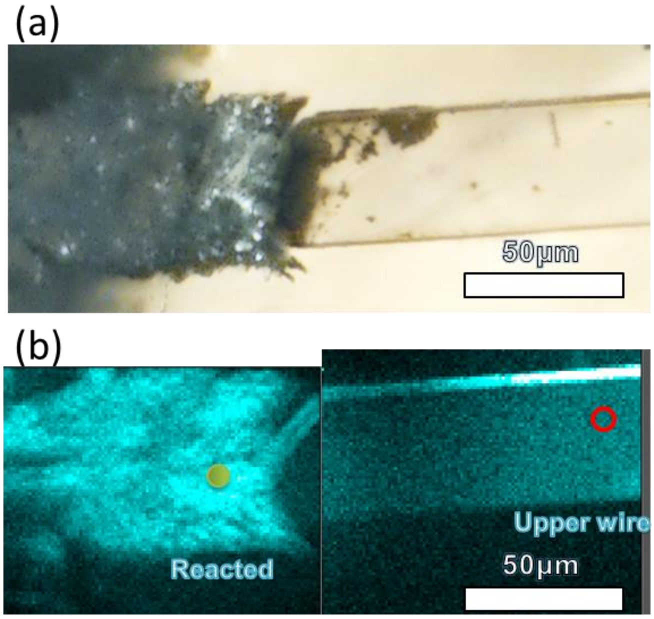

Fig. 1 Optical (a) and photoelectron intensity mapping (b) images of partially reacted SnO2 wire.

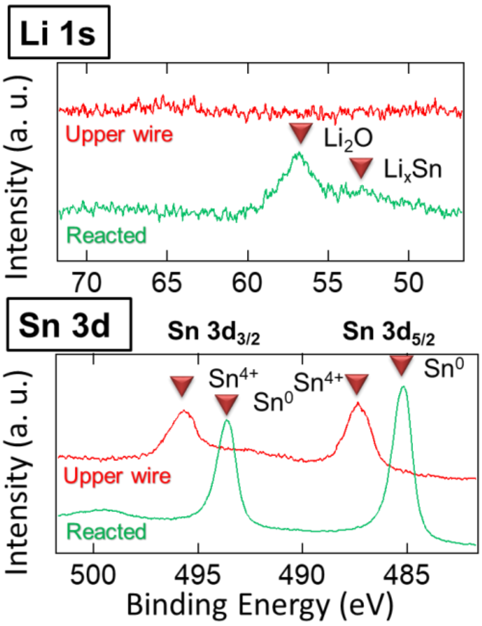

Fig. 2 Pin-point XPS spectra of Li 1s and Sn 3d from upper wire and reacted region on photoelectron mapping in Fig. 1 (b).

REFERENCES

[1] K. Horiba, Y. Nakamura, N. Nagamura, S. Toyoda, H. Kumigashira, M. Oshima, K. Amemiya, Y. Senba, and H. Ohashi, Rev. Sci. Instrum. **82**, 113701 (2011).

[2] K. Akada, T. Sudayama, D. Asakura, H. Kitaura, N. Nagamura, K. Horiba, M. Oshima, E. Hosono, and Y. Harada, Submitted (n.d.).

[3] K. Akada, T. Sudayama, D. Asakura, H. Kitaura, N. Nagamura, K. Horiba, M. Oshima, E. Hosono, and Y. Harada, J. Electron Spectros. Relat. Phenomena **233**, 64 (2019).

ELECTRONIC STRUCTURE ANALYSIS OF CATHODE MATERIALS FOR LI-ION BATTERIES BY OPERANDO SOFT X-RAY EMISSION SPECTROSCOPY USING AN AQUEOUS ELECTROLYTE SOLUTION

Daisuke Asakura[1,2], Takaaki Sudayama[1], Jun Miyawaki[3,4], Yoshihisa Harada[2,3,4], and Eiji Hosono[1,2]

[1]*Research Institute for Energy Conservation, National Institute of Advanced Industrial Science and Technology (AIST)*

[2]*AIST-UTokyo Advanced Operando-Measurement Technology Open Innovation Laboratory, AIST*

[3]*Synchrotron Radiation Laboratory, The Institute for Solid State Physics, The University of Tokyo*

[4]*Synchrotron Radiation Research Organization, The University of Tokyo*

Improvement of the performances of electrode materials for Li-ion batteries (LIBs) are highly important to further develop electric and hybrid-electric vehicles. To develop novel electrode materials having high performances, understanding the charge-discharge mechanisms of the electrode materials from a viewpoint of the electronic structure is indispensable. Soft x-ray spectroscopy, which directly reveals the 3*d* orbital of transition metals, has recently attracted much attention for the electronic-structure analyses of the electrode materials.

In this study we demonstrate *operando* soft x-ray emission spectroscopy (XES) for $LiFePO_4$ with an aqueous electrolyte solution. $LiFePO_4$ is a typical cathode material for LIB[1] and works as a cathode even for an aqueous electrolyte solution as well as organic electrolyte solutions used for general LIB. While a high voltage cannot be obtained for the aqueous LIBs because of the narrow voltage window for H_2O, the redox reaction in the host framework of $LiFePO_4$ is expected to be almost the same with the case when an organic electrolyte solution is used.

We developed an *in situ* cell consisting of the $LiFePO_4$ cathode, a Pt-wire counter electrode, Ag/AgCl reference electrode, and a 1 M $LiNO_3/H_2O$ electrolyte solution by modifying the *in situ* cell for fuel cell catalysts[2]. The charge-discharge experiment was performed with cyclic voltammetry (CV) with a scan speed of 0.5 mV/s. The XES spectra were recorded at the four points on the second cycle (OCV 1 → charge → discharge → OCV 2) shown in Fig. 1. The *operando* XES experiments were carried out using HORNET XES spectrometer[3] at BL07LSU of SPring-8. We selected 708 eV as the excitation energy (E_{in}) in which the Fe^{2+} character should be enhanced for the Fe L_3-edge absorption spectrum. The charge-discharge experiments were performed by cyclic voltammetry. The *operando* XES measurements were performed for the second charge-discharge cycle.

The Fe 2*p*-3*d*-2*p* resonant XES spectra revealed great difference between the slurry (initial state) $LiFePO_4$ powder and open-circuit-voltage (OCV) state after the first cycle (OCV 1, -0.07 V) (Fig. 2). For the slurry, the *dd*-excitation peaks are clearly observed from 704 to 707.5 eV and the charge-transfer (CT) excitation is

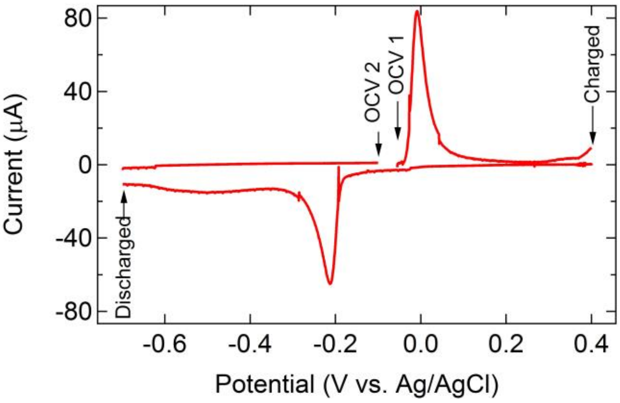

Fig. 1: The CV curve for the *operando* XES measurement. The potentials for the charged and discharged states were maintained by a potentiostatic operation. For OCV 1 and 2, the potentials were almost unchanged during recording the corresponding XES spectra.

considerably suppressed. These results are ascribed to be the Fe^{2+} high-spin state as shown in a previous report[4]. For OCV 1, broad feature centred on ~703 eV should overlap on the Fe^{2+} peaks.

For the charged state (+0.4 V), the profile is substantially changed from that of the OCV 1. Especially, the intensity for 704.5-707.5 eV greatly decreased, indicating a disappearance of the Fe^{2+} component possibly due to the oxidation reaction to Fe^{3+} state with Li extraction. Then, the profile for the charged state should be of the Fe^{3+} state. For the discharged state (-0.7 V), the *dd*-excitation peaks for the Fe^{2+} state as with the slurry appeared again, suggesting a reduction reaction to the Fe^{2+} state by discharge (Li re-intercalation). The spectrum for OCV 2 (-0.1 V) is similar to that for discharged state.

In summary, *operando* XES measurements for $LiFePO_4$ with an aqueous electrolyte solution were performed to reveal the Fe 3*d* electronic-structure change during the charge-discharge process. The great difference between the slurry and OCV 1 and the XES profile of charged state possibly reflecting the Fe^{3+} state indicate that the redox inactive Fe^{3+} component should be formed by the first cycle. For the second cycle, the redox reaction is reversible to some extent. In future, the electronic-structure parameters for the Fe^{2+} and Fe^{3+} states will be determined accurately by using multiplet calculations. The relationship between the electronic structure and electrochemical properties will also be discussed.

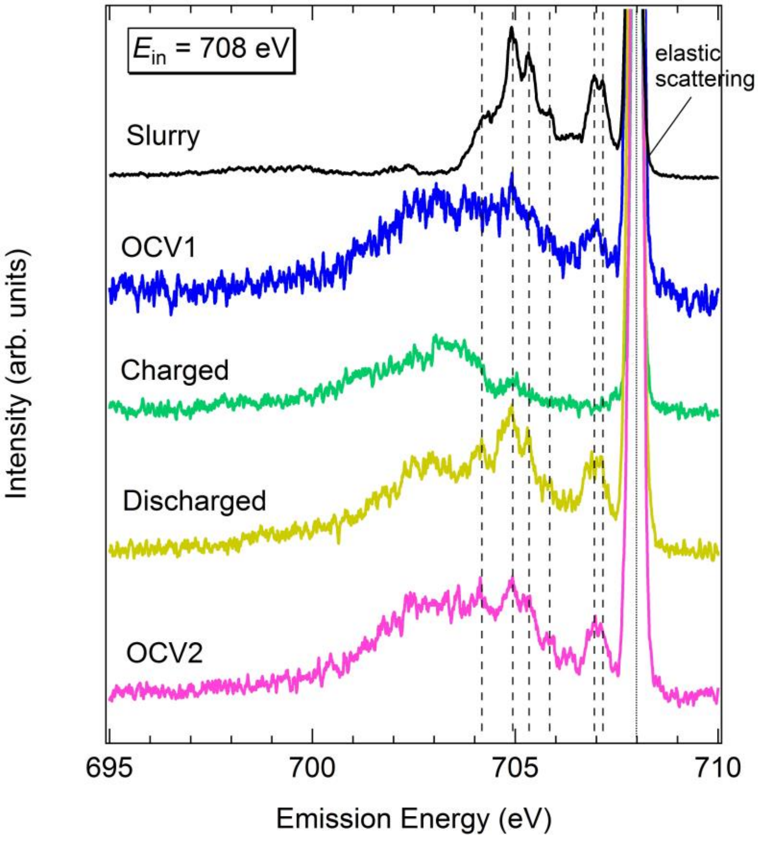

Fig. 2: *Operando* Fe 2*p*-3*d*-2*p* XES spectra for $LiFePO_4$.

REFERENCES

[1] A. K. Padhi *et al.*, J. Electrochem. Soc. **144**, 1188 (1997).
[2] H. Niwa *et al.*, Electrochem. Commun. **35**, 57 (2013).
[3] Y. Harada *et al.*, Rev. Sci. Instrum. **83**, 013116 (2012).
[4] D. Asakura *et al.*, Chem. Phys. Chem. **19**, 988 (2018).

AN OPERANDO SOFT X-RAY SPECTROSCOPY STUDY OF A CATHODE MATERIAL FOR LI-ION BATTERIES TO INVESTIGATE THE REACTION OF EACH REDOX PEAK

Daisuke Asakura[1,2], Takaaki Sudayama[1], Hirofumi Matsuda[1,2], Jun Miyawaki[3,4],
Yoshihisa Harada[2,3,4], and Eiji Hosono[1,2]

[1]*Research Institute for Energy Conservation, National Institute of Advanced Industrial Science and Technology (AIST)*

[2]*AIST-UTokyo Advanced Operando-Measurement Technology Open Innovation Laboratory, AIST*

[3]*Synchrotron Radiation Laboratory, The Institute for Solid State Physics, The University of Tokyo*

[4]*Synchrotron Radiation Research Organization, The University of Tokyo*

The redox potential of electrode materials for Li-ion batteries (LIBs) is the most important parameter to realize high-voltage LIB. For the cathode materials, the redox potential should be high as long as the electrolyte solution used in the battery is not decomposed. For example, $LiCoO_2$ (LCO) and $LiMn_2O_4$ (LMO) which are typical cathode materials exhibit redox potential of ~4 V vs. Li/Li^+. In contrast, $LiFePO_4$ (LFP) has a redox potential of 3.5 V vs. Li/Li^+ based on the Fe^{2+}/Fe^{3+} redox couple, while the chemical/thermal stability and charge-discharge cycle performances of LFP are higher than those of LCO and LMO. To elevate the redox potential of LFP, it is well known that substitution of Mn for Fe is effective.[1] A potential plateau indeed appears at 4 V vs. Li/Li^+ by the Mn doping, which is thought to be of the Mn^{2+}/Mn^{3+} redox couple. On the other hand, there are several reports suggesting that redox-inactive Mn exists.[2] In this study, we confirmed the redox reactions of $LiMn_{0.5}Fe_{0.5}PO_4$ (LMFP) by using *operando* soft X-ray spectroscopy.

For the *operando* experiment, we used our *operando* cell[3] with an oxygen-free current collector for O *K*-edge measurement. LMFP thin-film layer was directly fabricated by sputtering on the oxygen-free current collector layer on Si_3N_4 window (150 nm) which separate the vacuum from the electrolyte solution. The *operando* soft X-ray absorption spectroscopy (XAS) for the LMFP thin film were carried out at BL07LSU of SPring-8.[4] Partial-fluorescence-yield (PFY) detection mode using a silicon-drift detector was employed for the XAS measurement. The charge-discharge experiment was performed with cyclic voltammetry (CV) (Fig. 1). The *operando* XAS spectra were recorded at the five points on the second cycle as shown in Fig. 1: ① open-circuit voltage (OCV), ② 4.0-V charge, ③ full charge, ④ 3.7-V discharge, and ⑤ full discharge.

Figure 2(a) shows the *operando* XAS spectra at the Mn *L* edge. The XAS spectrum for ① OCV is attributed to Mn^{2+} high-spin state. This profile did not change for ② 4.0-V charge. For ③ full charge, the Mn L_3 peaks became smaller and a broad structure centered on 643 eV appeared. Moreover, the peak at 652.5 eV for the Mn L_2 edge was slightly enhanced. These changes suggest a small amount of Mn^{3+} emerged by charge, while the Mn^{2+} component considerably remained. The XAS profile returned to the Mn^{2+} state for ④ 3.7-V discharge and maintained after

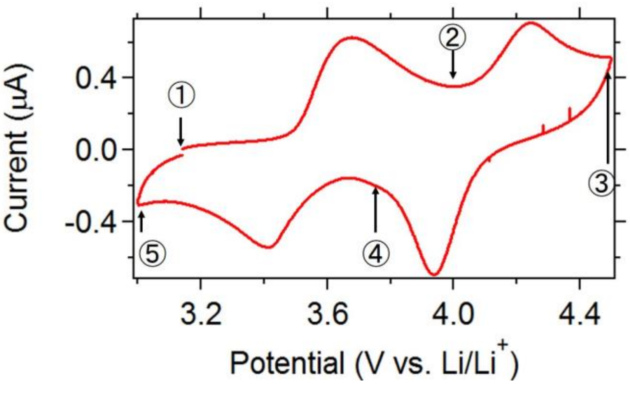

Fig. 1. CV curve for LMFP. ①－⑤indicate potentials where the *operando* XAS was performed.

⑤ full discharge, indicating the oxidation peak centered on 4.2 V and the reduction peak centered on 3.9 V in Fig. 1 are of partial redox reaction on the Mn. On the other hand, the Fe *L*-edge XAS largely changed for ① → ② and ④ → ⑤ (Fig. 2(b)). These reactions are attributed to reversible $Fe^{2+} \Leftrightarrow Fe^{3+}$ redox reaction around 3.5 V similar to LFP.

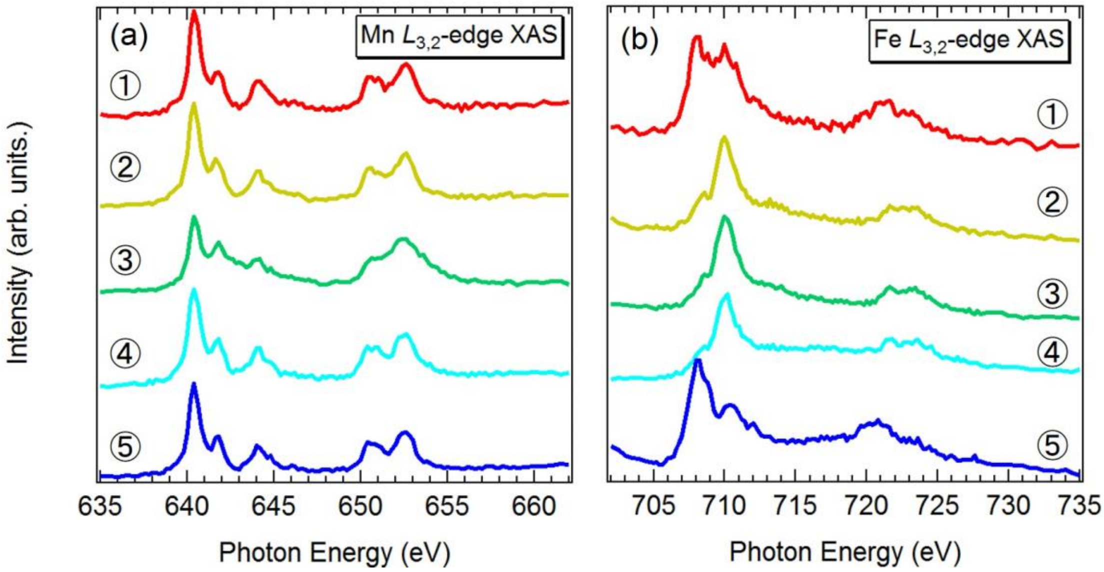

Fig. 2. *Operando* XAS results (a) at the Mn *L*-edge and (b) Fe *L*-edge. The numbers correspond to the potentials in Fig. 1.

The O *K*-edge XAS profile gradually changed during the charge-discharge process (Fig. 3). In particular, the pre-edge region below 532 eV was enhanced for ③ full charge. Taking the Mn *L*-edge XAS results into account, the Mn 3*d*-O 2*p* hybridized orbital should be redox active around 4 V. In addition, the peak at 533 eV comes from the electrolyte solution.

In summary, we measured the *operando* XAS at the Mn *L*-edge, Fe *L*-edge and O *K*-edge for LMFP. The redox orbital around 4 V is not attributed to localized Mn 3*d* orbital, but hybridized Mn 3*d*-O 2*p* orbital. In the near future, we will perform the *operando* soft X-ray emission spectroscopy to further understand the redox reaction.

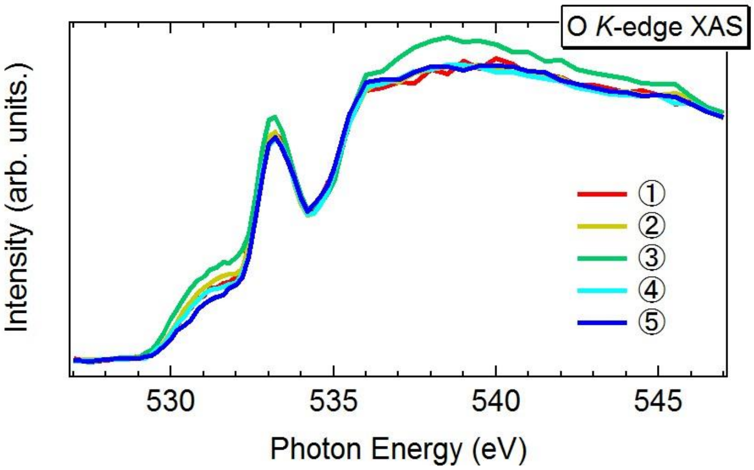

Fig. 3. *Operando* XAS results at the O *K*-edge.

REFERENCES

[1] For example, A. Yamada *et al*., J. Electrochem. Soc. **148**, A747 (2001).
[2] For example, L. F. J. Piper *et al*., J. Phys. Chem. C **117**, 10383 (2013).
[3] D. Asakura *et al*., Electrochem. Commun. **50**, 93 (2015).
[4] Y. Harada *et al*., Rev. Sci. Instrum. **83**, 013116 (2012).

PROBING OXYGEN-REDOX IN BATTERY CATHODES

Masashi Okubo
Department of Chemical System Engineering, School of Engineering, The University of Tokyo

Current lithium-ion battery (LIB) technology powers most of today's portable electronics, in part, owing to the high energy efficiency with which LIBs operate through intercalation chemistry. However, the tremendous industrial demand resulting from the market penetration of electric vehicles has significantly raised the requirement for the development of rechargeable batteries with higher energy density.

One of the main means of increasing the energy density of batteries is the development of the positive electrode (cathode), in which ion (de)intercalation is charge-compensated by the redox reactions of transition metals. Quantitatively, in the conventional charge-compensation regime, which relies on the redox capability of transition metals, the theoretical capacity is maximized for the chemical composition of AMO_2 (A: alkali metal, M: transition metal). However, recent experimental observations have shown that A-excess transition-metal oxides, $A_{1+x}M_{1-x}O_2$, can deliver large extra capacities exceeding the theoretical limit of the M-redox reaction because of an additional oxygen-redox capacity. For example, $Li_{1.2}Ni_{0.13}Co_{0.13}Mn_{0.54}O_2$ gives a large specific capacity of 270 mAh g^{-1} with a large contribution from an oxygen-redox reaction (~150 mAh g^{-1}). Therefore, exploiting additional oxygen-redox reactions of oxides would significantly contribute to surpassing the current energy-density limit of batteries.

We investigated the reversible oxygen-redox capacity of a layered sodium manganese oxide $Na_2Mn_3O_7$. $Na_2Mn_3O_7$ ($Na_{4/7}[\square_{1/7}Mn^{4+}_{6/7}]O_2$ in conventional Na_xMO_2 notation) consists of Na^+ and $[\square_{1/7}Mn^{4+}_{6/7}]$ layers that stack alternately (Figure 1). We expect that $Na_2Mn_3O_7$ has nonbonding 2*p* orbitals of oxygens neighboring $\square$, leading to an extra oxygen-redox capacity upon Na^+ extraction at a higher potential.

The powder X-ray diffraction (XRD) pattern of the as-prepared compound confirms the successful synthesis of $Na_2Mn_3O_7$. The galvanostatic charge/discharge curves of $Na_{2+x}Mn_3O_7$ recorded between 1.5 and 3.0 V vs. Na/Na^+ (Figure 1) confirm the reversible electrochemical reaction of $Na_2Mn_3O_7 \leftrightarrow Na_4Mn_3O_7$ based on Mn^{4+}/Mn^{3+}. In addition, we confirm that Na^+ can also be deintercalated from $Na_2Mn_3O_7$. The galvanostatic charge/discharge curves for first few cycles between 3.0 and 4.7 V vs. Na/Na^+ at a C/20 rate show that $Na_{2-x}Mn_3O_7$ delivers an extra

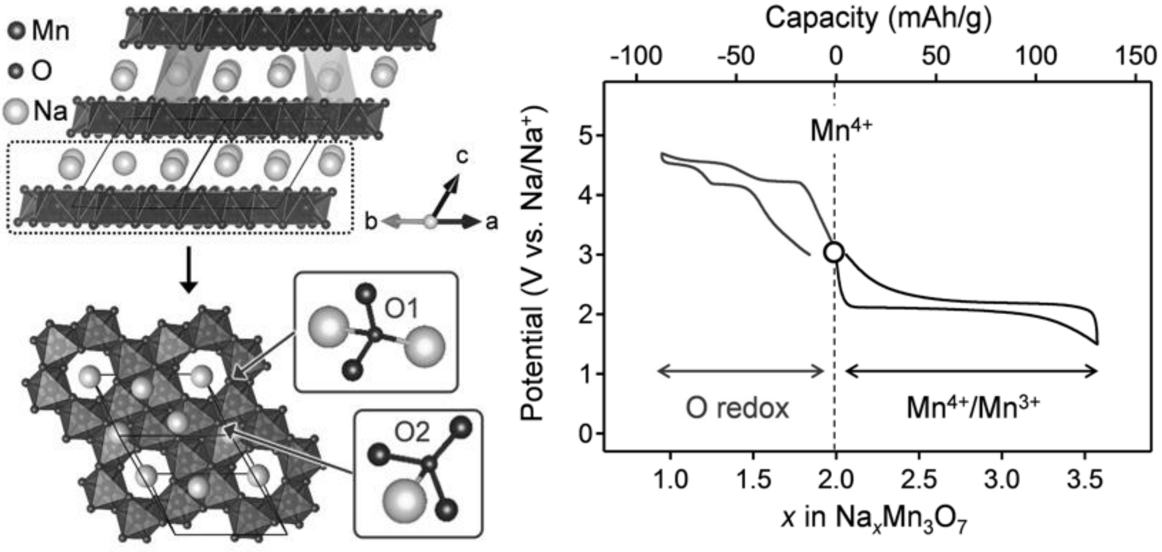

Figure 1. Left: Crystal structure of $Na_2Mn_3O_7$. Right: Charge-discharge curves of $Na_2Mn_3O_7$ in a sodium-ion cell.

reversible capacity of approximately 75 mAh g^{-1}, corresponding to the (de)intercalation of 1.0 Na^+ per formula unit ($Na_2Mn_3O_7 \leftrightarrow NaMn_3O_7$) at an average potential of 4.1 V vs. Na/Na^+. Considering that Mn^{4+} in $Na_2Mn_3O_7$ cannot undergo further oxidation during Na^+ deintercalation, the origin for this capacity is the reversible oxygen-redox reaction.

X-ray absorption spectroscopy (XAS) at the Mn L-edge and oxygen K-edge was conducted to confirm the oxygen-redox activity. The XAS spectra were measured in the bulk sensitive partial fluorescence yield (PFY) mode with a probing depth deeper than 100 nm, as well as in the surface sensitive total electron yield (TEY) mode with a probing depth of approximately 5 nm. Before charging, the XAS spectral shape of the Mn L_3-edge in the PFY mode is almost identical with that reported for Mn^{4+} in Li_2MnO_3. Maintaining its initial shape during the entire charge/discharge processes indicates that Mn in bulk does not contribute to the redox reaction. However, the XAS spectra of the Mn L_3-edge in the surface sensitive TEY mode indicate the formation of Mn^{3+} at the surface when discharging below 4.0 V vs. Na/Na^+. Therefore, at the sloping charge/discharge profile region below 4.0 V vs. Na/Na^+, the surface redox reaction of Mn^{4+}/Mn^{3+} is responsible for the capacity.

The XAS oxygen K-edge spectrum (PFY) before charging shows two pre-edge peaks that correspond to the excitation from 1s to unoccupied oxygen 2p orbitals hybridized with Mn $e_g{}^{\uparrow}$, $t_{2g}{}^{\downarrow}$, and $e_g{}^{\downarrow}$. If Mn^{4+} ions were oxidized during Na^+ deintercalation, a new absorption peak corresponding to the excitation from 1s to the unoccupied O 2p–Mn $t_{2g}{}^{\uparrow}$ state should appear at the lowest energy region (*ca.* 528 eV). However, the absorption increases at the high energy region of 532 eV after charging. The emergence of this new absorption at the high energy region upon charge is a typical behavior of oxygen-redox electrodes.

It is important to note that the oxygen K-edge XAS spectral change is reversible upon charge/discharge, confirming the reversibility of the oxygen-redox reactions. The oxidized oxygen is stabilized by a π-type interaction between the oxygen 2p and Mn t_{2g} orbitals. In addition, the large difference in the effective ionic radii of Na^+ (1.16 Å) and Mn^{4+} (0.67 Å) should suppress damaging Mn migration while coulombic attraction between Na^+ and $\square$ maintains the stacking of [$\square_{1/7}Mn^{4+}{}_{6/7}$] layers after desodiation.

In summary, a Mn deficient layered compound $Na_{2-x}Mn_3O_7$ ($Na_{4/7}[\square_{1/7}Mn^{4+}{}_{6/7}]O_2$) showed highly reversible oxygen-redox reaction at approximately 4.1 V vs. Na/Na^+. Nonbonding 2p orbitals of oxygens neighboring Mn vacancies $\square$ were determined to be essential for the reversible oxygen-redox reaction delivering an extra capacity of 75 mAh g^{-1}. This work provides a compelling future research direction toward reversible oxygen-redox cathodes for high energy density batteries through orbital/structural engineering.

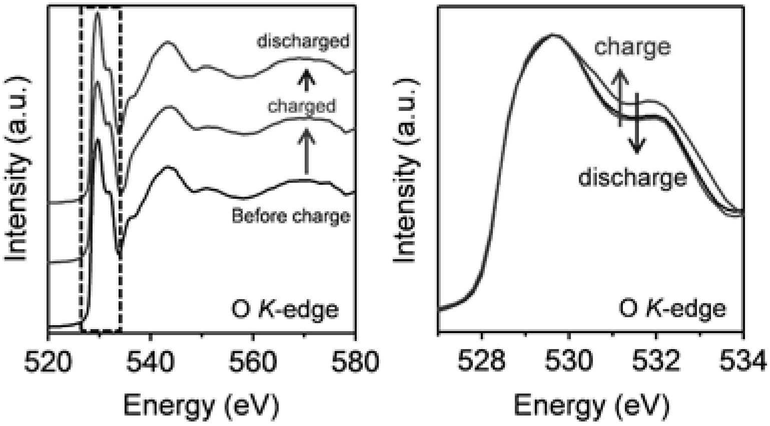

Figure 2. O K-edge X-ray absorption spectra for $Na_2Mn_3O_7$ upon charge/discharge.

REFERENCES

[1] B. Mortemard de Boisse, *et al.*, M. Okubo & A. Yamada, *Adv. Energy Mater.* (2018) 1800409.

REDOX DRIVEN SPIN TRANSITION IN SOLID

Masashi Okubo
Department of Chemical System Engineering, School of Engineering, The University of Tokyo

Electronic spin plays a crucial role in determining the physical and chemical properties of transition-metal compounds. In particular, d^4–d^7 electronic configurations of first-row transition-metals in an octahedral coordination have either high spin (HS) or low spin (LS) states, governed by the competition between the ligand-field splitting and electron paring energy. When two spin states are thermally accessible, the spin state changes (also known as spin crossover or spin transition) owing to external stimuli such as temperature, pressure, light, and chemical reactions. Because the alteration of spin states drastically modulates frontier orbitals that are fully responsible for chemical reactivity, coupling phenomena between spin transitions and chemical reactions are of great interest in chemistry. In an electrochemical system, the number of d electrons at a redox center is variable. Therefore, a stable spin state may occasionally be altered after oxidation/reduction, leading to a spin transition. Redox-driven spin transitions are important processes, for example in biochemistry, and have also been studied for possible applications for molecular devices.

In battery ceramics electrode materials containing transition-metals M, electrochemical ion (de)intercalation modulates the valence of M, which in turn changes the magnitude of the ligand-field splitting and the number of d electrons. In analogy with liquid state transition-metal complexes, it is likely that M in battery electrode materials exhibits a hitherto unreported solid-state electrochemical spin transition, which might considerably influence the operating potential of the electrodes. However, despite considerable interest in the redox behavior of M in battery electrode materials, materials featuring a RDST has not been explored to date. One suitable material for exploring this new concept is the layered transition-metal oxide $NaMO_2$ where MO_6 octahedra form a triangular two-dimensional slab and Na ions reside in the interlayer space. $NaMO_2$ has been investigated as a promising cathode material for sodium-ion batteries with a large theoretical capacity. Importantly, $NaMO_2$ maintains a layered structure with various M^{n+} owing to the large ionic size difference between Na^+ and M^{n+}. These features make the $NaMO_2$ system suitable for investigating the electrochemical properties of various redox couples $M^{(n+1)+}/M^{n+}$ in an identical solid-state matrix.

Taking advantage of the remarkable structural tolerance of $NaMO_2$ towards the variation of the electronic structure, we explored the possibility of spin transitions in Na_xMO_2 during charging/discharging reactions. Using computational calculations assuming various d^4–d^7 configurations in Na_xMO_2, we predict M^{n+}

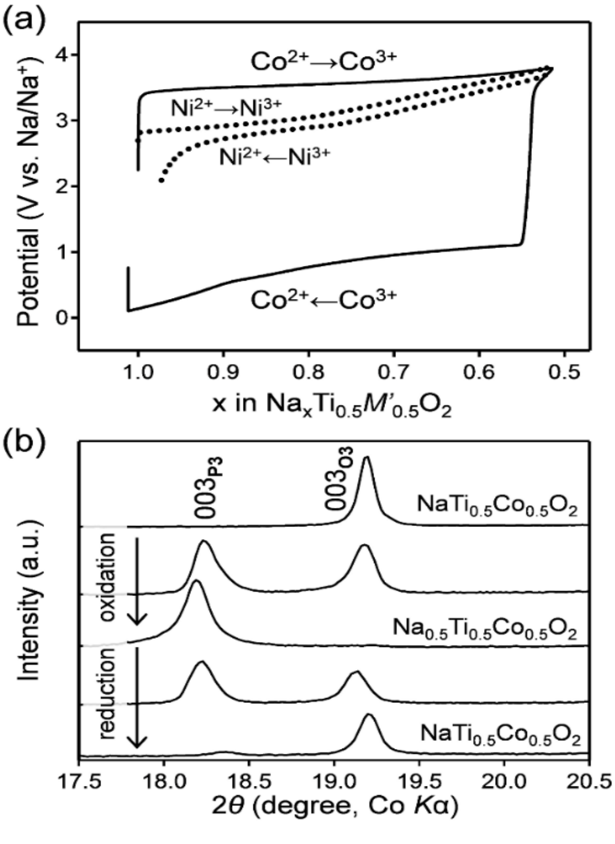

Figure 1. (a) Charge/discharge curves for O3-$Na_xTi_{0.5}Co_{0.5}O_2$ and $Na_xTi_{0.5}Ni_{0.5}O_2$. (b) Ex situ X-ray diffraction patterns for $Na_xTi_{0.5}Co_{0.5}O_2$.

species that can cause the HS-LS transition in a battery cell and verify these predictions in multiple experiments.

We verified the redox-driven spin transition for Co^{3+}/Co^{2+} experimentally. Generally, Na_xMO_2 exhibits reversible electrochemical Na-ion (de)intercalation with a small polarization owing to high Na-ion diffusivity and high electron mobility. For example, $NaTi_{0.5}Ni_{0.5}O_2$ shows reversible charge/discharge curves over a narrow voltage region. Conversely, the charge/discharge curves for $Na_xTi_{0.5}Co_{0.5}O_2$ show a large voltage hysteresis of approximately 2.8 V for the Na^+ (de)intercalation (Figure 1a). This phenomenon is not caused by sluggish conversion/phase segregation because ex situ X-ray diffraction experiments confirmed a commonly-observed smooth reversible transformation between the O3 and P3 phases upon Na-ion (de)intercalation (Figure 1b). Therefore, we attribute this large voltage hysteresis to specific energetics of the electron configuration.

To clarify the change in the electronic-structure of $Na_xTi_{0.5}Co_{0.5}O_2$ upon desodiation (charging) and subsequent sodiation (discharging) processes, we measured L-edge X-ray absorption spectroscopy of the transition metals M. No significant change of the Ti L-edge spectra was observed upon charge/discharge. The spectral shapes for all samples were well reproduced by the configuration interaction (CI) calculation of Ti^{4+} in octahedral TiO_6. Clearly, Ti is not redox active during charging/discharging $Na_xTi_{0.5}Co_{0.5}O_2$. We further confirmed the redox inactivity of Ti by X-ray photoelectron spectroscopy measurements of the Ti 2p region. Conversely, the Co L-edge spectra for $Na_xTi_{0.5}Co_{0.5}O_2$ showed notable and reversible changes upon charge/discharge. The spectra for $NaTi_{0.5}Co_{0.5}O_2$ and $Na_{0.5}Ti_{0.5}Co_{0.5}O_2$ were well reproduced by CI calculations of Co^{2+} HS and Co^{3+} LS in octahedral CoO_6, respectively (Figure 2). Therefore, the stable spin state of Co reversibly changed during the charging/discharging of $Na_xTi_{0.5}Co_{0.5}O_2$.

In summary, we discovered a solid-state redox-driven spin-state transition of Co^{3+}/Co^{2+} in layered transition metal oxides upon reversible sodium intercalation reaction in an electro-chemical cell. Our work points to the considerable influence of the spin-state variance of transition metals with d^4–d^7 configurations on their solid-state electrochemistry. Further ex-ploration in various host structures might reveal the missing link between the spin transition and electrochemical modula-tions. In a practical sense, redox-driven spin transitions cause a large voltage hysteresis (> 1 V) upon electrochemical charg-ing/discharging processes and a large loss in energy efficiency. Thus, Co^{3+}/Co^{2+}, and possibly Fe^{4+}/Fe^{3+}, in oxides should be used with care as the redox couples in battery electrodes.

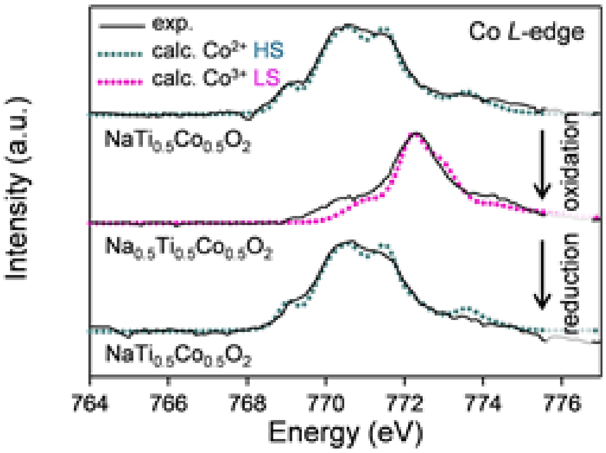

Figure 2. Ex situ Co L-edge absorption spectra for O3-$Na_xTi_{0.5}Co_{0.5}O_2$.

REFERENCES

[1] E. Watanabe, *et al.*, M. Okubo & A. Yamada, *Chem. Mater.* (2019) *31*, 2358.

ENHANCEMENT OF PHOTORESPONSIVITY OF FULLERENE IN PHTHALOCYANINE /FULLERENE ORGANIC SOLAR CELL

Kenichi Ozawa[a], Susumu Yamamoto[b], Marie D'angelo[c], Yuto Natsui[d], Naoya Terashima[d], Kazuhiko Mase[e,f], Iwao Matsuda[b]

[a]*Department of Chemistry, Tokyo Institute of Technology,* [b]*The Institute for Solid State Physics, The University of Tokyo,* [c]*Sorbonne Université, Institut des NanoScience de Paris,* [d]*Department of Advanced Physics, Hirosaki University,* [e]*Institute of Materials Structure Science, High Energy Accelerator Research Organization,* [f]*SOKENDAI (The Graduate University for Advanced Studies)*

INTRODUCTION

Organic photovoltaic (OPV) devices are one of leading solutions for realizing ubiquitous light-harvesting systems. Although much effort has been devoted to improve the OPV performance, the light-electricity conversion efficiency is no more than 15% [1]. An effective electron-hole separation before an electron-hole recombination is a key to realize a high efficiency. Thus, it is important to understand the behavior of the photoexcited electrons and holes especially at heterojunctions between p- and n-type organic semiconductors.

In the present study, layered systems fabricated by phthalocyanine (CuPc and TiOPc), a p-type organic semiconductor, and C_{60}, an n-type organic semiconductor, on a single crystalline rutile $TiO_2(110)$ surface were investigated by pump-probe time-resolved soft X-ray photoelectron spectroscopy (TRXPS) to clarify the photoexcited carrier dynamics in the layered organic thin films [2]. Photoresponsivity of C_{60} towards the ultraviolet (UV) light was found to be enhanced when the phthalocyanine layer covers the C_{60} layer.

EXPERIMENTAL

The TRXPS measurements were done at BL07LSU of SPring-8 [3]. A 402-nm UV laser was used to generate the photoexcited carriers in the organic films, and the excited states were monitored through synchrotron-radiation (SR)-excited C 1s peaks of C_{60} and phthalocyanine. The SR was provided with an H-mode operation of SPring-8 with a pulse width of about 50 ps, which corresponded to the time resolution of the TRXPS system. We also carried out conventional X-ray photoelectron spectroscopy (XPS) measurements at BL-13B of the Photon Factory [4] utilizing an SES200 electron energy analyser (Gamma Data/Scienta).

A 0.05 wt% Nb-doped rutile TiO_2 crystal with (110) orientation was used as a substrate. The (110) surface was cleaned in an ultrahigh vacuum (UHV) chamber by cycles of Ar^+ sputtering and annealing at 950 K in O_2 atmosphere. C_{60}, CuPc and TiOPc were evaporated on the TiO_2 surface at room temperature using Knudsen cells. The thicknesses of the organic layers were adjusted to monolayer-equivalent thicknesses, i.e., 0.8 nm for C_{60} and 0.34 nm for the phthalocyanine molecules, by controlling evaporation rate and time.

RESULTS AND DISCUSSION

Fig. 1 shows C 1s XPS spectra of the $C_{60}/TiO_2(110)$ and $CuPc/C_{60}/TiO_2(110)$ systems. The C 1s spectrum of the former system is composed of a single component, whereas both C_{60} and CuPc contributions are confirmed by peak fitting. Even though the C_{60} layer is beneath the CuPc layer, the C 1s spectrum for the $CuPc/C_{60}/TiO_2(110)$ system is dominated by the C_{60} component, reflecting the densities of the composite C atoms in the CuPc and C_{60} layers.

Upon the UV laser irradiation, the C 1s spectrum moves slightly towards the higher binding energy side (Fig. 2). Amounts of the peak shift are 13 and 14 meV at a delay time, a time difference between the pump UV laser pulse and the probe SR pulse, of 0.1 ns for $CuPc/C_{60}/TiO_2(110)$ (Fig. 2) and $TiOPc/C_{60}/TiO_2(110)$ (not shown here but given in Ref. [2]), respectively. Since the C 1s spectrum is dominated by the C_{60} component, the observed spectral shift is caused mainly by the shift of the C_{60} component. The direction of the shift implies cationization of C_{60} after photoabsorption. We speculate that an electron excited into an unoccupied state of C_{60} is transferred to the conduction band of TiO_2. Thus, the peak shift indicates the electron-hole separation.

As the delay time is prolonged, the shift is diminished to ~8 meV for both systems (Fig. 3). Solid lines in Fig. 3 are best-fitted results using $\Delta_1 \exp(-t/\tau_1) + \Delta_2 \exp(-t/\tau_2)$, where Δ and τ are the magnitude of the shift and the decay time constant, respectively. τ for $CuPc/C_{60}/TiO_2(110)$ are 95 ns and >100 μs and those for $TiOPc/C_{60}/TiO_2(110)$ are 20 ns and >100 μs. This indicates that there are two excited states of C_{60}; one has a lifetime in a nanosecond order and the other has a very long lifetime (a microsecond order). Existence of the long-lifetime component is beneficial to the efficient OPV because it means suppression of the electron-hole recombination.

Also shown in Fig. 3 is a delay-time dependence of the C_{60} C 1s peak shift for the $C_{60}/TiO_2(110)$ system. The C 1s peak moves to the higher binding energy side upon the UV laser irradiation. The magnitude of the shift is approximately 7 meV irrespective of the delay time. If the magnitude of the shift is proportional to the density of excited C_{60}, comparison of the three systems leads us to conclude that, although the phthalocyanine overlayer partially blocks the incoming UV photons, photoresponsivity of C_{60} is enhanced by the overlayer. A pohotoresponsivity enhancement is possible when an energy is effectively transferred from excited phthalocyanine to C_{60} via either a Förster mechanism or a Dexter mechanism [5]. Such an intermolecular energy transfer is an important process in, for example, dye-sensitized solar cells, in which a repeated stack of the C_{60} and phthalocyanine layers may be effective to achieve a high efficiency.

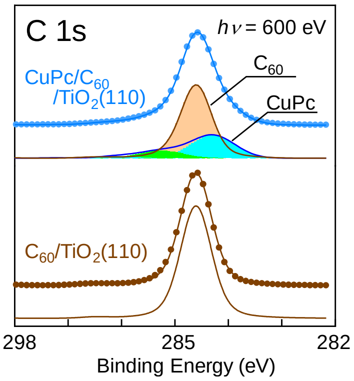

FIGURE 1. C 1s spectra of $CuPc/C_{60}/TiO_2$ and C_{60}/TiO_2. Lines drawn by dots are experimental results, and solid lines are best-fitted results of peak fitting using Voigt functions.

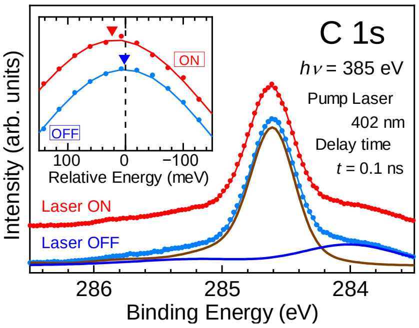

FIGURE 2. C 1s spectra of $CuPc/C_{60}/TiO_2$ without UV laser irradiation and at 0.1 ns after the laser pulse irradiation. Magnified view around the spectral peak region is shown in the inset. A slight shift of the peak position is induced by the UV irradiation.

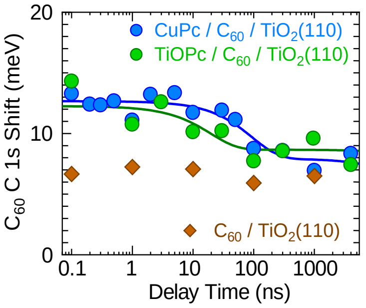

FIGURE 3. Summary of the laser-induced shift of the C_{60} C 1s peak as a function of the delay time. Dots are the experimental results and solid lines are obtained by fitting the data using a biexponential function.

REFERENCES

[1] M. Green *et al.*, Prog. Photovoltaics Res. Appl. **25**, 668−676 (2017).
[2] K. Ozawa *et al.*, J. Phys. Chem. C **123**, 4388−4395 (2019).
[3] S. Yamamoto *et al.*, J. Synchrotron Radiat. **21**, 352−365 (2014).
[4] A. Toyoshima *et al.*, J. Phys.: Conf. Ser. **425**, 152019 (2013).
[5] M. T. Lloyd et al., Mater. Today **10**, 34−41 (2007).

PHOTOELECTRON NANO-SPECTROSCOPY OF REACTIVE ION ETCHING-INDUCED DAMAGES TO THE TRENCH SIDEWALLS AND BOTTOMS OF 4H-SIC TRENCH-MOSFETS

Masaharu Oshima[1, 5], Daisuke Mori[2], Aki Takigawa[2], Akihiko Otsuki[2], Naoka Nagamura[3], Shun Konno[4], Yoshinori Takahashi[4], Masato Kotsugi[4], Hiroshi Nohira[5], Keishi Akada[1] and Yoshihisa Harada[1]

[1]The Institute for Solid State Physics, The University of Tokyo, [2]Fuji Electric Co., [3]NIMS, [4]Tokyo University of Science, [5]Tokyo City University

Silicon carbide has attracted great attention in order to be applied to high-power devices for devices that depict low power consumption, low on-resistance, and high blocking voltage, because of its superior material properties such as high voltage endurance and saturation velocity. Recently, 4H-SiC trench-MOSFETs have been regarded as one of the most promising device structures to reduce on-resistance. Furthermore, the non-polar 1-100 plane (m-plane) of 4H-SiC can offer the highest channel mobility among various SiC crystal planes and can be used as a channel plane for the trench sidewall in trench-MOSFETs. [1]

In this study, SiC trench structures having a width of 0.6 μm and a depth of 2.0 μm fabricated by reactive ion etching (RIE) using a gas mixture of SF_6, Ar, and O_2 were cleaved to expose the sidewall for the channel region of a trench MOSFET and analyzed by 3D nano-ESCA [2] using a 100 nm soft-X-ray beam at SPring-8 BL07LSU (Fig. 1). The AFM image of RIE-tranch sidewall surface is shown in Fig. 2.

It is observed that around 2 nm-thick homogeneous carbon-rich layer containing 1%-2 % F is formed on the SiC sidewalls. This may be caused due to the re-deposition of RIE reaction products, CF_4, and SiF_4 under appropriate conditions to fabricate approximately vertical trench walls, as shown in Fig. 3. Further, a carbon-rich layer having a thickness of about 2.4 nm is also formed on the bottom of the SiC trench, suggesting the possibility of selective etching of Si from the SiC substrates. CF_x species are likely to form polymer-like protective layers during the RIE process, resulting in the enhancement of the etching selectivity, and the addition of Ar to the etching gas is thought to enhance the physical reaction or sputtering effect. The overall chemical reaction can be represented as follows:

$$4\,SF_6 + 4\,O_2 + 3\,SiC \rightarrow 4\,SO_2\uparrow + 3\,SiF_4\uparrow + 3\,CF_4\uparrow \qquad (1).$$

It should be noted that the position of the Si 2*p* dominant peak that is associated with the SiC component remains constant regardless of the trench depth, as shown in Fig. 4. This suggests homogeneous band bending due to the RIE defects, which may explain the reason for no variation being observed in the gate oxide/SiC interface trap density values. The Si 2*p* binding energy of 101.1 eV on the sidewall corresponds to a band bending of 1.50 eV. Theoretical calculations using DFT reportedly revealed that the EH7 trap observed by DLTS [3] can be attributed to the presence of positively charged carbon vacancies (V_C^+) whose energy level is 1.73 eV below the CBM [4]. Based on these experiments and calculations the observed band bending of 1.50 eV may be attributed to the dominant EH7 trap or to the positively charged carbon vacancy (V_C^+). [5]

We also analysed SiC trench sidewall which was treated with thermal annealing and oxidation processes, and found that the almost same band bending remained unchanged even by these processes. Further study is needed to realize nearly flat band condition.

REFERENCES

[1] J. Senzaki *et al.*, IEEE Electron Device Lett. **23**, 13 (2002).
[2] K. Horiba *et al.*, Rev. Sci. Instrum. **82**, 113701 (2011).
[3] L. Storasta *et al.*, J. Appl. Phys. **96**, 4909 (2004).
[4] L. Torpo *et al.*, J. Phys.: Cond. Mat. **13**, 6203 (2001).

[5] M. Oshima *et al.*, e-Journal of Surf. Sci. and Nanotech. **16**, 257 (2018).

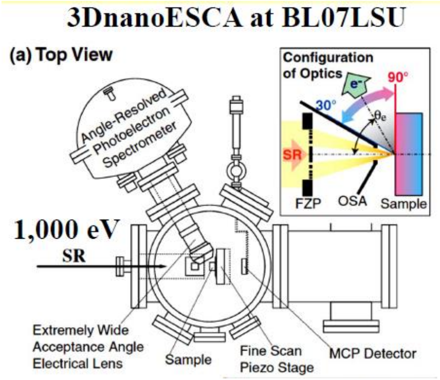

Fig. 1. 3D nano-ESCA at SPring-8 BL07LSU

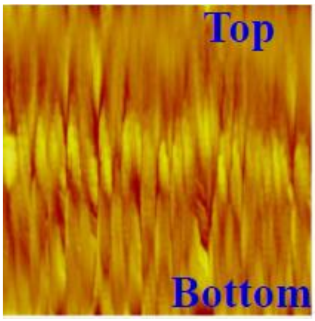

Fig. 2. AFM image of SiC trench sidewall (1μmx1μm)

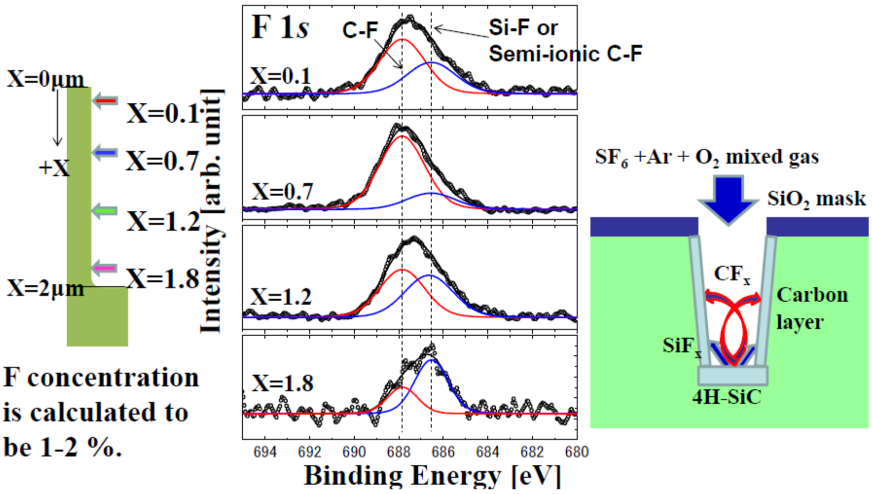

F concentration is calculated to be 1-2 %.

Fig. 3. F 1s photoelectron spectra with the deconvoluted components from four different positions (X= 0.1, 0.7, 1.2, and 1.8 μm from the surface) of the SiC trench sidewall, and a schematic model of RIE trench structure.

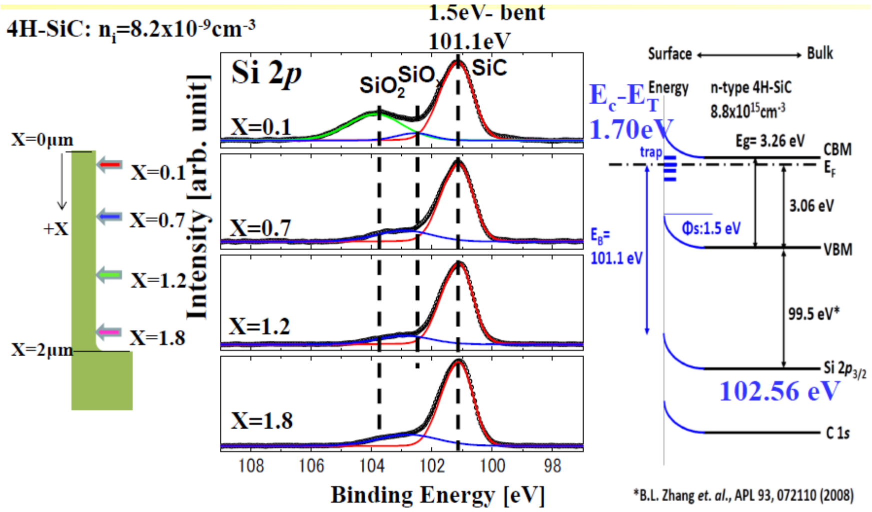

*B.L. Zhang *et. al.*, APL 93, 072110 (2008)

Fig. 4. Si 2*p* photoelectron spectra in a narrow scan mode with the deconvoluted components from four different positions (X= 0.1, 0.7, 1.2, and 1.8 μm from the surface) of the SiC trench sidewall, and a schematic band diagram for the m-plane SiC sidewall caused by RIE.

STUDY ON INTERFACIAL HYDROGEN-BOND STATES IN ELECTRON-PROTON-CORRELATED ORGANIC HETEROBILAYERS

Hiroyuki S. Kato [a], Susumu Yamamoto [b], Akira Ueda [b], Shinya Yoshimoto [b], Hatsumi Mori [b],
Jun Yoshinobu [b], Hiroki Wadati [b], Iwao Matsuda [b]
[a] *Graduate School of Science, Osaka University,*
[b] *The Institute for Solid State Physics, The University of Tokyo*

Introduction

Recently, new organic functional materials that show the proton (H^+) dynamics coupled with electrical conductivity have been reported [1,2]. In the organic crystal consisting of catechol-fused tetrathiafulvalene derivative (Cat-TTF), the change in the position of H^+ in the hydrogen bonds (HBs) induces charge redistribution of the π electrons in the molecules, which results in the switching of electrical conductivity [1,2]. Although the novel “proton-electron” concerted functionality of Cat-TTF has been achieved in 3D crystals, it should be necessary to reduce the dimensionality to 2D when one considers its application in organic electronic devices. In the previous study, hence, we designed the proton-electron correlated bilayers and created them in a way of self-assembly [3]. The bilayer consists of the catechol-fused bis(methylthio)tetrathiafulvalene (H_2Cat-BMT-TTF) molecular layer as a H^+ donor and the imidazole-terminated alkanethiolate self-assembled monolayer (Im-SAM) as a H^+ acceptor (Fig. 1). When the pairs of H^+ donor and acceptor provide strong HBs, the H^+ transfer along the HBs becomes easier in the bilayer and thus the conductivity of the Cat-TTF layer may become more controllable. In this study, therefore, we aimed to elucidate the characteristics of the interfacial HB states in the heterobilayer for creating the 2D proton-electron correlated systems on a substrate [4].

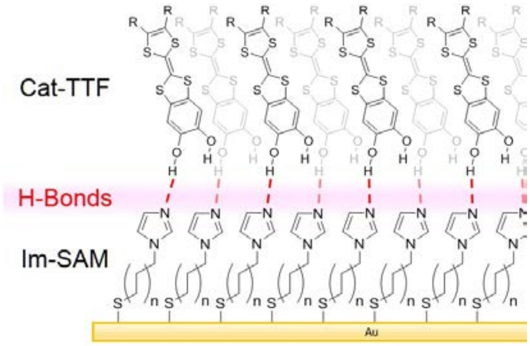

Fig. 1. Schematic chemical structures of the self-assembled heterobilayer consisting of the Cat-TTF layer and Im-SAM on an Au substrate.

Experimental

The organic heterobilayer on an Au surface was prepared by sequential two-step immersion of the Au substrate deposited on cleaved mica (Au film thickness of 200 nm, Phasis) in individual solutions of the organic compounds. First, the clean Au substrate was immersed in a deoxygenated ethanol solution containing 1 mM of 1-(11-mercaptoundecyl)-imidazole ($Im-(CH_2)_{11}-SH$; 96%, Sigma-Aldrich) for $\geq$ 20 h. This produced a well-packed Im-SAM on Au. Secondly, the Im-SAM/Au sample was immersed in a deoxygenated chloroform solution containing 1 mM of the synthesized H_2Cat-BMT-TTF for $\geq$ 20 h. All immersion processes were carried out under dry N_2 atmosphere in a glove box at room temperature. Further details of sample preparation can be found in the previous publication [3].

The element- and site-specific molecular interactions in the organic bilayer were investigated by NEXAFS. The NEXAFS experiments were carried out at soft X-ray beamline BL07LSU at SPring-8. The spectra were recorded in total electron yield (TEY) by measuring the sample drain current. The incidence angle of the p-polarized soft X-ray was set to 54.7° from the sample surface, i.e., “magic angle”. The incident soft X-ray beam was defocused to ~60 μm (H) × ~30 μm (V) to avoid beam damage of the organic molecules. All NEXAFS spectra were measured in UHV (base pressure of $\sim 5 \times 10^{-6}$ Pa) at 300 K. The NEXAFS spectra were normalized with the incident photon flux measured by the drain current of the Au mesh and then, a linear background determined by the slope at the nitrogen preedge region

(396−399 eV) was subtracted. Further details of NEXAFS measurements can be found in our recent publication [4].

Results and Discussion

By the design of our heterobilayer, the OH group of catechol and imino N in the imidazole group may make HB (Fig. 2). In fact, the interfacial HB states in the heterobilayer are characterized by a broadened and highly red-shifted band of O-H stretching vibrations observed by infrared reflection absorption spectroscopy [3]. This is the clear evidence of strong HBs of the H^+ donors. However, it was not clear that imino N works as the H^+ accepter in HBs. Hence, the N K-edge NEXAFS was conducted to specify the complete picture of interfacial HB states [4]. The element specificity of NEXAFS allows elucidation of the nature of HB at the H^+ acceptor side because N atoms exist only in the Im-SAM.

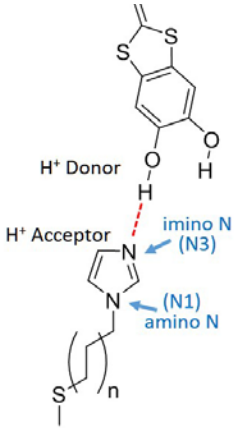

Fig. 2. Schematic chemical structures and a hydrogen bond at the interface between the Cat-TTF layer and Im-SAM.

Figure 3 shows the N K-edge NEXAFS spectra of Im-SAM/Au and H_2Cat-BMT-TTF adsorbed on Im-SAM/Au. The sharp peaks at 400.0 eV and 401.8 eV are ascribed to the N 1s → 1π* transition of the imino N (N3) and amino N (N1) atoms, respectively, of the imidazole ring in Im-SAM. In comparison between the spectra before and after the H_2Cat-BMT-TTF adsorption, the π* peak of imino N (N3) shifts from 400.0 eV to 400.3 eV, while that of amino N (N1) remains at the same energy. This shows that the adsorption of H_2Cat-BMT-TTF changes only the chemical environment of imino N, by making HBs. Based on the deconvolution analysis, the ratio of the shifted component to the total imino N is determined to be 0.41. These results depict the interfacial HB states in the heterobilayer as that closely half of imino N makes strong HB with the OH groups of H_2Cat-BMT-TTF.

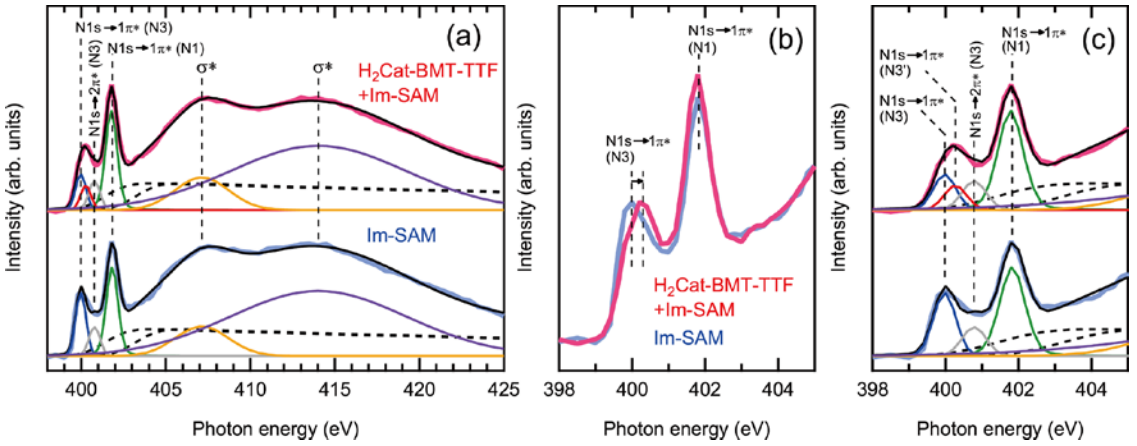

Fig. 3. N K-edge NEXAFS spectra of Im-SAM and H_2Cat-BMT-TTF adsorbed on Im-SAM: (a) Whole absorption, (b) enlarged π* peak regions (raw data), and (c) enlarged π* peak regions (raw data and fit data) [see details in Ref. 4]. The NEXAFS spectra were fit by up to six Gaussian peaks for the excitation of a core electron to π* and σ* states, and two step functions for the excitation of a core electron to a continuum. Two step functions originate from two different N atoms in Im-SAM; imino N (N3) and amino N (N1) atoms.

REFERENCES

[1] T. Isono, *et al.*, Nat. Commun. **4**, 1344 (2013).
[2] A. Ueda, *et al.*, J. Am. Chem. Soc. **136**, 12184 (2014).
[3] H.S. Kato, *et al.*, Langmuir **34**, 2189 (2018).
[4] S. Yamamoto, *et al.*, e-J. Surf. Sci. Nanotechnol. **17**, 49 (2019).

OPERANDO OBSERVATION OF METHANE ACTIVATION ON HETEROGENEOUS CATALYSTS BY AMBIENT-PRESSURE XPS

Takanori Koitaya[1,2], Susumu Yamamoto[3], Iwao Matsuda[3], Jun Yoshinobu[3], and Toshihiko Yokoyama[1]

[1] *Institute for Molecular Science, National Institutes of Natural Sciences*

[2] *Japan Science and Technology Agency, Precursory Research for Embryonic Science and Technology*

[3] *The Institute for Solid State Physics, The University of Tokyo*

Chemical transformation of methane to valuable chemicals is an attracting, but challenging research topic. Activation of inert methane molecules on metal or metal-oxide surfaces is an important process for catalytic conversion [1]. In order to detect reaction of physisorbed methane molecules, (near) ambient-pressure condition is indispensable, since dissociative sticking probability of methane is very small [2]. In this study, the reaction of methane with preadsorbed oxygen on Pd(110) and a PdO thin film was investigated by XPS under ultrahigh vacuum and ambient-pressure XPS (AP-XPS).

XPS experiments were performed using the AP-XPS apparatus in BL07LSU [3]. The Pd(110) sample was cleaned by sputtering and annealing in the preparation chamber (base pressure = 3×10^{-10} mbar). The oxygen-preadsorbed Pd(110) (O-Pd(110)) was prepared by exposure of 22 mbar oxygen on Pd(110) at room-temperature for 1500 s. The PdO thin film on Pd(110) (PdO-Pd(110)) was formed by heating the sample to 770 K in the presence of 1 mbar oxygen.

Figure 1(a) shows a series of Pd 3p and O 1s spectra of the O-Pd(110) surface as a function of methane exposure. Methane molecules were exposed on the surface at room-temperature. By the reaction of methane with preadosorbed oxygen, the adsorbed amount of oxygen was gradually decreased. Concomitantly, peaks of oxygen-adsorbed Pd atoms in Pd 3d core-level (Fig. 2b) decreased in intensity. Fig. 1(c) shows change in the coverage of oxygen atoms. The oxygen coverage was steeply decreased at low methane exposure, indicating that reaction probability of methane is higher at high oxygen coverage than those at lower oxygen coverage.

Fig. 2 (a) and (b) show Pd 3p, O 1s and Pd 3d spectra of PdO-Pd(110) surface under 0.4 mbar methane atmosphere as a function of sample temperature. The methane gas was introduced into the gas-cell at sample temperature of 300 K, followed by heating in the presence of methane. The reaction of methane did not occur on the PdO thin film at room temperature. The sample was reduced by heating above 450 K. These results indicate that methane reactivity is much lower on the PdO thin film formed on Pd(110) than on the oxygen-preadsorbed Pd (110) surface.

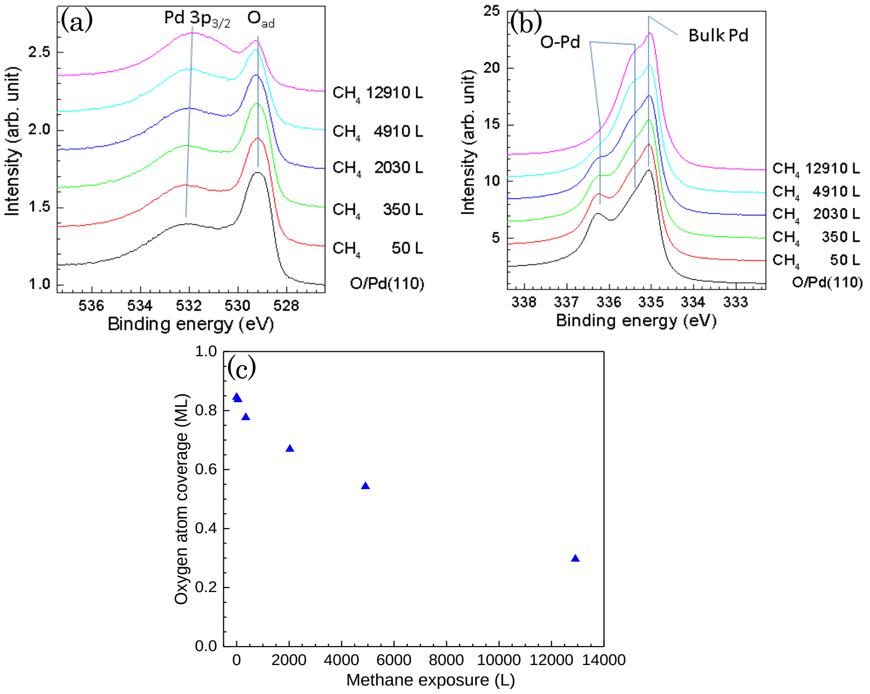

Fig. 1 (a) Pd 3p and O 1s, and (b) Pd 3d core-levels of oxygen-preadsorbed Pd(110) as a function of methane exposure. Methane was dosed on the surface at room temperature. (c) Oxygen coverage estimated from O 1s intensity.

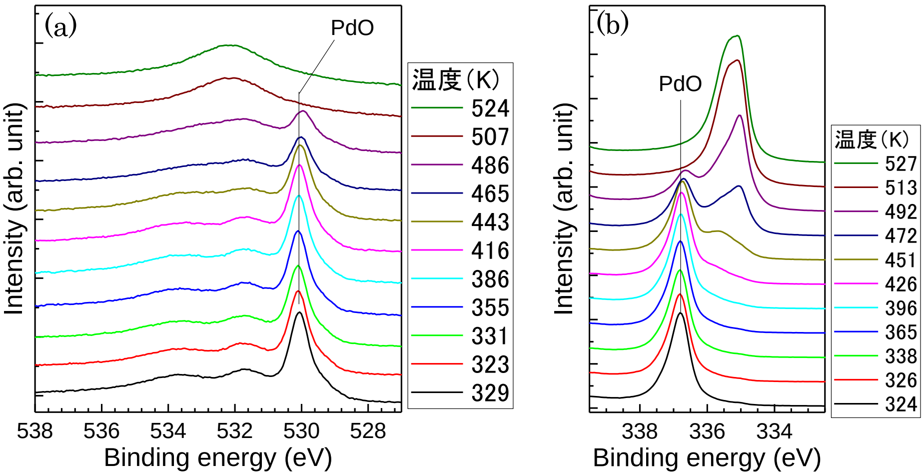

Fig. 2 (a) Pd 3p, O 1s, and (b) Pd 3d AP-XPS spectra of the PdO thin film on Pd(110) as a function of sample temperature. A series of spectra was measured in the presence of 0.4 mbar methane.

REFERENCES

[1] R. Horn and R. Schlögl, Catal. Lett. **145**, 23 (2014).

[2] R. A. Campbell, J. Szanyi, P. Lenz, and D. W. Goodman, Catal. Lett. **17**, 39 (1993).

[3] T. Koitaya *et al.*, Top. Catal. **59**, 526 (2015).

SYNERGETIC EFFECT AT METAL-OXIDE INTERFACE ON METHANE ACTIVATION MEASURED BY AMBIENT-PRESSURE XPS

Takanori Koitaya[1,2], Susumu Yamamoto[3], Iwao Matsuda[3], Jun Yoshinobu[3], and Toshihiko Yokoyama[1]
[1] Institute for Molecular Science, National Institutes of Natural Sciences
[2] Japan Science and Technology Agency, Precursory Research for Embryonic Science and Technology
[3] The Institute for Solid State Physics, The University of Tokyo

The interfacial interaction between metal and metal oxide significantly affects reactivity of heterogeneous catalysts [1]. The metal particle on the oxide support is often decorated or encapsulated by the metal-oxide thin film through the strong metal-support interaction (SMSI) [2]. Metal-oxide thin films deposited on metal substrates are thus a good model system to examine the SMSI effect in catalysis. Recently, we have studied CO_2 hydrogenation on Zn-deposited Cu surfaces, and revealed that surface oxidation states depend on reaction conditions, such as sample temperature and gas composition [3]. Therefore, *in situ* observation of catalysts during reaction is indispensable for elucidation of chemical states of working catalysts.

Ambient-pressure X-ray photoelectron spectroscopy (AP-XPS) is now widely applied for many reaction systems for real time observation of electronic structures of catalysts and reaction intermediates on the surface under reaction condition [4]. In particular, soft X-ray AP-XPS is suitable for investigation of chemical states of a thin film deposited on the surface, since it is surface-sensitive technique due to low kinetic energy of photoelectron. In this study, redox properties of the Ir-deposited Pd(110) surface were investigated by AP-XPS.

The sample preparation and AP-XPS measurements were carried out in ultrahigh vacuum chambers (base pressure: 3×10^{-10} mbar). Iridium was deposited on the Pd(110) surface at room temperature using electron-beam evaporator (Scienta Omicron, EFM 3). The coverage of Ir was estimated to be 1.7 ML. After the preparation of the Ir-deposited Pd(110) model catalyst, AP-XPS measurements of redox reactions were conducted in the gas-cell at room temperature.

Figure 1 shows Pd 3d and Ir 4f AP-XPS spectra measured under 1 mbar oxygen at sample temperature of 300 K as a function of elapsed time. The Pd 3d spectra show gradual growth of an oxygen-adsorbed Pd peak (O-Pd). Oxidation of the substrate to PdO was not observed in this reaction condition. In contrast, the Ir 4f spectra show oxidation of deposited Ir from a metallic state to IrO_2 oxide. Note that total intensity of the Pd 3d peaks decreased as the oxidation of Ir proceeds. This indicates that Ir atoms were segregated on the surface, and an IrO_2-Pd(110) interface was formed in the presence of 1 mbar oxygen.

Figure 2 shows a series of Pd 3d and Ir 4f AP-XPS spectra of the IrO_2-Pd(110) interface under 0.4 mbar methane at 300 K. By the reaction with methane, atomic oxygen on Pd atom was removed, and the IrO_2 thin film was reduced to a metallic state. Thus, the Ir-deposited Pd(110) surface is oxidized by O_2 and reduced by methane at room temperature. In the case of the bare Pd(110) surface, oxidation and formation of a PdO thin film occur at much higher temperature (about 600 K). In addition, the PdO thin film was reduced to metallic Pd by heating to 450 K in the presence of 0.4 mbar methane. These experimental results indicate that the redox reactivity is significantly improved by the deposition of Ir atoms on the Pd(110) surface.

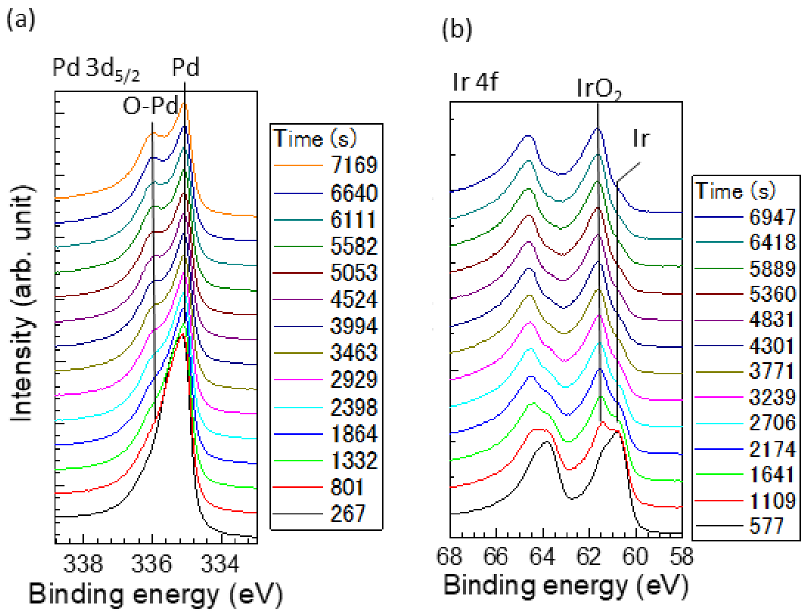

Figure 1. (a) Pd 3d and (b) Ir 4f core-level spectra of Ir-deposited Pd(110) measured under 1 mbar oxygen atmosphere as a function of elapsed time. During the measurement, the sample was kept at 300 K.

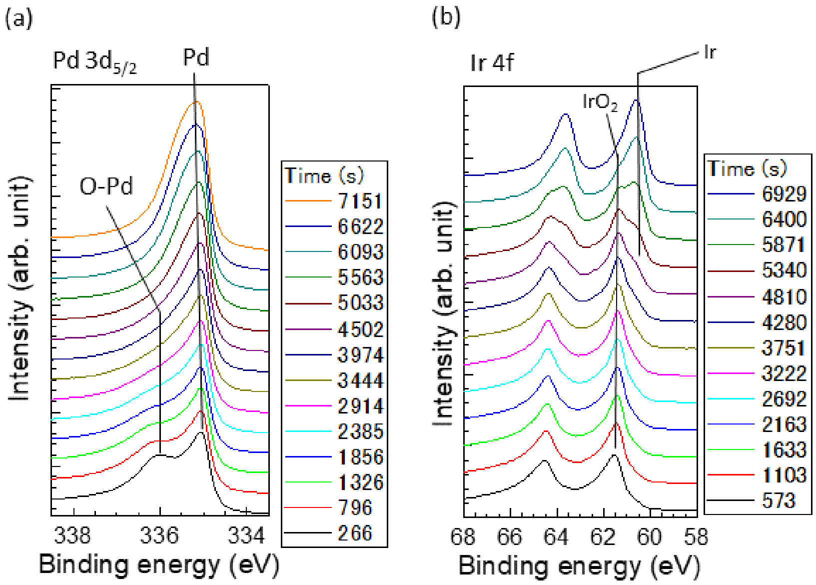

Figure 2. (a) Pd 3d and (b) Ir 4f core-level spectra of IrO_2-Pd(110) in the presence of 0.4 mbar methane as a function of elapsed time. The sample temperature was 300 K.

REFERENCES

[1] S. Shaikhutdinov and H. J. Freund, Annu. Rev. Phys. Chem. **63**, 619 (2012).
[2] Q. Fu and T. Wagner, Surf. Sci. Rep. **62**, 431 (2007).
[3] T. Koitaya *et al.*, ACS Catalysis **9**, 4539 (2019).
[4] D. E. Starr, Z. Liu, M. Hävecker, A. Knop-Gericke, and H. Bluhm, Chem. Soc. Rev. **42**, 5833 (2013).

CHEMICAL STATE ANALYSIS OF INTERMEDIATE WATER BOUNDED BY BIOCOMPATIBLE POLYMERS

Masahiro Kunisu[1], Masaru Nakada[1], Koichi Ozaki[1], Junpei Yahiro[1],
Yitao Cui[2], Kosuke Yamazoe[2], Jun Miyawaki[2] and Yoshihisa Harada[2]
[1]*Toray Research Center, Inc.,*
[2]*Synchrotron Radiation Laboratory, The Institute for Solid State Physics, The University of Tokyo*

Biocompatibility is one of the important performance indicators for polymers used in medical materials. It is thought that adsorbed water on the polymer surface contributes to the expression of biocompatibility. At the biocompatible polymer interface, there are roughly three types of water classified as free water, intermediate water, and antifreezing water. It is considered that the intermediate water plays an important role in the expression of biocompatibility. However, the local structural and dynamical properties of intermediate water are still unknown. In this project, it aims at studying water contained in biocompatible polymer in detail, using soft X-ray absorption spectroscopy (XAS) by O *K*-edge core excitation and (resonant) soft X-ray emission spectroscopy (XES/RIXS) by successive emission from oxygen valence to the excited core states after XAS.

Polyvinyl pyrrolidone (Poly Vinyl Pyrrolidone $(C_6H_9NO)_n$: PVP) and polyethylene glycol (Poly Ethylene Glycol $(C_2H_4O)_n$: PEG) were used as the biocompatible polymer. For PVP and PEG, an aqueous solution was prepared as a measurement sample at a polymer concentration of 5 wt% - 65 wt%, along with absolutely dry polymer powders as an estimate of background. The O *K*-edge XAS measurements were performed in the energy range from 520 to 550 eV. The XES measurements were performed under ionization excitation energy of 550 eV. In the RIXS analysis resonant excitation to the pre-edge (535 eV), main-edge (537 eV), and post-edge (541 eV) in the XAS spectrum of water were used. Moreover, measurement was also performed with excitation energy near the resonance to the C = O carbonyl π^* state (near 532 eV). The measurement of the polymer aqueous solution was carried out using an originally developed solution cell at room temperature and under ambient pressure environment by circulating the solution.

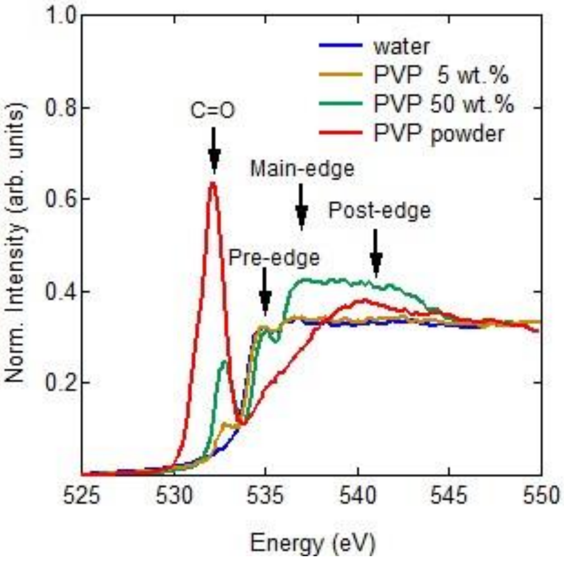

Figure 1. O *K*-edge XAS spectrum of PVP aqueous solution with a polymer concentration of 5 wt%(yellow) and 50 wt%(green), PVP powder(red), and pure water(blue).

Figure 1 shows XAS spectra of PVP aqueous solution with a polymer concentration of 5 wt% and 50 wt%, PVP powder, and pure water. Peaks at 532.7 eV for the aqueous PVP solution and at 532.2 eV for the PVP powder are considered to be attributed to C = O (carbonyl). In the PVP aqueous solution, as the concentration decreased, the peak intensity also decreased, and a clear correlation was found between the concentration of the polymer aqueous solution and the peak intensity.

In this experiment, XES / RIXS analysis was also performed. In the RIXS analysis, the energy shown by the arrow in Fig. 1 was used as the excitation energy. In the near future, we plan to proceed the analysis of the obtained results and compare them with the previous results to investigate in more detail the characteristics and electronic state of water contained in the biocompatible polymers.

SIZE AND TEMPERATURE DEPENDENCE OF HYDROGEN-STORAGE IN Pd NANOPARTICLES

Seo Okkyun[1], Jiayi Tang[2], Takanori Koitaya[3], Susumu Yamamoto[4], Chulho Song[1],
Iwao Mastuda[4], Jun Yoshinobu[4], Osami Sakata[1]
[1] National Institute for Materials Science, [2]Departnment of Engineering, University of Hyogo,
[3]Institute for Molecular Science, [4]The Institute for Solid State Physics, The University of Tokyo

Introduction

Research into the interaction between metals and hydrogen is very important for the development of potential applications, such as advanced materials for hydrogen storage and purification. Among these catalysts, Pd nanoparticles (NPs) are known as the classic models for the clarification of hydrogen-storage properties of metal nanoparticles [1-5]. It is reported that the hydrogen absorption/desorption processes during the hydrogen-storage leads to a large expansion of the Pd lattice, which is called as α-β phase transition [2]. In addition, hydrogen atoms can be trapped strongly in the Pd NPs compared with Pd bulk catalysts because of the larger surface area to volume ratio [3,4]. Recently, many studies have been conducted on the structures effects on the catalyst performance of Pd NPs, however, *in-situ* observations of hydrogen adsorption/desorption mechanisms on Pd nanoparticles with specific surface depending on nanoparticle size under the ambient pressure are lacked. In this study, the valence band as well as the core-level photoelectron spectra of Pd NPs were investigated under the ambient hydrogen atmosphere to characterize the size dependence of hydrogen absorption process.

Experimental

The Pd cube shaped NPs samples with size of 12 and 20 nm are prepared in aqueous solution by reducing Na_2PdCl_4 with citric acid in the presence of PVP [6]. The size and crystalline structure of Pd NPs were characterized by TEM and XRD measurements. The Pd microparticles with 1 μm size were measured as a reference sample. The hydrogen absorption were observed under H_2 atmosphere at 2.0 mbar at 300, 373, and 473 K by using ambient pressure X-ray photoelectron spectroscopy system at BL07LSU. Pure H_2 (> 99.99999%) gas was introduced into an ambient-pressure gas cell, where the base pressure was below 5×10^{-10} Torr. An electron analyzer (SPECS, Phoibos 150) was assembled with a three-stage differential pumping system. The Pd 3*d* core-level and valence band spectra were observed at a photon energy of 1200 eV.

Results and Discussion

Figures 1 (a)-(c) show the Pd $3d_{5/2}$ spectra measured before hydrogen exposure and during hydrogen absorption at 2.0 mbar at 300, 373, and 473 K for 12 nm Pd NPs, for 20 nm Pd NPs, and Pd microparticles, respectively. Pd $3d_{5/2}$ spectra observed before hydrogen exposure on three samples were fit well with two components, which are located at 334.8 eV and 335.4 eV. The component at lower binding energy (BE) is assigned as Pd atoms from the bulk (Pd bulk), another one at higher BE is assigned as Pd carbide (Pd-C). After hydrogen exposure at 2.0 mbar at 300 K, one new component appeared at BE of 335.1 eV on the Pd NPs surface. It can be assigned as the Pd hydride (Pd-H), which is generally located at lower BE relative to Pd-C. On the other hand, there is almost no Pd hydride formed on Pd microparticles during hydrogen exposure at 300 K. Moreover, the amount of Pd hydride formed on 12 nm Pd NPs is more than that on 20 nm Pd NPs, indicating the hydrogen absorption rate is higher with decreasing the particle size. The hydrogen absorption was enhanced on both Pd NPs and Pd microparticles by increasing the temperature. In the meantime, the Pd carbide was reduced because of the carbon diffusion into the bulk with the increase of temperature, which produced more absorption sties for hydrogen atoms. We suggested that the increase of the absorption sites enhance the hydrogen absorption rate. Figures 2 (a)-(c) show the valence band spectra observed on the Pd NPs and Pd microparticles under the same condition. The valence band spectra near Fermi edge was increased after hydrogen exposure on Pd NPs, whereas there was no changes on Pd microparticles. First-principle simulations of the valence band will be carried out to compared with the experiment results to explain the detailed electronic properties during hydrogen adsorption/absorption.

REFERENCES

[1] R. Griessen *et al.*, Nature Mater. 15 (2016) 311-317.
[2] A. Baldi *et al.*, Nature Mater. 13 (2014) 1143-1148.
[3] C. Wadell *et al.*, Chem. Phys. Lett. 603 (2014) 75-81.
[4] S. Syrenova *et al.*, Nature Mater. 12 (2013) 905-912.
[5] R. Bardham *et al.* Nature Mater. 15 (2016) 311-317.
[6] G. Li *et al.*, Nature Mater. 13 (2014) 802-806.

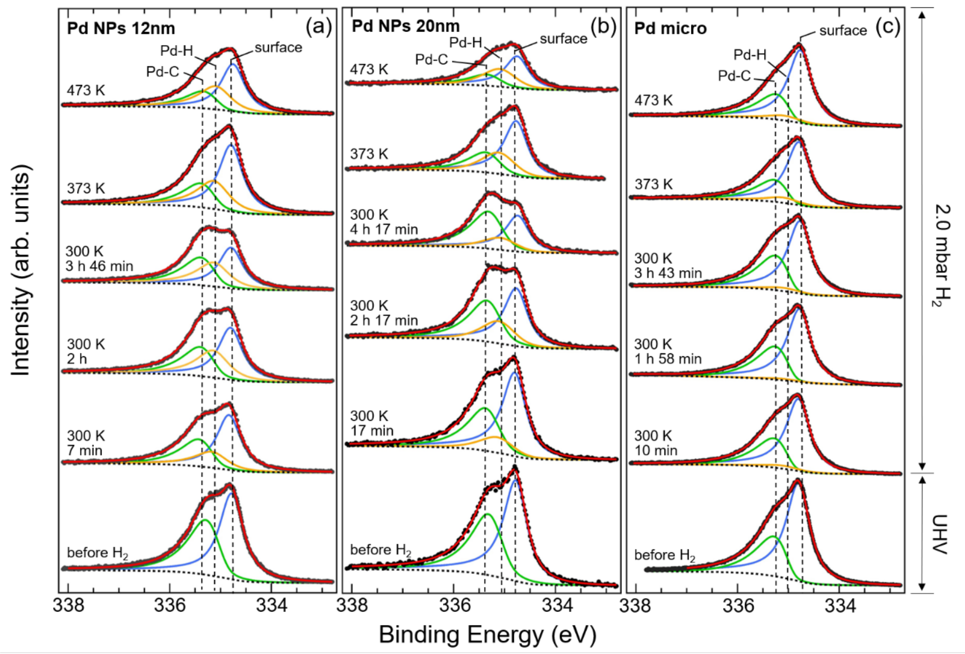

Fig.1 Pd 3d5/2 spectra measured before H_2 exposure and during hydrogen absorption at 300 K, 373 K and 473 K on (a) Pd nanoparitles (12 nm), (b) Pd nanoparitles (20 nm) and (c) Pd microparticle.

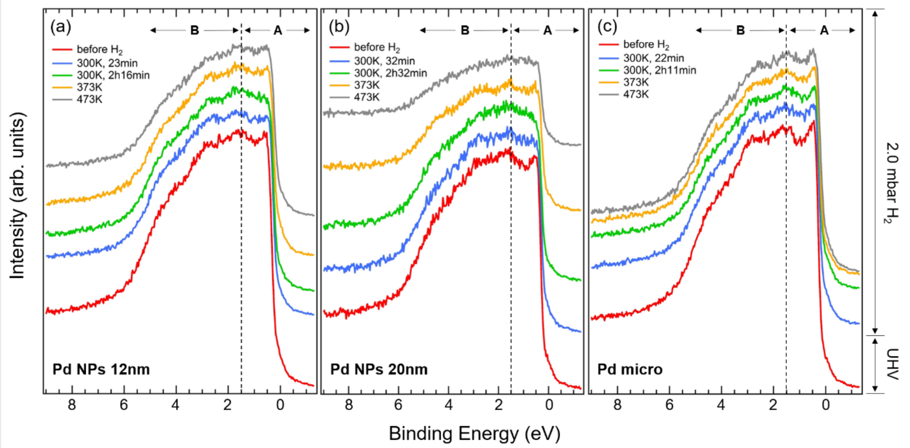

Fig.2 valence band spectra measured before H_2 exposure and during hydrogen absorption at 300 K, 373 K and 473 K on (a) Pd nanoparitles (12 nm), (b) Pd nanoparitles (20 nm) and (c) Pd microparticle.

ELUCIDATION OF BAND ALIGNMENT AT SEMICONDUCTOR/ELECTROLYTE INTERFACE BY X-RAY PHOTOELECTRON SPECTROSCOPY

Yuki Imazeki[1], Masahiro Sato[2], Takahito Takeda[1], Masaki Kobayashi[1], Susumu Yamamoto[3], Iwao Matsuda[3], Jun Yoshinobu[3], Yoshiaki Nakano[1], and Masakazu Sugiyama[1,2]

[1]*Department of Electrical Engineering and Information Systems, The University of Tokyo*

[1]*Research Center for Advanced Science and Technology, The University of Tokyo*

[3]*The Institute for Solid State Physics, The University of Tokyo*

Photocatalytic water splitting is one of the most attractive technologies for storing sunlight. However, today's photocatalysts (photoelectrodes) still suffer from low efficiency or poor stability [1], and to overcome these problems, the physical basis of photoelectrochemical reactions has to be understood in more detail. Band alignment (, i.e., the relative position between the conduction band minimum (CBM) or the valence band maximum (VBM) of the semiconductor and the redox potentials in the electrolyte at the semiconductor/electrolyte interface,) determines whether the reaction of interest proceeds or not, and therefore is the key factor for photoelectrochemical reactions. Nevertheless, from an atomistic point of view, little is known about the photocatalyst(semiconductor)/electrolyte interface, and the relationship between the band alignment and the geometric structure at the interface remains unrevealed.

The recent development of ambient pressure X-ray photoelectron spectroscopy (AP-XPS) has made it possible to probe the geometric as well as the electronic structure of the semiconductor/electrolyte interface under nearly in situ conditions [2]. On the other hand, we have been exploring the band alignment at the semiconductor/electrolyte interface under the same environment as in the progress of photoelectrochemical water splitting [3]. The purpose of this research is to bridge the band alignment in the surface vicinity of n-GaN photoanode between the situation in vacuum to the condition of water splitting, using AP-XPS with controlled coverage of water molecules on the n-GaN surface.

An n-type GaN layer was grown epitaxially on a silicon substrate using metalorganic vapor-phase epitaxy (MOVPE) with a doping concentration of ca. 4×10^{18} cm^{-3}. X-ray photoelectron spectroscopy (XPS) of the GaN surface was conducted using SPring-8 BL07LSU beamline in order to quantify the band bending in the surface vicinity of the GaN. The amplitude of band bending was evaluated on the basis of the binding energy of Ga 3d peak with respect to the Fermi level.

Prior to XPS measurements, the surface of the GaN layer was treated with N_2 plasma in a vacuum environment and the periodic arrangement of surface atoms was confirmed by low-energy electron diffraction (LEED). In order to observe the change in band bending under light irradiation, ultraviolet light from Xe lamp was introduced onto the GaN surface through the quartz window of the specimen chamber. Water molecules were attached to the GaN surface by introducing water vapor (1.9 mbar in partial pressure) into the chamber while keeping the surface temperature to either 289 or 302 K.

Band bending under the dark condition was evaluated first. Under high-vacuum condition, band bending was 0.43 eV. Adsorption of water molecules on the GaN surface at 289 K reduced band bending to 0.032 eV. By increasing the surface temperature to 302 K, corresponding to the reduction in the amount of adsorped water molecules, band bending was slightly increased to 0.060 eV. Such reduction is band bending induced by the adsorption of water molecules is consistent with the previous report [4]. It seems that water molecules passivated the surface states of n-GaN and un-pinned the Fermi-level from the surface states. As depicted in Fig. 1, such almost flat-band conditions brought about by water adsorption seems is in contrast to the huge band bending which has been observed for the n-GaN surface adjacent to 1M NaOH aqueous solution [3]. This gap is a target of future investigation. By increasing the amount of water adsorbed on the GaN surface, further structural change in the GaN surface is anticipated.

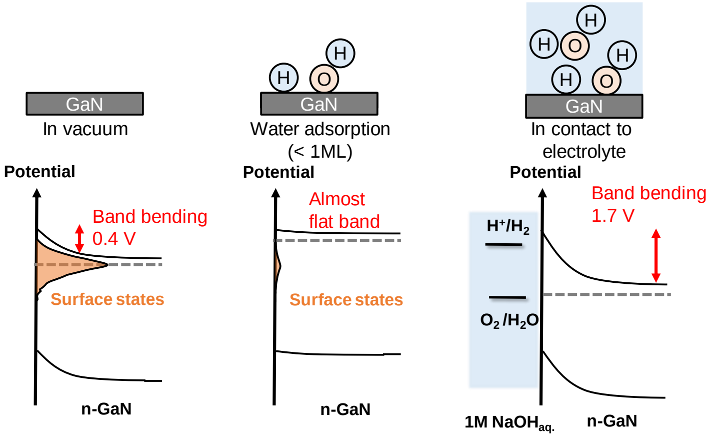

Fig. 1 Band alignment in the surface vicinity of n-GaN photoelectrode under dark.

The next analysis is the impact of light irradiation on the band bending with and without water adsorption on the n-GaN surface. Under the light intensity of this experiment (not quantitatively calibrated), the amplitude of band bending was decreased by 10 - 20 meV, to which the impact of water adsorption is not clear. For the n-GaN adjacent to 1M NaOH aqueous solution, much larger change in band bending has been observed, but further discussion needs the XPS measurement with more intense and variable light irradiation, which is the target of the future trial.

The initial results described here provides a perspective for the future experiment: it will be possible to analyze the band bending of n-GaN photoelectrode as a function of both the amount of adsorbed water molecules and light intensity.

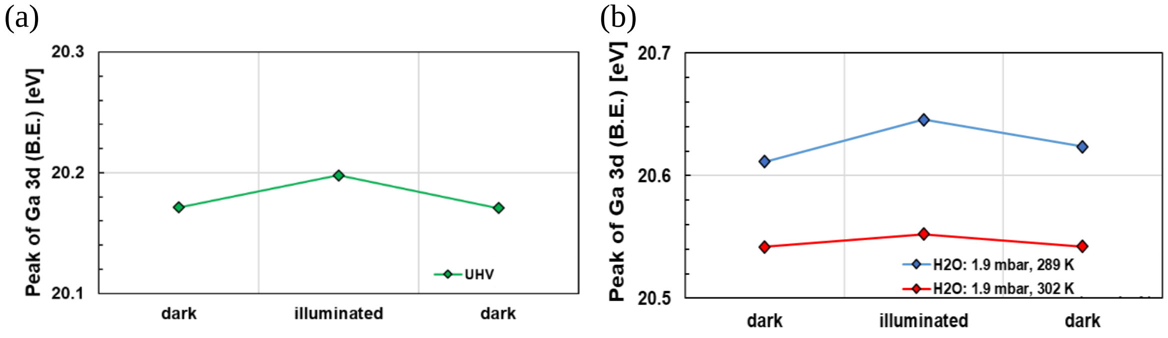

Fig. 2 The shift in Ga 3d peak position under dark and Xe-lamp illumination: (a) under vacuum, (b) with water adsorption at a GaN surface temperature of 289 and 302 K. The increased binding energy under light irradiation indicates the increased distance between the Fermi level and the Ga 3d level in the topmost surface of GaN, i.e., the reduction in band bending.

REFERENCES

[1] J. Liu et al., Science, **347**, 970, 2015.
[2] M. Lichterman et al., Energy Environ. Sci., **8**, 2409, 2015.
[3] Y. Imazeki et al., ECS Transactions, **77**, 25-30, 2017.
[4] P. Lorenz et al., Phys. Status Solidi C, **7**, 169–172, 2010.

STRUCTURE ANALYSIS OF BATIO$_3$ /PT (111)/SI QUASCICRYSTAL THIN FILM BY PHOTOELECTRON HOLOGRAPHY

Shun Fukami [a], Hiroki Momono [a], Masafumi Ogi [a], Peng Dawei [a], Yusuke Hashimoto [a], Hiroyuki Matsuda [a], Munetaka Taguchi [a], Stefan Förster [b], Wolf Widdra [b], Hiroshi Daimon [a]

[a]*Nara Institute of Science and Technology(NAIST),*

[b]*Martin-Luther-Universität Halle-Wittenberg*

Stefan *et al* [1)] focused on the BaTiO$_3$ (111) / Pt (111) thin film and succeeded to make Oxide Quasi-Crystal (OQC) on Pt (111) substrate by specific annealing steps. Their characteristic two-dimensional structures are revealed by STM and LEED technique. OQC not only has a 12-fold quasi-periodic structure called Stampfli-Gähler tiling, but it also changes to a more regular approximate crystal structure under an another annealing condition. Furthermore, the wetting mechanism on the substrate indicates that the OQC film has potential as a brand new device. However, there is still room for clarification of the local structure of each element.

We have conducted elemental selective experiments of two-dimensional oxide thin film using photoelectron holography technique. These experiments used BL07LSU beam line, which produces strong linear and circular polarizations in the soft x-ray region. Meanwhile, we used Display type ELlipsoidal Mesh Analyzer (DELMA) [2)], a unique device, to perform high energy resolution photoelectron diffraction measurements.

Fig.1 shows O 1s core-excited diffraction pattern from BaTiO$_3$ (111) islands. The pattern was operated by three-fold symmetry operation and mirror-symmetry operation. Distinctive diffraction rings derived from two-dimensional structures were confirmed in ultra-thin film pattern. This feature directly indicates that the local structure around O atoms have changed dramatically by the additional annealing treatment. Fig. 2 shows a local atomic model around oxygen constructed from the O1s using holographic transformation. From this result, we clearly show that two-dimensional photoelectron holography is a very effective tool for the analysis of ultrathin films.

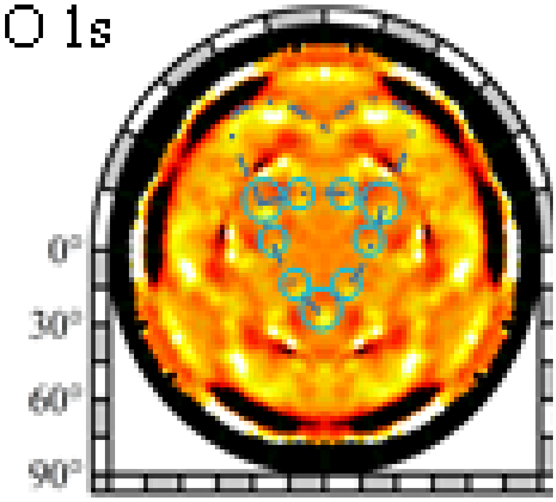

Fig.1 O 1s core photoelectron diffraction pattern from BaTiO$_3$ (111) .

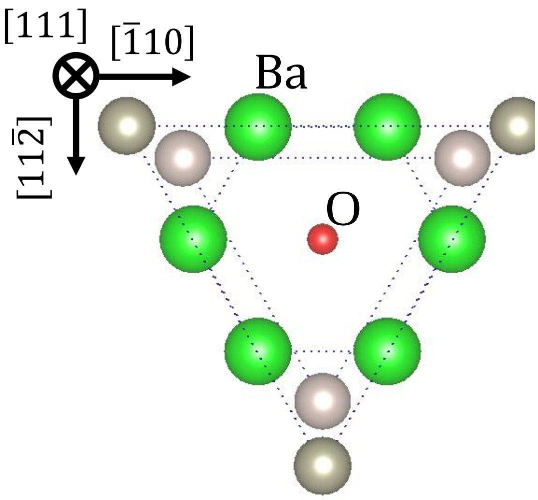

Fig.2 Local atomic structural model around O.

This work was performed with the approval of the Japan Synchrotron Radiation Institute, Proposal No. 2014A7462, 2014B7476, 2015A7488, 2017B7554 and 2018A7569, and supported by Japan Society for the Promotion of Science Grant-in-Aid for Scientific Research on Innovative Areas: Grant Number 26105001.

REFERENCES

[1] Stefan Förster, Klaus Meinel, René Hammer, Martin Trautmann & Wolf Widdra, Nature **502**, 215-218 (2013).

[2] K. Goto, H. Matsuda, M. Hashimoto, H. Nojiri, C. Sakai, F. Matsui , H. Daimon, L. Tóth, T. Matsushita, e-J. Surf. Sci. Nanotech. **9**, 311-314 (2011).

PHOTOINDUCED DYNAMICS IN $Ba_3CuSb_2O_9$ WITH Cu 3*d* ORBITAL LIQUIDS MEDIATED BY OXYGEN 2*p* HOLES

Kou Takubo,[1,2] Kohei Yamamoto,[1] Yujun Zhang,[1,3] Yasuyuki Hirata,[1] Hiroki Wadati,[1,3]
Huiyuan Man,[1] Satoru. Nakatsuji,[1] Takashi Mizokawa[4]

[1]*The Institute for Solid State Physics, The University of Tokyo*
[2]*Department of Chemistry, Tokyo Institute of Technology*
[3]*Graduate School of Material Science, University of Hyogo*
[4]*Department of Applied Physics, Waseda University*

Quantum spin liquids in Mott insulators usually emerge in geometrically frustrated magnets. Less commonly, unfrustrated magnets can show a variety of quantum spin liquids if charge and/or orbital degrees of freedom are involved. $Ba_3CuSb_2O_9$ harbors orthorhombic phase and hexagonal phase. Jahn-Teller distortion of $Cu^{2+}O_6$ octahedra is absent only in the hexagonal $Ba_3CuSb_2O_9$ suggesting a Cu 3*d* spin-orbital liquid [1,2]. Many previous experiments indicated that the spin-orbital liquid phase in the hexagonal $Ba_3CuSb_2O_9$ is associated with a dynamical character of fluctuation in the orbital sector. However, the real microscopic origin of this behavior was still not clarified in these studies. A puzzle is that the same material seems to exist in the two different modifications. The orthorhombic phase behaves quite normally: it shows a cooperative JT distortion, no special dynamic effects, *etc*. On the other hand, the hexagonal phase has all these strange features argued above.

In order to clarify the microscopic origin for this different behavior, we measured x-ray absorption spectroscopy (XAS) and time-resolved resonant soft x-ray scattering (Tr-RSXS) at BL07LSU of SPring-8 for two phases of $Ba_3CuSb_2O_9$. Single crystals of $Ba_3CuSb_2O_9$ were grown under oxygen atmosphere from the $BaCl_2$-based flux [2]. The samples were cleaved along the (001) plane *in situ* to avoid the surface contamination. The XAS spectra were recorded both using the total electron yield (TEY) and total fluorescence yield (TFY) modes. The Tr-RSXS measurement was performed using the pump-probe technique with a time-resolution of ~50 ps [3]. A second-harmonic Ti:sapphire laser pulse ($h\nu$=3.1 eV, repetition rate = ~ 1 kHz, width = 50 fs) was adopted as the pump light, which was introduced from the laser station of BL07LSU.

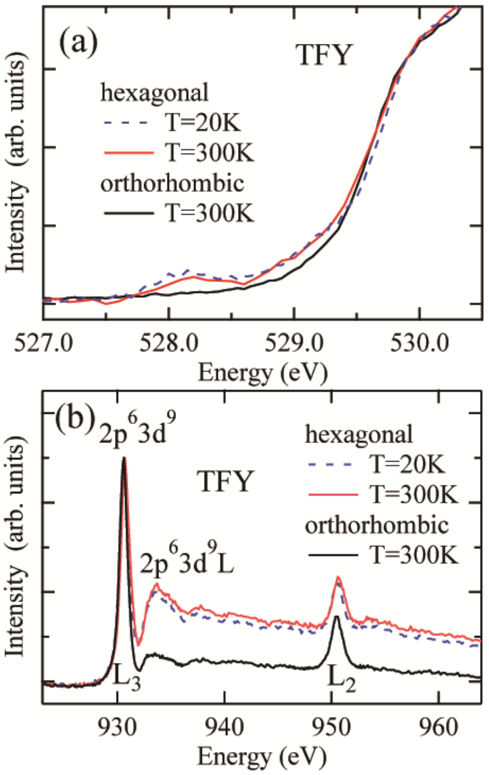

Fig. 1 Typical XAS spectra at the (a) O K and (b) Cu L edges for the hexagonal and orthorhombic phases of $Ba_3CuSb_2O_9$ taken in the TFY mode.

Figure 1 shows TFY-XAS spectra at the O K and Cu L edges of $Ba_3CuSb_2O_9$. The Cu L_3 main peak at 930.2 eV is accompanied by the charge transfer satellite at about 933 eV. The intensity of the satellite seems to be rather large in the hexagonal phase compared to the orthorhombic phase. The main and satellite peaks are assigned to the transitions of $2p^63d^9$ to $2p^53d^{10}$ and of $2p^63d^9\underline{L}$ to $2p^53d^{10}$ [4]. Here $\underline{L}$ represents a hole on the oxygen 2*p* orbitals. The Cu 2*p* XAS indicates that the ground state of the hexagonal phase includes more $3d^9\underline{L}$ than the orthorhombic phase. On the other hand, the structure at 530 eV observed at O K edge spectra of Fig. 1(a) can be assigned to the transition from 1*s* to 2*p* which is hybridized into the upper Hubbard band. The peak at 528.2 eV is observed only in the hexagonal region and can be assigned to the Zhang-Rice singlet band seen in the hole doped high-*Tc* cuprates: the transition from oxygen 1*s* to unoccupied oxygen 2*p* (corresponding to "3*d*9*L to* 3*d*9") [5].

Figure 2 shows the dynamics of Tr-RSXS at Q=(002) with *hv*=930.2 eV on the Cu L resonance after the pump pulse at 3.1 eV. A coherent oscillation with period of ~165 ps (~6 GHz) is observed in the hexagonal phase while no oscillation seems to be not observed in the orthorhombic phase. In addition, the x-ray scattering signals probed at 923.0 eV below the absorption edge do not show appreciable change after the pump pulse. The observed coherent oscillation of ~6 GHz is rather slow compared to various optical phonons in the system which are usually coupled to charge or orbital orderings. Such a slow dynamics in the hexagonal phase is consistent with the expectations in the previous reports [6,7].

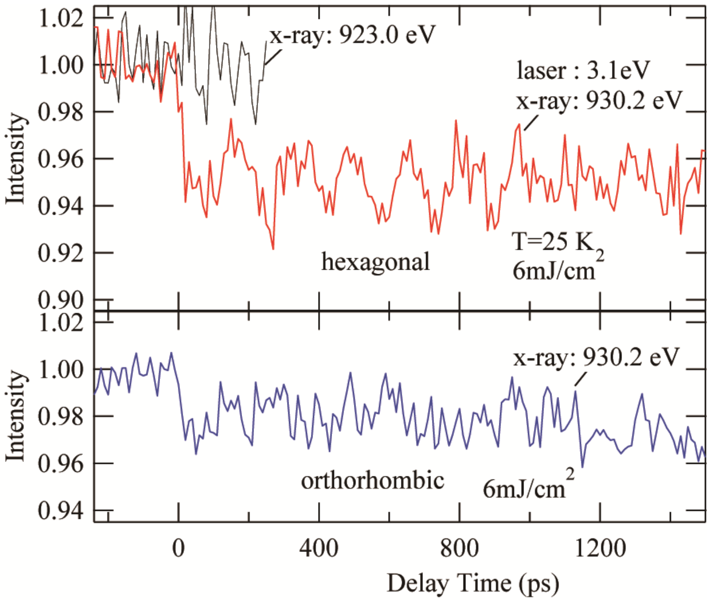

Fig. 2 Time-revolution of the Tr-RSXS signals at Q=(002) for the hexagonal and orthorhombic and phases after the pump-pulse of

To summarize, x-ray absorption spectroscopy on $Ba_3CuSb_2O_9$ reveal that the hexagonal phase with spin and orbital liquid is characterized by emergence of oxygen 2*p* hole in the highly insulating state. The coherent oscillation in the pump-probe resonant x-ray scattering measurement suggests that the spin-charge-orbital fluctuation in the hexagons of Cu sites can be controlled by optical laser.

REFERENCES

[1] S. Nakatsuji *et al.*, Science **336**, 559 (2012).
[2] H. Man *et al.*, J. Phys.: Condens. Matter **30,** 443002 (2018).
[3] K. Takubo *et al.*, Appl. Phys. Lett. **110**, 162401 (2017).
[4] T. Mizokawa *et al.*, Phys. Rev. Lett. **67**, 1638 (1991).
[5] C. T. Chen *et al.*, Phys. Rev. Lett. **66**, 104 (1991).
[6] Y. Ishiguro *et al.*, Nature Comm. **4**, 2022 (2013).
[7] Y. Han *et al.*, Phys. Rev. B **92**, 180410(R) (2015).

AMBIENT-PRESSURE XPS STUDIES OF CO_2 HYDROGENATION ON PD-BASED BIMETALLIC ALLOY CATALYSTS

Jiayi Tang[1], Takanori Koitaya[2], Susumu Yamamoto[3], Okkyun Seo[4], Kozo Mukai[3], Iwao Mastuda[3], Jun Yoshinobu[3]

[1]Departnment of Engineering, University of Hyogo,[2] Institute for Molecular Science,[3] The Institute for Solid State Physics, The University of Tokyo,[4] National Institute for Materials Science

Introduction

Reducing CO_2 emission, capturing, storage and utilizing of CO_2 as a feedstock to synthesize useful chemicals not only contribute to solve “greenhouse effect” but also to provide a great challenge in exploring new methods and opportunities for catalytic and industrial development. Although various technologies for CO_2 reduction has been considered, the recycling of CO_2 by hydrogenation to high-energy-density liquid fuel is considered to be the most attractive approach in terms of economy, ecology, and safety. In order to further improve the activity, selectivity and stability of catalyst, the origins of catalytic properties, transition metal Pd is an excellent candidate to activate hydrogen molecules, leading to a catalyst surface with highly reduced state, which can facilitate the hydrogenation process. Alloy sites have been considered as the active sites in the CO_2 hydrogenation, such as Pd-based bimetallic catalysts [1-4]. The study of bimetallic surfaces has gained considerable interest because it is difficult to know the correlations between electronic and chemical properties of the intermixed bimetallic surfaces and the catalytic reaction. In this study, the ambient pressure X-ray photoelectron spectroscopy were carried out to investigate the changes of electronic properties as well as the reaction mechanisms during the CO_2 hydrogenation over Pd-based alloy catalysts.

Experimental

The fcc- and B2- phased $PdCu_{40}$ and $PdAg_{23}$ alloys (ϕ12.4 mm, 0.1 mm thickness) were obtained from Tanaka Kikinzoku Kogyo K.K.. The bulk compositions were 60 wt% Pd and 40 wt% Cu for PdCu alloy, and 77 wt% Pd and 23 wt% Ag for PdAg alloy. The clean surface of PdCu and PdAg alloys are prepared by several cycles of Ar^+ sputtering (0.5 keV) for 15 min and annealing at 670-675 K for 2 min. The CO_2 hydrogenation were observed under H_2 and CO_2 atmosphere by using ambient pressure X-ray photoelectron spectroscopy system with base pressure of $\sim 5.0 \times 10^{-10}$ Torr at BL07LSU, SPring-8. The temperature dependence experiments were performed under H_2 pressure of 0.4 mbar and CO_2 pressure of 1.6 mbar at 300 K, 310 K and 320 K. The gas pressure dependence was performed under H_2 pressure of 0.4 mbar and CO_2 pressure of 0.8, 1.6 and 2.4 mbar at 300 K. The C 1s, O 1s, Pd 3d and Ag 3d core-level were measured at photon energy of 680 eV, and Cu 2p spectra were measured at photon energy of 1200 eV.

Results and Discussion

C 1s spectra measured on the clean surface and under H_2 pressure of 0.4 mbar and CO_2 pressure of 1.6 mbar at 300 K on the PdCu(fcc) alloy are shown in Fig.1. The graphene-like carbon C-C(sp^2) located at binding energy (BE) of 284.4 eV and CO contaminations whose BE is 286.2 eV still remained on the clean surface even after several cycles of Ar^+ sputtering and annealing. The component located at BE of 287.5 eV appeared after flowing H_2 and CO_2, which can be assigned as the intermediate species formate ($H_2 + 2CO_2 \rightarrow 2HCOO$) during the CO_2 hydrogenation. The amount of formate slightly increased with exposure time. Figure 2 shows the C 1s spectra observed on the clean surface and during CO_2 hydrogenation process under the H_2 pressure of 0.4 mbar and CO_2 pressure of 1.6 mbar at 300 K on the PdCu(B2) surface. It shows the same reaction behavior on the B2-phased PdCu surfaces as that on fcc-phased PdCu surfaces, where the formate slightly increased with exposure time. The amount of formate formed on the surface after exposure time of 82 min are almost same between fcc phase and B2 phase. It indicates that the activity of CO_2 hydrogenation is relatively high to other catalyst, such as ZnCu alloy. The phase-structure has little effect on CO_2 hydrogenation activity on the PdCu alloys. Figure 3 shows the C 1s spectra measured on the clean surface and under H_2 atmosphere of 0.4 mbar and CO_2 atmosphere of 1.6 mbar at 300 K on the PdAg alloy. After H_2 and CO_2 exposure, the formate was formed on the surface, and increased with time. Besides, the additional adsorption species C=O species, CH_x and C-C(sp^3) appeared on the surface, whose BEs are 287.2 eV, 285.0 eV and 284.2 eV, respectively. We observed that CO formation is largely suppressed, however, formate formation activity is almost same on the PdAg alloy compared to the reaction on the PdCu alloys. The temperature dependence of the formate formation on PdCu(fcc) alloy is shown in Fig.4. The formate formation rate is higher at lower temperature, which indicates the desorption of formate is occurring during the CO_2 hydrogenation by increasing the temperature.

REFERENCES

[1] X. Jang et al. Catalysis Communications 118 (2019) 10.
[2] X. Nie et al. ACS Catal. 2018, 8, 4873.
[3] S. Bai et al. J. Am. Chem. Soc. 2017, 139, 20.
[4] K. Mori et al. J. Am. Chem. Soc. 2018, 140, 8902.

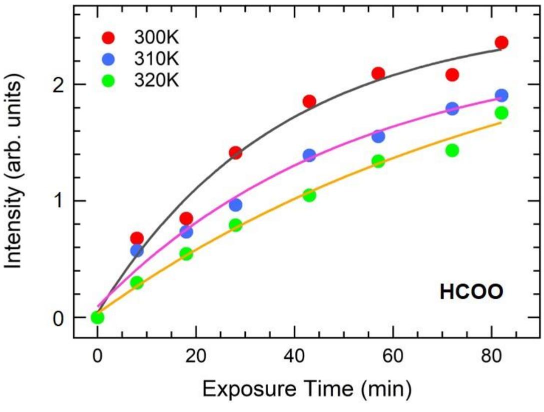

Fig.4 Temperature dependence of the formation of HCOO with exposure time on the PdCu(fcc) alloy.

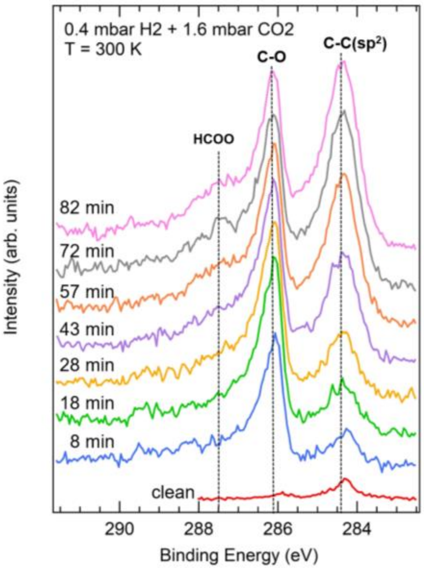

Fig.1 C 1s spectra measured on the clean surface and after H_2 exposure at 0.4 mbar and CO_2 at 1.6 mbar at 300 K on PdCu(fcc) alloy.

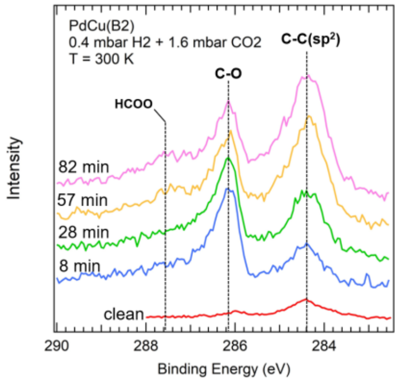

Fig.2 C 1s spectra mesured on the clean surface and under H_2 exposure at 0.4 mbar and CO_2 at 1.6 mbar at 300 K on PdCu(B2) alloy.

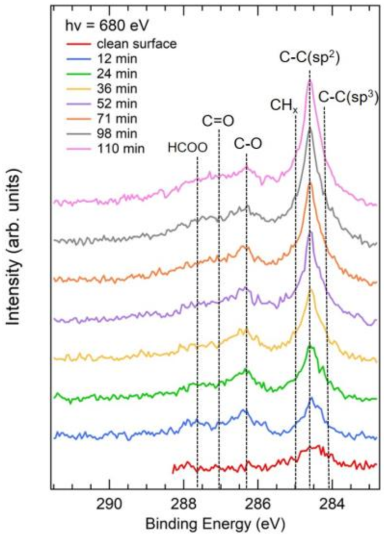

Fig.3 C 1s spectra measured on the clean surface and under H_2 exposure at 0.4 mbar and CO_2 at 1.6 mbar at 300 K on PdAg alloy.

SOFT X-RAY SPECTROSCOPY OF SOLUTIONS WITH CARBON NANOTUBES TREATED VIA PLASMA IN LIQUID

Kazuo Terashima[1,2], Noritaka Skakibara[1,2], Kenichi Inoue[1], Shion Takahashi[1], Taku Goto[1,2], Tsuyohito Ito[1], Keishi Akada[2,3], Jun Miyawaki[1,3], Yukiya Hakuta[2], Yoshihisa Harada[1,2,3]

[1]*Department of Advanced Materials Science, Graduate School of Frontier Sciences, The University of Tokyo*

[2]*AIST-UTokyo Advanced Operando-Measurement Technology Open Innovation Laboratory (OPERANDO-OIL), National Institute of Advanced Industrial Science and Technology (AIST)*

[3]*Synchrotron Radiation Laboratory, The Institute for Solid State Physics, The University of Tokyo*

Flexible and wearable electronic devices have attracted much attentions. Substrates for such devices are often required to have both flexibility and functional properties. Composite materials, which consists of inorganic fine particles providing functionalities and polymer materials providing flexibility, are promising candidates for the substrate. However, in general, the flexibility is greatly reduced as the mixing ratio of inorganic fine particles increases to reach desired functionalities.

To overcome such trade-off, we treated inorganic fine particles by plasma in solution. The resulted composite materials, such as plasma-treated BN particles with slide-ring materials, showed improved toughness and high thermal conductivity comparing with the composite with non-treated BN particles [1]. One of the reasons for the good performance might be high dispersibility of inorganic particles in the composites [2]. The high dispersibility should be achieved with well-dispersed suspension during the process.

Carbon nanotubes are well known to have high thermal and electrical conductivities and thus applied for high thermal and electrical conductive composites. It is also known that plasma treatment in solution could improve dispersibility in solution, thus might results in better performances in the composites made e.g. with solution. In this study, by soft X-ray emission spectroscopy (XES) we are analysing the solutions with carbon nanotubes treated by plasma in liquid to reveal how the plasma treatment could improve the dispersibility.

Soft X-ray emission spectroscopy (XES) of the solutions were performed at SPring-8 synchrotron radiation facility using the BL07LSU HORNET station. In the station, the original system for performing XES of liquid with a very thin (150 nm) Si_3N_4 window is equipped. Thus we have applied this spectroscopic system for investigating our solution with CNTs. The probe was O 1s, which should represent the structure of H_2O molecules in the CNT-dispersed solution. The first purpose of this study is to detect changes of water structure associated with CNTs.

The soft X-ray emission spectrum of the hydrophilized CNTs aqueous solution was compared with the untreated CNTs dispersion. The hydrophilization was performed with plasma in solution containing 4 wt% hydroquinone and 0.5 wt% multi-walled CNTs (average diameter and length were 20-30 nm and 0.5-2 μm) in 70 ml deionized water (Fig. 1). The treatment time was 30 min.

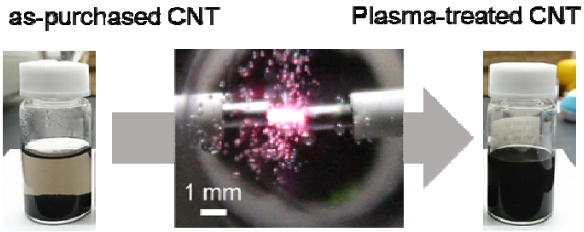

Fig. 1 Schematic of plasma treatment of CNTs in solution.

After the treatment, the remaining hydroquinone were rinsed away with ethanol and dried CNTs were re-dispersed in deionized water to form the solution investigated.

The XES spectra of pure water, solutions with plasma-treated CNTs, and solutions with raw CNTs were recorded and compared. CNT concentrations were modified from 0.1 to 1 w% for plasma-treated one. Since the untreated CNTs could not be dispersed in water well, the concentration of raw CNTs were essentially unknown although we modified the initial concentration at 0.5 w% .

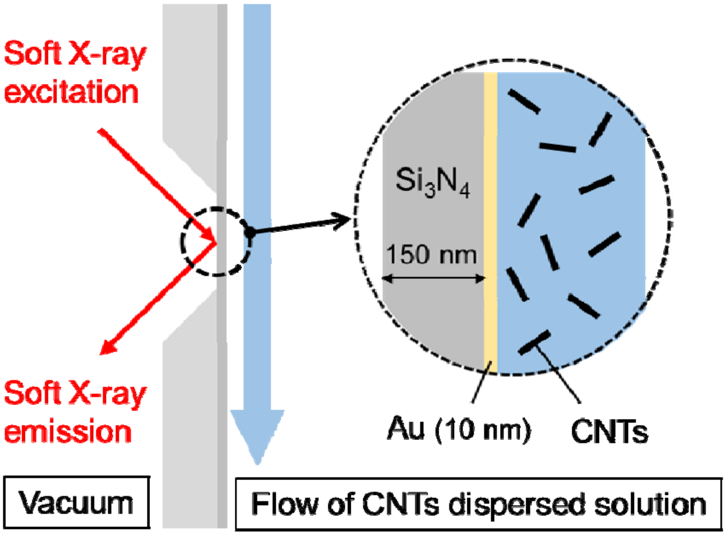

Fig. 2 Schematic diagram of XES applied in this study.

The spectra of pure water and the solution with raw CNTs were almost identical, while the spectra with plasma-treated CNTs with concentration higher than 0.5 w% clearly showed different feature around $3a_1$ region at 521–525 eV, indicating the modification of hydrogen bonding network by plasma-treated CNTs. While the mechanism for the spectral change still need to be revealed with theoretical study, the difference could be seen only with high concentration of CNTs, which could not be achieved with untreated CNTs.

REFERENCES

[1] T. Goto, M. Iida, H. Tan, C. Liu, K. Mayumi, R. Maeda, K. Kitahara, K. Hatakeyama, T. Ito, Y. Shimizu, H. Yokoyama, K. Kimura, K. Ito, Y. Hakuta, K. Terashima, *Appl. Phys. Lett.* **112**, 101901 (2018).

[2] T. Goto, M. Iida, H. Tan, C. Liu, K. Mayumi, R. Maeda, K. Kitahara, K. Hatakeyama, T. Ito, Y. Shimizu, H. Yokoyama, K. Kimura, K. Ito, Y. Hakuta, K. Terashima, *J. Japan Inst. Met. Mater.* **82**, 403-407 (2018). [in Japanese]

Photoelectron spectral imaging of p^+-WSe$_2$/n-MoS$_2$ hetero junctions for TFET device structures

Naoka Nagamura[1,2], Keigo Nakamura[3], Keishi Akada[4], and Kosuke Nagashio[3]

[1]*National Institute for Materials Science (NIMS), Tsukuba, Ibaraki, Japan.*
[2]*PRESTO, Japan Science and Technology Agency, Honcho, Saitama, Japan.*
[3]*Department of Materials Engineering, The University of Tokyo, Hongo, Tokyo, Japan.*
[4]*Institute for Solid State Physics, The University of Tokyo, Kashiwa, Chiba, Japan.*

The significant increase of data traffic causes the increase of energy consumption, so power saving of electronic devices is an urgent issue. Recently, two-dimensional tunnel field effect transistors (2D TFETs) have drawn attention as the low power switching FETs which can realize the low subthreshold swing compared to conventional MOSFETs. TFET devices need the p^+/n heterojunction with large band-discontinuity. Here we have found that p^+-WSe$_2$ doped chemically by WO$_x$ can be stabilized in air by transferring it on *h*-BN, then we succeeded in observing TFET characteristics in the p^+-WSe$_2$/MoS$_2$(4 ML) heterostructure [1].

In a usual *p/n* heterojunction of semiconductors, a depletion layer is generated and continuous band bending of micro-meter order occurs at the interface. However, our photoluminescence spectroscopy measurements suggest that the charge transfer at the p^+-WSe$_2$/MoS$_2$ heterojunction forms valence band offset of the MoS$_2$ sheet and band-discontinuity at the interface.

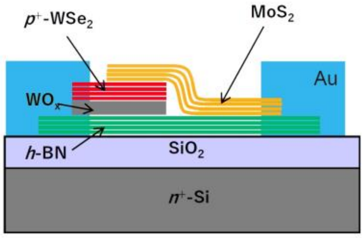

Fig. 1 Schematic image of a p^+-WSe$_2$/MoS$_2$ TFET device structure

In this study, we have attempt to characterise the local charge transfer at interfaces in the p^+-WSe$_2$/MoS$_2$ TFET device structure as shown in Fig. 1 by scanning photoelectron emission microscopic (SPEM) measurements using a three-dimensional nanoscale electron-spectroscopy chemical analysis (3D nano-ESCA) system installed at BL07LSU of SPring-8.

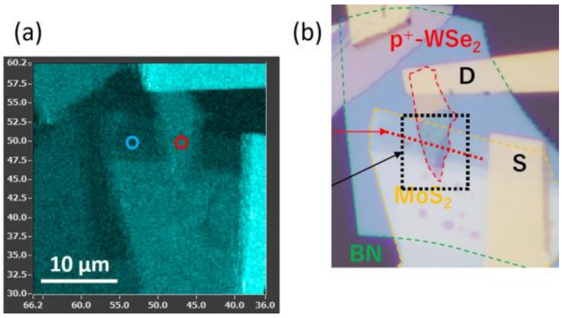

Fig. 2 (a) O 1*s* core level photoelectron intensity mapping of the device structure. (b) Optical image of the device structure.

2D materials used in the sample are fabricated by exfoliation of bulk crystals. WO$_x$ side of WSe$_2$ film is transferred onto *h*-BN on a SiO$_2$/n^+-Si substrate after forming WSe$_2$/WO$_x$ by O$_3$ annealing. In this process, p^+-WSe$_2$ is stabilized. Then, MoS$_2$ with suitable thickness (1-5 ML) is chosen by its optical contrast and the p^+-WSe$_2$/MoS$_2$ heterostructures were fabricated via dry transfer method using PDMS under the alignment system. Ni/Au was deposited as source/drain electrodes by EB lithography.

Fig. 2 shows a photoelectron intensity mapping of the p^+-WSe$_2$/MoS$_2$ TFET sample. Comparing to the optical image, the device structure can be clary identified. Mo 3*d* and S 2*s* core level photoelectron spectra were measured locally at two different regions; MoS$_2$ on *h*-BN and MoS$_2$ on p^+-WSe$_2$. Peak shift which is caused by charge transfer between MoS$_2$ and p^+-WSe$_2$ was not detected as shown in Fig. 3.

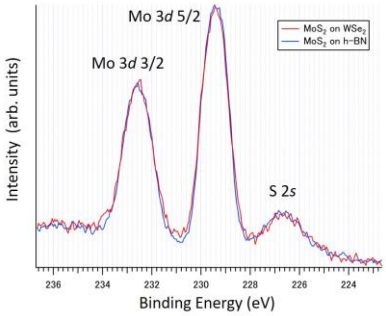

Fig. 3 (a) Mo 3*d* and S 2s core level spectra of pin-point analysis. Measurement points are presented in Fig. 2(a) as circles.

Background signal owing to the 0th order diffracted beam of the focusing optics, the Fresnel zone plate, prevent to detect such a small peak shift. So, we have induced a new focusing optical stage with a center beam stop and dual Fresnel zone plates for wide-energy-range experiments. The significant improvement in special resolution and signal-to-noise ratio will be expected in the measurement in 2019.

We are also working on the feasible study of the practical use of machine learning technique for the data analysis of spectral imaging obtained by 3D nano-ESCA. To reduce computational cost for high-throughput analysis in multi-parameter measurements in 3D nano-ESCA, compared with previous studies using a Bayesian peak separation with the exchange Monte Carlo method [2], we used an expectation-maximization (EM) algorithm and confirmed drastic acceleration of peak fitting in comparison to the manual approach [3]. Now we aim for applying this method to on-site data analysis during experiments.

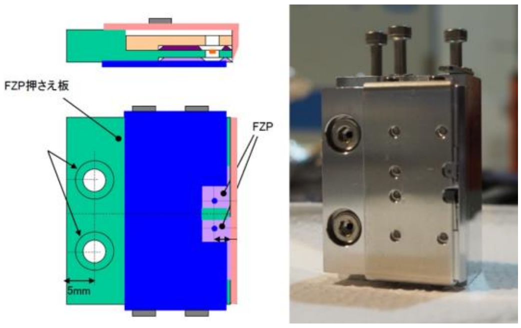

Fig. 4 Schematic image (left) and photo (right) of the new optical stage including Fresnel zone plates.

REFERENCES

[1] J. He *et al*. Adv. Electron. Mater. 4, 1800207 (2018).
[2] K. Nagata *et al*., Neural Networks 3, 82 (2012).
[3] T. Matsumura *et al*. Sci. Technol. Adv. Mater. (2019) in press.
(DOI: 10.1080/14686996.2019.1620123)

TIME-RESOLVED PHOTOELECTRON HOLOGRAPHY STUDY OF SILICENE

Kouichi Hayashi[1,2], Artoni Kevin R. Ang[1], Koji Kimura[1], Yuichiro Fukatsu[1], Akito Asano[1],
Takahiro Tsukada[1], Yohei Okuda[3], Takahiro Yonezawa[4], Antoine Fleurence[4], Yukiko
Yamada-Takamura[4]
[1]Structural Physics Laboratory, Nagoya Institute of Technology, Nagoya, Japan
[2]Frontier Research Institute for Materials Science, Nagoya Institute of Technology, Nagoya, Japan
[3]Okayama University, Okayama, Japan
[4]School of Materials Science, Japan Advanced Institute of Science and Technology, Ishikawa, Japan

[Introduction]

Silicene is a monolayer of Si atoms arranged in a honeycomb lattice that exhibits massless Dirac fermions, similar to its carbon based counterpart in graphene. The development of silicene based devices have seen significant interest recently because of the expected remarkable electronic properties, stronger spin-orbit coupling of Si, and the ease of adapting such technologies into the already Si-based manufacturing infrastructure. Until recently, silicene could only be synthesized on conductive substrates, resulting in electronic interactions with the substrate. It was recently demonstrated that silicene with minimal substrate interactions can be grown on a ZrB_2/Si(111) substrate through the surface segregation of Si atoms[1]. This silicene layer was found to buckle easily, resulting in sp^2/sp^3 hybridization that can tailored to tune its electronic properties [1,2]. Photoemission studies have shown that the Si atoms occupy at least 3 chemically different sites on the silicene layer (Fig. 1a) [1,3]. In this study, we investigate the different local structures around these Si atoms using photoelectron holography (PEH). Furthermore, dynamic investigations will be done using time-resolved PEH.

[Experiment]

To do this, the silicene samples were grown in-situ in the angle-resolved time-of-flight (ARTOF) end station of BL-07. A ZrB_2/Si(111) substrate was prepared elsewhere and was degassed after introduction into the UHV chamber. This was followed by annealing at 800°C, where the silicene layer forms spontaneously through the segregation of the Si atoms from the substrate [1]. The silicene surface was evaluated using LEED and core level photoemission.

For the photoemission experiments, the photon energy used was $h\nu = 300$ eV. The angular distribution and the energy of the photoelectrons were recorded using the ARTOF detector. In this experiment, the acceptance angle was ±13°. To obtain a larger section of the hologram pattern, the sample's orientation with respect to the detector was varied.

In the time-resolved experiments, a 1.5 eV, 208 kHz laser was used as the pump and 300 eV X-rays from the synchrotron was used as the probe.

[Results]

The LEED and Si 2p spectra confirmed the formation a well-defined silicene layer. The Si 2p spectra (Fig. 1b), show two peak components resolved by peak fitting, similar to 2 of the 3 reported peak fitting components [1,3]. In our preliminary PEH experiments in a high resolution hemispherical analyser in KEK-PF, the same sample preparation was used and resulted in well resolved components in the Si 2p spectra, identical to those reported [1,3].

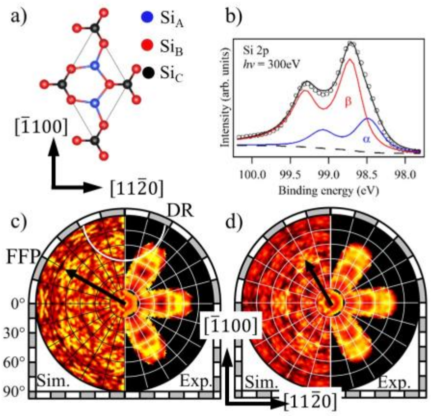

Fig. 1 a) Structural model of epitaxial silicene, b) Si 2p peak fitting components, and simulated and experimental holograms from the c) Si_A and d) Si_B peak components.

These peak components, α and β, correspond to the Si atoms in the A and B positions, as noted in Fig. 1a. Using the difference in the peak positions of these components, the hologram patterns for each component was extracted by pixel-by-pixel peak fitting of the 3D data I(k_x, k_y, E). Figure 1c and 1d shows the simulated and experimental holograms from the $\mathrm{Si_A}$ and $\mathrm{Si_B}$ atoms. The prominent features of these patterns are the diffraction rings (formed by scatterers located in-plane) and the forward focusing peaks (FFP) (formed by scaterrers located out-of-plane, which in this case is the $\mathrm{Si_C}$ atom). In particular, the FFP from the $\mathrm{Si_B}$ atom (θ ≈ 48°) is well reproduced.

For the dynamic measurements, the time-resolved XPS spectra in Fig. 2a) show a small shifts (~10 meV) in the peak position after irradiation with the pump laser. The FFPs (Fig. 2b) from the time-resolved $\mathrm{Si_B}$ hologram patterns (Fig. 2c - 2f) also show small shifts towards higher polar angle positions, this indicates that there is a small decrease in the height of the $\mathrm{Si_C}$ atom from the $\mathrm{Si_A}$-$\mathrm{Si_B}$ plane.

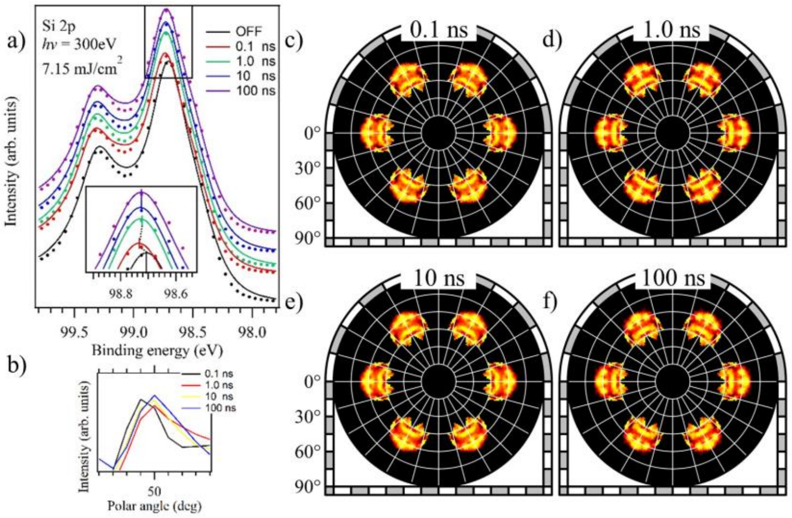

Fig. 2 a) Time-resolved Si 2p spectra, b) polar line profiles along the FFP from the time-resolved PEH patterns, and the SiB time-resolved holograms at delay times of: c) 0.1 ns, d) 1.0 ns,
e) 10 ns and f) 100ns.

The time-resolved Si 2p spectra indicate that there are no significant changes in the chemical environment of the Si atoms in the silicene layer, while the FFPs suggest small shifts in the height of the $\mathrm{Si_C}$ atom. These structural changes could be due to localized heating from the laser, causing expansion of the layer. High-temperature STM work done in JAIST shows modulation of $\mathrm{Si_C}$ atom height, which seems to agree with the changes in the FFPs.

However, in the time-scales investigated here, the system was not observed to relax back to equilibrium, and further experiments with longer time scales are necessary (~ms scale). Furthermore, a detailed understanding of the structural changes occurring upon laser irradiation is still needed.

[Results]

In this study, site-selective photoelectron holography was performed on silicene. The FFPs from the simulation are well reproduced in the experiment. Time-resolved photoemission experiments show small shifts in the $\mathrm{Si_C}$ position, possibly as a result of localized heating by the laser. Additional experiments with longer time-scales will be performed to fully understand what happens to the buckled Silicene layer upon heating. Such information will be vital for future silicene based devices.

REFERENCES

[1] A. Fleurence, et al., Phys. Rev. Lett. **108**, 245501 (2012).
[2] R. Friedlein and Y. Yamada-Takamura. J. Phys. Condens. Matter **27**, 203201 (2015).
[3] R. Friedlein, et al., J. Chem. Phys. **140**, 184704 (2014).

SOFT X-RAY INELASTIC SCATTERING AND DIFFRACTION TECHNIQUES APPLIED FOR THE STUDY ON THE ROLE OF WATER AND HYDRATION IN BIOPOLYMERS, POLYSACCHARIDES AND ELECTROLYTES

Jun Miyawaki, Kosuke Yamazoe, Yitao Cui and Yoshihisa Harada*
Synchrotron Radiation Laboratory, The Institute for Solid State Physics, The University of Tokyo

With the rapid increase in its energy resolving power, RIXS has become one of the cutting-edge tools to investigate the electronic structure of materials. We have developed our RIXS station to accept various sample circumstances and seamless spectrometer rotation for momentum dependence experiments. The aim of this project is to provide abundant potential use of RIXS/XES and its combination with soft X-ray diffraction. Here we show three types of outcomes obtained in this project in 2018.

1) Folding induced dehydration observed in PNIPAM

We have probed the electronic structure of poly(N-isopropylacrylamide) solution (PNIPAM, inset in Fig. 1), a stimuli-sensitive polymer that undergoes clouding (around 33.7 ℃) upon heating and is regarded as a simple model of proteins, using soft X-ray absorption/emission spectroscopy. Figure 1(a) shows the temperature dependence of the O *K*-edge X-ray absorption spectra of PNIPAM aqueous solution. The peak around 532 eV is assigned as C=O double bond but has at least two components, a 531.5 eV peak favoured at 30 ℃ and a 532.4 eV peak favoured at 36 ℃. Figs. 1 (b) and (c) show O *K*-edge RIXS spectra at the 531.5 eV and 532.4 eV resonances. In addition to two peaks from the C=O σ and π components, one more peak appears at the 532.4 eV resonance. The new peak would be related to the formation of hydrogen bonds between water molecules and PNIPAMs, thus reflecting the dehydration process through the precise temperature dependent RIXS.

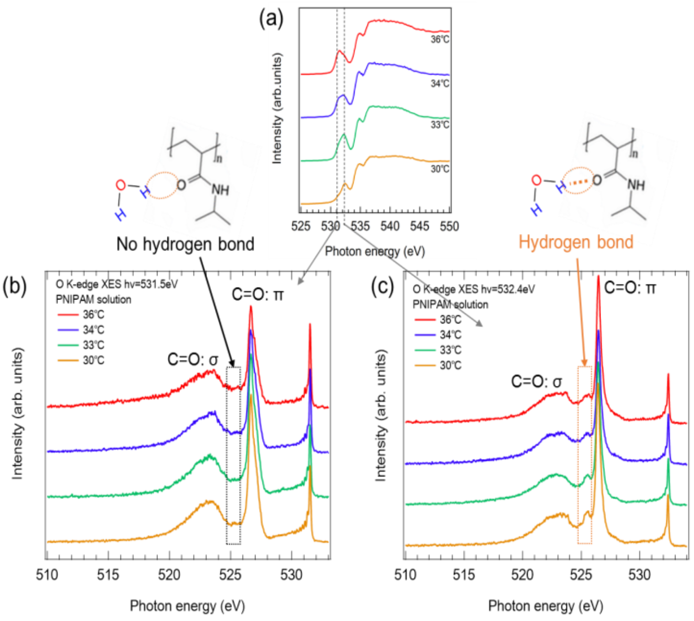

Figure 1. (a) Temperature dependence of soft X-ray absorption spectrum of PNIPAM aqueous solution. (b)(c) Temperature dependence of the resonant soft x-ray emission spectrum, respectively. The hydrogen bond between water and PNIPAM is shown above panel (c).

2) Li-H_2O interaction observed in hydrate melt electrolytes

The structure of a lithium salt hydrate melt (LSHM) was investigated by O K-edge X-ray absorption and RIXS spectroscopy. Hydrate melt is a metal salt that forms liquid by addition of only a small amount of water. How exactly H_2O bonds with other anions/cations to form a liquid and how Li behaves in the hydrate melt are still open questions. Figure 2 shows O *K*-edge RIXS spectrum of liquid LSHM with the chemical formula $Li(TFSI)_{0.7}(BETI)_{0.3}\cdot 2H_2O$ which has high performance as an aqueous electrolyte for Li-ion batteries. In order to extract actual local structural information of water in the LSHM from the experimental RIXS spectra, density-functional theory based molecular dynamics simulations were carried out and the RIXS spectra were calculated for the ensemble of clusters extracted from the molecular dynamics simulations coupled with non-resonant semiclassical Kramers-Heisenberg formalism. Elementary structures were identified through the comparison between the experimental and theoretical spectra, which clearly distinguished interactions between Li-H_2O, Li-anion, and H_2O-anion present in the hydrate melt. It is found that Li is not necessarily moving jointly with other water molecules in the hydrate melt but is rather breaking old and forming new Li-O bonds as it is progressing through the hydrate melt.

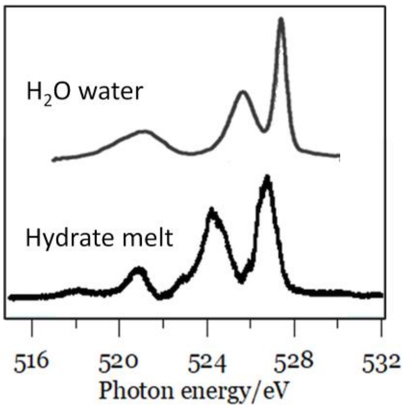

Figure 2. O *K*-edge RIXS spectra of pure H_2O water and hydrate melt $Li(TFSI)_{0.7}(BETI)_{0.3}\cdot 2H_2O$.

3) Resonant Inelastic Soft X-ray Diffraction of $La_{1/3}Sr_{2/3}FeO_3$

Scattered X-ray is separated into elastic and inelastic scattering according to the amount of energy loss. The momentum dependence of elastic scattering, which has no energy loss, gives information about structural order by X-ray diffraction, and that of inelastic scattering, which has energy loss, gives the energy-momentum dispersion of elementary excitations, such as orbiton, magnon, and phonon. Here, at a particular momentum $\boldsymbol{q}$ which satisfies the Bragg condition and where X-ray diffraction peak (enhanced intensity of elastic scattering) is observed, the intensity of the inelastic scattering is expected to be enhanced assisted by the X-ray diffraction: "Inelastic X-ray diffraction" is expected to be observed. Thus, in order to demonstrate "inelastic X-ray diffraction", we have investigated the $\boldsymbol{q}$ dependence of the intensity of the inelastic scattering of $La_{1/3}Sr_{2/3}FeO_3$ around its magnetic diffraction.

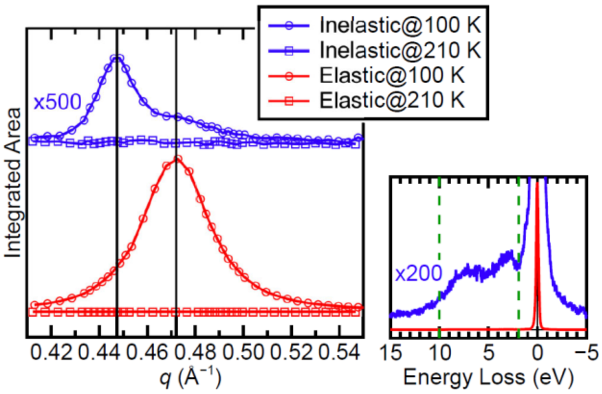

Figure 3. Resonant elastic X-ray scattering (red) and resonant inelastic X-ray diffraction (blue) scans measured at Fe *L*-edge RIXS. The integration range for the inelastic scattering is indicated by two green lines in the right figure.

Figure 3 shows the results of resonant inelastic soft X-ray diffraction of $La_{1/3}Sr_{2/3}FeO_3$ measured at 100 K (magnetically ordered) and 210 K (no magnetic order). A peak at $q \approx 0.472$ Å^{-1} of elastic scattering at 100 K is ascribed to the magnetic diffraction. However, an extra peak was observed at $q \approx 0.447$ Å^{-1} for inelastic scattering. At 210 K, the peak at $q \approx 0.447$ Å^{-1} disappeared accompanied by the disappearance of magnetic diffraction peak. These results strongly suggest that the observed extra peak at $q \approx 0.447$ Å^{-1} is the enhancement of the inelastic scattering assisted by X-ray diffraction, and thus inelastic X-ray diffraction was successfully demonstrated.

OPERANDO OBSERVATION OF BURIED INTERFACES OF DEVICES BY USING SOFT X-RAY PHOTOELECTRON MICROSCOPY IN COMBINATION WITH CHARGE NEUTRAL CONDITION

Hirokazu Fukidome, Naoka Nagamura[2], Masaharu Oshima[3]
[1]*Research Institute of Electrical Communication, Tohoku University*

[2]*NIMS*

[3]*ISSP, The University of Tokyo*

The scanning-type soft x-ray photoelectron spectromicroscopy, so-called, 3D nano-ESCA is the powerful tool in elucidating chemical and electronic natures of surfaces with the high-spatial resolution. To be noted, we have newly developed created operando observation system, i.e. the system that enables to observe surface electronic and chemical states of devices in operation. In 2018-2019, we have published the articles about device observation using 3D nano-ESCA, for Graphene FETs [1, 2] and GaN-HEMT [3] by using 3D nano-ESCA.

These works have been high evaluated in terms of both basic research to elucidate materials functioning and applied device researches. As a consequence, in addition to paper publications, we have applied for more than 10 patents, as registered in SPring-8 research record, with companies (Sumitomo Electric Industreies, and ShinEtsu Chemicals) which has collaborated with us about device operation mechanistic study with the aid of 3D nano-ESCA, in the industry-government-academia collaboration projects in recent years, such as SCOPE of Ministry of internal affairs and communication, NEDO of Ministry of Economy, Trade and Industry, and Grant-in-Aid for Specially Promoted Research of MEXT.

However, soft x-ray photoelectron nanospectroscopy has the limitation that it is hard to probe buried interfaces because of electron escape depth of several nanometers. We should surmount this limitation for devices or functionalized materials that has complicated structures to deliver maximal performances.

In this study, we tackle to solve the above-mentioned issue by using the charge-neutrality condition, in combination with precise advanced device technologies.

The charge-neutrality condition is the key in this study for solving the issue. By using this condition with the aid of the advanced device technologies, the soft x-ray photoelectron nanospectroscopy can probe electronic states of both buried interfaces and surfaces (Figure 1).

The model for this is GaN-HEMT [3]. The operation of GaN-HEMT is degraded by the so-called current collapse phenomena. The main cause of the current collapse phenomena is electron trapping at surface traps. In the direction perpendicular to the surface, the charge neutrality condition holds, i.e. the sum of charges is zero at every point. Then, if there are negligible density of charges except surface trapped electron and carrier density in the channel, the carrier density in the channel, which is the key factor in device performances, is determined by measuring surface trapped electron density by using

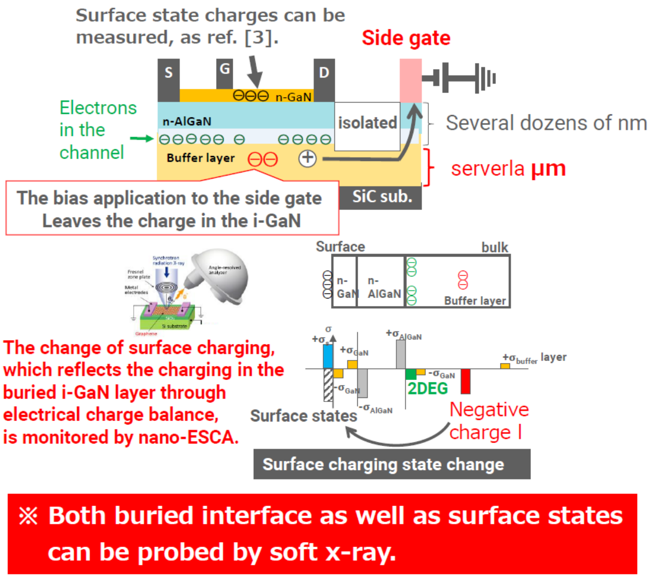

Figure 1 Schematics of this study

operando photoelectron nano spectroscopy with 3D nano-ESCA [3].

However, in real devices, the charge trapping except at the surface and in the channel cannot be ignored. For instance, the buffer layer between GaN and SiC substrates for GaN-HEMT contains trapped electrons. This causes so-called virtual back-gate effects which leads to long-term instabilities of GaN-HEMT. Coversely, controlling enough the buried interface electrically enables us to probe the electronic states of buried interface by using soft x-ray photoelectron spectroscopy.

In the experiments in 2019 B, we have tried to establish the method to probe buried interfaces by using soft x-ray. For that purpose, we used GaN-HEMT with an additional side gate as a model sample, in collaboration with Sumitomo Electric Industries. A typical result is shown in Figure 2.

The application of the side-gate bias withdraws mobile (trapped charges) in the buffer layer and leaves opposite charges of trapping sites. As shown in the previous report [3], the blue-shift of the spectral centroid of the surface GaN indicates the electron trapping at the surface. However, as shown in Fig. 1, we predicted that the surface trapped electron decrease by leaving negative charges (trapping sites) with withdrawing mobile holes due to the side-gate application. We speculates the cause to the temporal change of surface condition irrelevant to the side-gate bias application that overwhelms the shift due to the side-gate bias application. Unfortunately, however, we cannot have enough evidence to support our speculation.

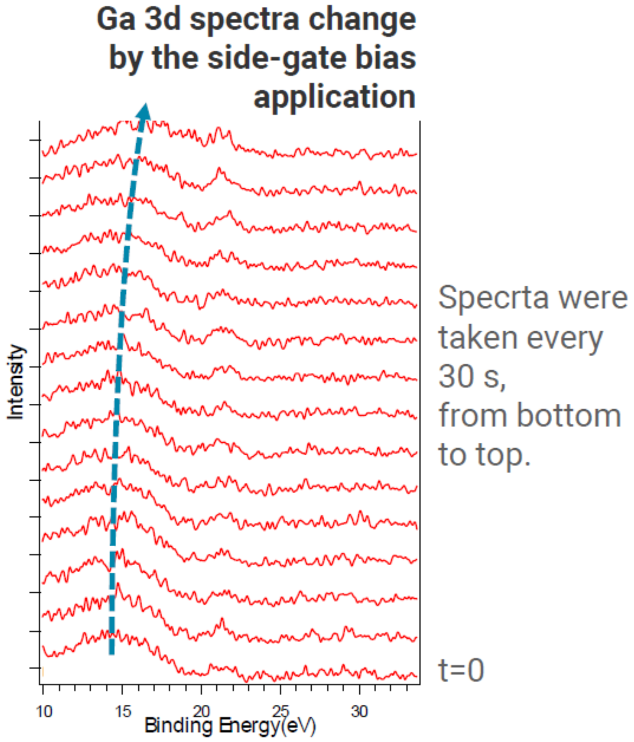

Figure 2 A typical result of this study.

REFERENCES

[1] N. Nagamura, H. Fukidome, K. Nagashio, K. Horiba, T. Ide, K. Funakubo, K. Tashima, A. Toriumi, M. Suemitsu, and M. Oshima, Influence of interface dipole layers on the performance of graphene field effect transistors, Carbon, 152 (2019) 680-687. Impact factor：7.466

[2] H. Fukidome, K. Funakubo, N. Nagamura, K. Horiba, Y. Tateno, M. Oshima, and M. Suemitsu, Modulation of Electronic States near Electrodes in Graphene Transistors Observed by Operando Photoelectron Nanospectroscopy, Sensors and Materials, (2019), accepted.

[3] K. Omika, Y. Tateno, T. Kouchi, T. Komatani, S. Yaegassi, K. Yui, K. Nakata, N. Nagamura, M. Kotsugi, K. Horiba, M. Oshima, M. Suemitsu, and H. Fukidome, Operation Mechanism of GaN-based Transistors Elucidated by Element-Specific X-ray Nanospectroscopy, Scientific Reports, 8 (2018) 13268.

REVEALING THE MECHANISM OF THE METAL-INSULATOR TRANSITION IN VO_2 PROBED BY MOMENTUM RESOLVED RIXS

H. Fujiwara[1], T. Kashiuchi[1], K. Nishimoto[1], N. Nishikawa[1], A. Irizawa[2],
J. Miyawaki[3,4], and Y. Harada[3,4]

[1]Graduate School of Engineering Science, Osaka University, Toyonaka, Osaka 560-8531, Japan
[2]Institute of Scientific & Industrial Research, Osaka University, Ibaraki, Osaka 567-0047, Japan
[3] Institute for Solid State Physics (ISSP), The University of Tokyo, Japan
[4] Synchrotron Radiation Research Organization, The University of Tokyo, Japan

Introduction

VO_2 is a text book compound which shows the first-order metal-insulator transition (MIT) at 340 K [1]. Since the transition temperature is controlled by applying the voltage, this material is a good candidate for the application of a resistive memory in the new field of the oxide electronics [2]. Since the crystal structure changes across the transition accompanied by forming the V dimer along the c-axis in the insulating phase, Peierls transition is one of the possibilities to explain the MIT. On the other hand, the Mott transition due to the strong electron correlation in the V 3*d* states has also been discussed. Moreover, the recent study using the photoemission and X-ray absorption spectroscopy pointed out the orbital-assisted MIT scenario, in which the electron correlation is enhanced by forming the one-dimensional chain due to the *c*-axis dimer [3,4]. Therefore, the mechanism of the MIT has been under debate. To reveal the mechanism of the MIT in VO_2, we have performed the resonant inelastic soft-x-ray scattering at V 2*p* edge to probe the excitation from the occupied to the unoccupied 3*d* states (*dd*-excitation) by changing the scattering angle parallel to the *c* axis.

Experimental

RIXS measurements were performed at the SPring-8 BL07LSU HORNET end-station, where a high-resolution soft x-ray spectrometer are installed [5]. Total energy resolution was set to about 150 meV at V 2*p* edge, and the experimental temperature was set to 300 K and 390 K to study the *dd*-exciation in the insulating and insulating phases, respectively. Moreover, the momentum resolved measurements were performed at 300 K. The single crystalline VO_2 was fractured in situ to expose the clean (001) surface. For the momentum resolved measurements, the geometry of the spectrometer is set to keep the scattering vector parallel to the (001) direction.

Results and discussions

Figure 1 shows V 2*p* XAS spectra obtained by the horizontally and vertically polarized photons with electric field vector *E* parallel and perpendicular to the crystal *c* axis at 300 K in the insulating phase. The spectra show the clear linear polarization dependence, which is consistent with previous report [3]. This dichroism suggests the anisotropic charge distribution of the V 3*d* states due to the dimer formation of the V ions along the

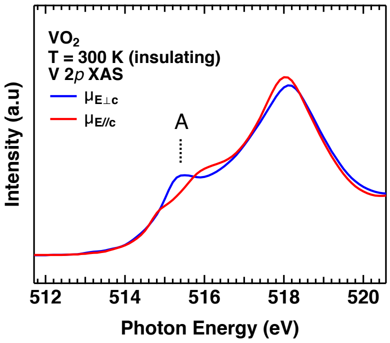

Figure 1
V 2p XAS spectra of VO_2 recorded with $E//c$ and $E \perp c$ configurations.

crystal *c*-axis. Especially the shoulder structure at incoming photon energy ($h\nu_{in}$) of 515.4 eV (A) clearly shows the linear dichroism, suggesting that the *dd*-excitations in the RIXS spectra obtained at A reflect the electronic structure along the V dimer, since the intermediate states in the optical process of RIXS is same as XAS.

Figure 2 shows V 2*p* RIXS at $h\nu_{in}$ = 515.4 eV obtained with a scattering angle 2θ of 90° and 120°. The *dd*-excitations around 0.5 eV in the energy loss scale are observed in both 90° and 120° spectra. Interestingly, the additional low energy shoulder is shown up around 0.3 eV in the 90° spectra, suggesting the existence of the low-energy excitation dispersing along the *c* axis dimer. To reveal the origin of the MIT, the detailed momentum resolved measurements are required in both insulating and metallic phases.

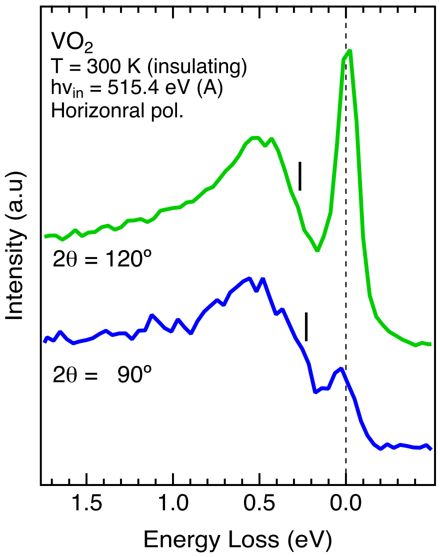

Figure 2
Scattering angle dependence of the V 2*p* RIXS spectra obtained at $h\nu_{in}$ = 515.4 eV.

Summary

We have performed the momentum resolved RIXS of VO_2. By tuning the incoming photon energy at the low energy sholder of the V 2*p* XAS, we have successfully observed the *dd*-excitation in the insulating phase. The RIXS spectra show the scattering angle depdence at the lower loss-energy side of the peak structure due to the *dd*-excitation due to the low energy excitations dispersing along the *c*-axis dimer.

REFERENCES

[1] F. J. Morin, Phys. Rev. Lett., **3**,34, (1959).
[2] M. Nakano, K. Shibuya, D. Okuyama, T. Hatano, S. Ono, M. Kawasaki, Y. Iwasa and Y. Tokura, Nature **487**, 459 (2012).
[3] M. W. Haverkort, Z. Hu, A. Tanaka, W. Reichelt, S. V .Streltsov, M. A. Korotin, V . I. Anisimov, H. H. Hsieh, H.-J. Lin, C. T. Chen, D. I. Khomskii, and L. H. Tjeng, Phys. Rev. Lett. **95**, 196404 (2005).
[4] T. C. Koethe, Z. Hu, M. W. Haverkort, C. Schler-Langeheine, F. Venturini, N. B. Brookes, O. Tjernberg, W. Reichelt, H. H. Hsieh, H.-J. Lin, C. T. Chen, and L.H. Tjeng, Phys. Rev. Lett. **97**, 116402 (2006).
[5] Y. Harada, M. Kobayashi, H. Niwa, Y. Senba, H. Ohashi, T. Tokushima, Y. Horikawa, S. Shin, and M. Oshima, Rev. of Sci. Instrum. **83**, 013116 (2012).

ELECTRONIC-STRUCTURE MAPPING OF ELECTRODE MATERIALS BY O*PERANDO* PHOTOELECTRON SPECTROMICROSCOPY USING AN ALL-SOLID-STATE LI-ION-BATTERY

Eiji Hosono[a,b], Takaaki Sudayama[a], Daisuke Asakura[a,a], Keishi Akada[c,c], Naoka Nagamura[c],
Koji Horiba[e], Masaharu Oshima[f], Yoshihisa Harada[b, b, f]

[a] National Institute of Advanced Industrial Science and Technology (AIST), Research Institute for Energy Conservation, 1-1-1 Umezono, Tsukuba, Ibaraki 305-8568, Japan
[b] AIST-UTokyo Advanced Operando-Measurement Technology Open Innovation Laboratory, 5-1-5 Kashiwanoha, Kashiwa, Chiba 277-8565, Japan
[c] Institute for Solid State Physics (ISSP), The University of Tokyo, 5-1-5 Kashiwanoha, Kashiwa, Chiba 277-8581, Japan
[d] National Institute for Materials Science, Research Center for Advanced Measurement and Characterization, 1-2-1 Sengen, Tsukuba, Ibaraki 305-0047, Japan
[e] Photon Factory, Institute of Materials Structure Science, High Energy Accelerator Research Organization (KEK), 1-1 Oho, Tsukuba, Ibaraki 305-0801, Japan
[f] Synchrotron Radiation Research Organization, The University of Tokyo, 7-3-1 Hongo, Bunkyo-ku, Tokyo, 113-8656, Japan

Li-ion-batteries (LIBs) play an important role as an energy storage of electric vehicles to establish a sustainable society. Understanding the charge-discharge mechanism of LIBs is essential to improve their properties, such as high energy density, long cycle life, safety operation, and thermal stability. Many operando researches have been done on the electronic properties of the constituent elements using, e.g. hard X-ray absorption spectroscopy, while the character of the most functional 3d electrons in LIBs have not yet been fully understood. Recently Asakura and Hosono *et al*. have successfully introduced operando soft X-ray absorption / emission spectroscopy as a novel method to understand the functional metal 3d states during Li-intercalation/deintercalation process in LIB cathode materials [1].

However, the X-ray beam size is usually larger than the particle size of active materials in LIB electrodes. Most of the synchrotron X-ray spectroscopy techniques provide averaged information of electrodes within several-tens or several-hundreds μm scale limited by the X-ray beam size. A spectromicroscopy with a high spatial resolution is of particular importance because that method can detect changes of various electronic structures of transition metals and oxygen, which are correlated closely with the Li-intercalation/deintercalation, in a single particle. The local information of the materials is important for further understanding the charge/discharge mechanisms.

We propose the use of operando photoelectron spectromicroscopy to add spatially resolved information to the electronic structure of single-crystal LIB cathode materials. We developed an all-solid-state LIB cell that can operate under ultra-high vacuum condition and obtained operando photoelectron spectra of $LiCoO_2$ cathode at charge/discharge states using 3DnanoESCA station at BL07LSU of SPring-8 [2].

Figure 1 shows the Co 3p and Li 1s spectra of single crystalline $LiCoO_2$ in the all-solid-state LIB cell for operando measurement. The peak position of each Co 3p spectrum from initial, charge, and discharge condition is not changed. It is considered that strong hybridization between Co 3d and O 2p orbitals causes the charge-polarization at the oxygen side. We should measure the narrow scan of O 2p for detail discussion. However, oxygen components in the dry polymer as solid-state electrolyte is overlapped with the oxygen atom in $LiCoO_2$. We will create oxygen free measurement system.

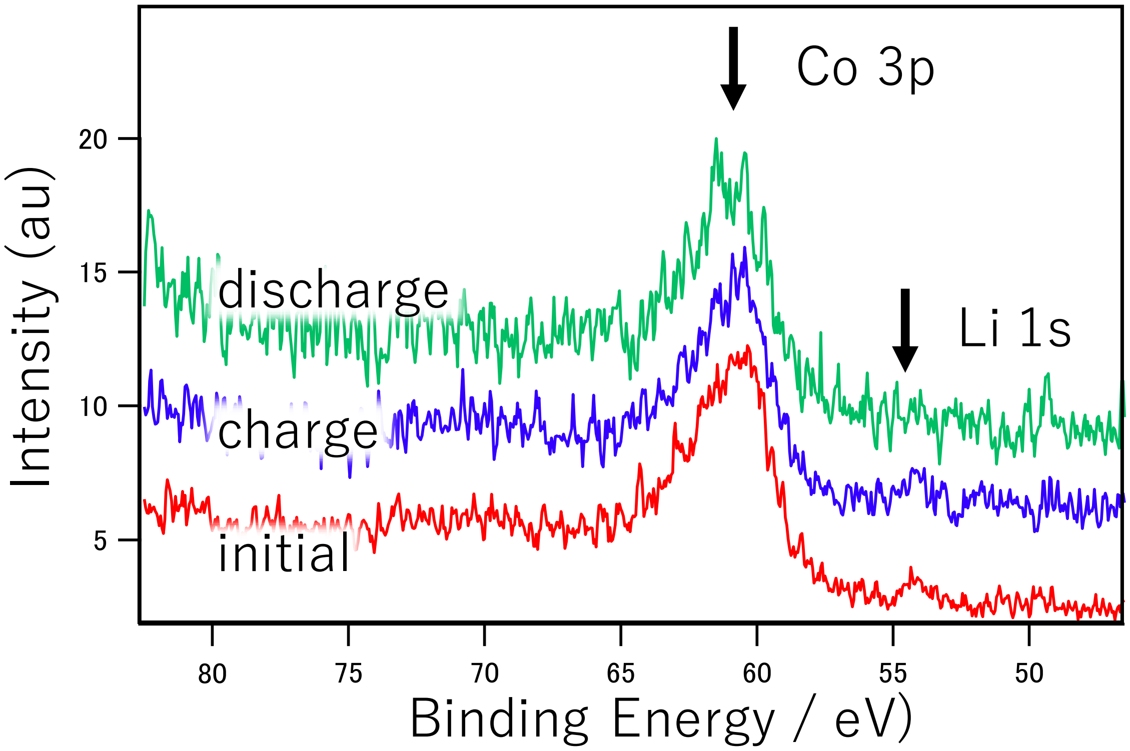

Figure 1 Co 3p and Li 1s spectra of $LiCoO_2$.

ACKNOWLEDGEMENT

This work is partially conducted on the basis of the International joint research program for innovative energy technology by Ministry of Economy, Trade and Industry, Japan. A part of this work was supported by TIA collaborative research program "Kakehashi"

REFERENCES

[1] D. Asakura, E. Hosono, H. Niwa, H. Kiuchi, J. Miyawaki, Y. Nanba, M. Okubo, H. Matsuda, H.S. Zhou, M. Oshima, and Y. Harada, "Operando Soft X-ray Emission Spectroscopy of $LiMn_2O_4$ Thin Film Involving Li-ion Extraction/insertion Reaction", Electrochem. Commun. **50**, 93 (2015).

[2] K. Horiba, Y. Nakamura, N. Nagamura, S. Toyoda, H. Kumigashira, M. Oshima, K. Amemiya, Y. Senba, H. Ohashi, Scanning photoelectron microscope for nanoscale three-dimensional spatial-resolved electron spectroscopy for chemical analysis. Rev. Sci. Instrum. **82,** 113701 (2011).

VALENCE-CHANGE MAPPING OF TRANSITION METALS BY O*PERANDO* PHOTOELECTRON SPECTROMICROSCOPY USING AN ALL-SOLID-STATE LI-ION-BATTERY

Eiji Hosono[a,b], Takaaki Sudayama[a], Daisuke Asakura[a,a], Keishi Akada[c,c], Naoka Nagamura[c],
Koji Horiba[e], Masaharu Oshima[f], Yoshihisa Harada[b, b, f]

[a] National Institute of Advanced Industrial Science and Technology (AIST), Research Institute for Energy Conservation, 1-1-1 Umezono, Tsukuba, Ibaraki 305-8568, Japan
[b] AIST-UTokyo Advanced Operando-Measurement Technology Open Innovation Laboratory, 5-1-5 Kashiwanoha, Kashiwa, Chiba 277-8565, Japan
[c] Institute for Solid State Physics (ISSP), The University of Tokyo, 5-1-5 Kashiwanoha, Kashiwa, Chiba 277-8581, Japan
[d] National Institute for Materials Science, Research Center for Advanced Measurement and Characterization, 1-2-1 Sengen, Tsukuba, Ibaraki 305-0047, Japan
[e] Photon Factory, Institute of Materials Structure Science, High Energy Accelerator Research Organization (KEK), 1-1 Oho, Tsukuba, Ibaraki 305-0801, Japan
[f] Synchrotron Radiation Research Organization, The University of Tokyo, 7-3-1 Hongo, Bunkyo-ku, Tokyo, 113-8656, Japan

For realizing a sustainable low-carbon society, development of high-performance lithium-ion battery (LIB) for electric vehicles is one of the most important research subjects. In the presence of trade-offs among the performances such as energy density, power performance, cycle performance, and safety property, it is difficult to fulfill all the requirements for those properties. Comprehensive researches and developments are highly important because the combination of the materials among the cathode, anode, and electrolyte is crucial for the improvement of total performances of LIB. Understanding of the redox reactions and structural/electronic properties for the materials in LIBs is necessary to design/create innovative materials for LIBs. Thus, cutting-edge analyses are inevitable in addition to the materials development.

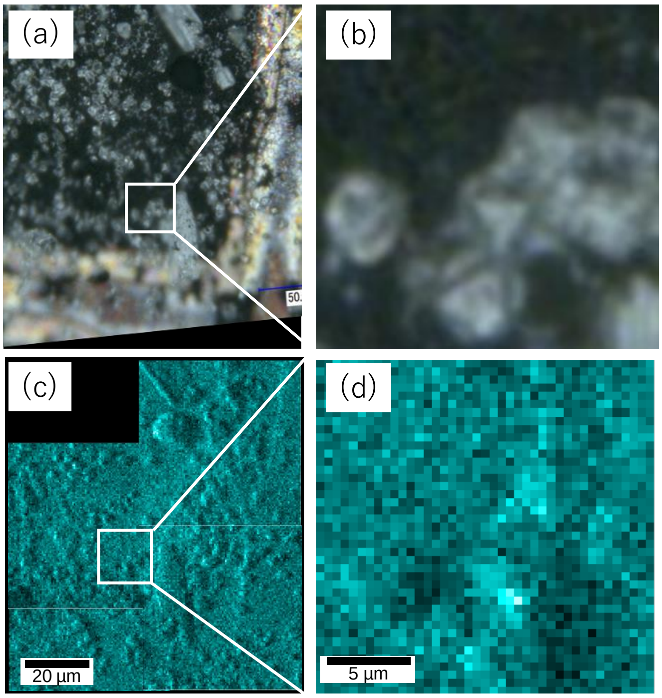

Figure 1 (a)(b) optical microscope images and (c)(d) corresponding XPS images of working electrode

Synchrotron radiation X-ray spectroscopy is a useful technique to understand the crystal structure and electronic structure of LIB materials. We have been studying the charge-discharge mechanisms in LIBs by the electronic-structure analysis based on soft X-ray spectroscopy. The operando soft X-ray emission spectroscopy under the charge-discharge operation is an important technique to investigate the redox reactions of electrode materials [1]. Furthermore, spatially resolved electronic-structure information is of particular importance because the redox reaction by charge-discharge reaction should depend on the position like a facet of an electrode material and the interfaces between the electrode materials and electrolytes.

We report operando photoemission spectromicroscopy of single crystalline $Li_4Ti_5O_{12}$ (an anode material) [2] by 3DnanoESCA [3] with all-solid-state LIB. The soft X-ray photoemission spectromicroscopy experiments has been conducted at BL07LSU of SPring-8.

Figures 1 shows (a) optical microscope image of the surface of working electrode constructed by Cu mesh, $Li_4Ti_5O_{12}$, carbon as conductive additive, and polymer solid-state electrolyte, along with (b) the enlarged images of the white squared area in (a), while Fig. 1 (c) and (d) are the corresponding XPS images. The 3DnanoESCA obtains corresponding XPS images of working electrode to images of optical microscope.

ACKNOWLEDGEMENT

This work was conducted under the international joint research program for innovative energy technology by METI, Japan and TIA collaborative research program “Kakehashi”.

REFERENCES

[1] D. Asakura, E. Hosono, H. Niwa, H. Kiuchi, J. Miyawaki, Y. Nanba, M. Okubo, H. Matsuda, H.S. Zhou, M. Oshima, and Y. Harada, “Operando Soft X-ray Emission Spectroscopy of $LiMn_2O_4$ Thin Film Involving Li-ion Extraction/insertion Reaction”, Electrochem. Commun. **50**, 93 (2015).

[2] K. Akada, T. Sudayama, D. Asakura, H. Kitaura, N. Nagamura, K. Horiba, M. Oshima, E. Hosono, Y. Harada, “Operando measurement of single crystalline Li4Ti5O12 with octahedral-like morphology by microscopic X-ray photoelectron spectroscopy”, J. Electron Spectrosc. Relat. Phenom. **233**, 64 (2019).

[3] K. Horiba, Y. Nakamura, N. Nagamura, S. Toyoda, H. Kumigashira, M. Oshima, K. Amemiya, Y. Senba, H. Ohashi, Scanning photoelectron microscope for nanoscale three-dimensional spatial-resolved electron spectroscopy for chemical analysis. Rev. Sci. Instrum. **82,** 113701 (2011).

THE ELECTRONIC STRUCTURE OF HYDRATED WATER IN BIOCOMPATIBLE POLYMERS

Daiki Murakami[1,2], Kosuke Yamazoe[3], Tomoya Ueda[2], Toshiki Sonoda[2],
Jun Miyawaki[3], Yoshihisa Harada[3], Masaru Tanaka[1,2]

[1]*Institute for Materials Chemistry and Engineering, Kyushu University, Japan*
[2]*Graduate School of Engineering, Kyushu University, Japan,*
[3]*Institute for Solid State Physics, The University of Tokyo, Japan*

Introduction

The role of water molecules in biological systems have long been discussed. Tanaka et al. showed by differential scanning calorimetry (DSC) that water in biocompatible polymer, poly(2-methoxyethyl acrylate) (PMEA) could be classified into three types; non-freezing water, intermediate water, and free water, while water in less biocompatible analogues lacks the intermediate water. [1] This tendency has been verified for other biocompatible polymers such as poly(ethylene glycol) (PEG) and poly(2-methacryloyloxyethy phosphorylcholine) (PMPC). Lots of experiments verified that the intermediate water is a key to control the biocompatibility of polymers. However, the detailed structural feature of the intermediate water is not clear so far.

In this work, we aimed to clarify the structural property of intermediate water by soft x-ray absorption spectroscopy (XAS) and soft x-ray emission spectroscopy (XES). XAS and XES experiments are powerful tools to determine the local hydrogen bond network of water. [2]

Experimental

XAS/XES measurement was performed at BL07LSU HORNET station in SPring-8. We prepared the PMEA spin-coated film on a SiC substrate. PMEA was synthesized by radical polymerization method. To enhance the stability of the film, small amount of PMEA with terminal thiol group was grafted on the SiC surface before the spin-coating. Similarly, the film of poly(*n*-butyl acrylate)(PBA) was prepared and used for comparison. The humid air with controlled humidity was flowed on the sample to change the water contents in the polymer films.

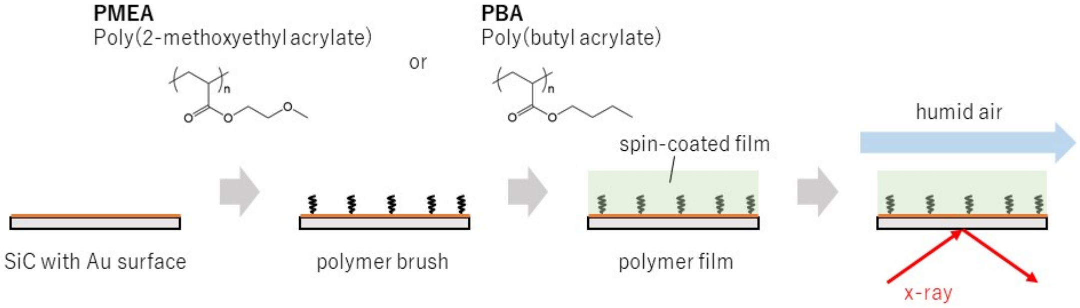

Figure 1. Sample preparation and experimental setup

Results and discussion

Figure 2 shows the XES spectra of PMEA and PBA under the humidity control. As expected the emission intensity increased as the relative humidity increased. In the hydration process of PMEA, first non-freezing water which shows the strongest interaction with polymer chains appears. Intermediate water and free water should contribute in the order of interaction strength. [3] Thus we assigned the XES spectrum in the highest humidity (95%RH) to free water which shows a similar spectral profile with bulk water having two peaks originated from tetrahedrally-coordinated and distorted hydrogen bonds. [4] In 50%RH, non-freezing water appears as a broad profile peaked at the tetrahedrally-coordinated component, along with a sharp peak at 527 eV indicating adsorbed water. It is remarkable that the 75%RH spectrum showed still a broad profile with larger tetrahedrally-coordinated and lesser distorted components compared with bulk water. We speculate this unique spectrum is closely relevant to the presence of intermediate water in PMEA. In PBA, this type of water was not observed while highly distorted but tetrahedrally coordinated component [5] dominates at higher humidity, which would rather lead to a decreased biocompatibility.

The XAS spectra in the same humidity conditions were shown in Fig. 3. We notice that water in PMEA showed increased post-edge profile peaked around 540 eV in 75%RH, which is relevant to the interpretation of the XES profile in 75%RH. In PBA, the profile peaked at 537 eV is again characteristic for the distorted but tetrahedrally-coordinated component [5].

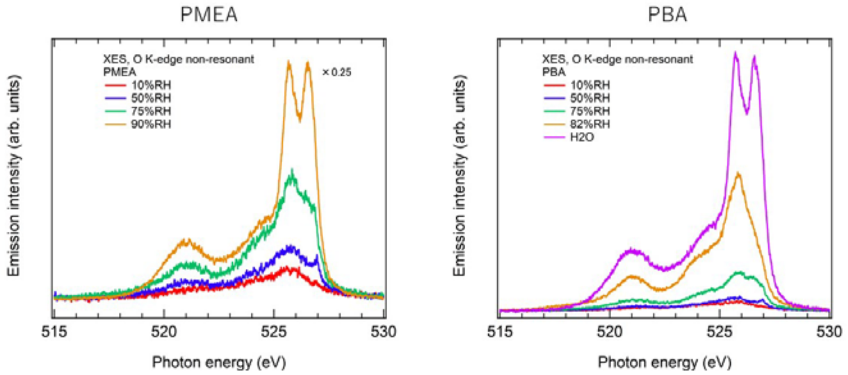

Fig. 2 XES spectra of PMEA and PBA under the humidity control.

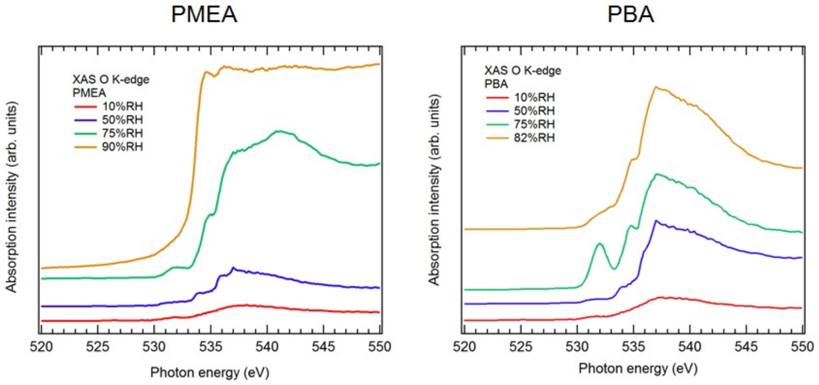

Fig. 3 XAS spectra of PMEA and PBA under the humidity control.

Conclusion

The biocompatible polymer PMEA has characteristic XAS/XES profile with larger tetrahedrally-coordinated and lesser distorted components, while the less biocompatible polymer PBA dominantly has highly distorted but tetrahedrally coordinated component. This study provides a clue to reveal the detailed mechanism of biocompatibility and design highly biocompatible polymers.

References

[1] M. Tanaka et al. *Polymer Journal*, **2015**, *47*, 114.
[2] T. Fransson et al. Chem. Rev, **2016**, *116*, 7551.
[3] S. Morita et al. *Langmuir* **2007**, *23*, 3750.
[4] T. Tokushima et al. *Chemical Physics Letters*, **2008**, *460*, 387.
[5] K. Yamazoe et al. *Langmuir* **2017**, *33*, 3954.

SOFT X-RAY ABSORPTION AND EMISSION SPECTROSCOPY OF THE INTERMEDIATE WATER IN BIOCOMPATIBLE POLYMERS

Daiki Murakami[1,2], Kosuke Yamazoe[3], Tomoya Ueda[2],
Jun Miyawaki[3], Yoshihisa Harada[3], Masaru Tanaka[1,2]

[1]*Institute for Materials Chemistry and Engineering, Kyushu University, Japan*
[2]*Graduate School of Engineering, Kyushu University, Japan,*
[3]*Institute for Solid State Physics, The University of Tokyo, Japan*

Introduction

Poly(2-methoxyethyl acrylate) (PMEA) is an outstanding biocompatible polymer widely used in the medical field. We have revealed that the water molecules contained in PMEA can be classified into three types: non-freezing water, free water, and intermediate water. Non-freezing water does not crystallize below 0 °C due to a strong interaction with a polymer chain. Free water crystallizes at approximately 0 °C like bulk water. Intermediate water does not freeze at 0 °C but exhibits melting/crystallization at lower temperature due to the weak interaction with polymer chains. It has been well recognized that the intermediate water dominates the biocompatibility of polymers. [1] However, the structure and characteristics of intermediate water remains unclear so far. In this work, we aimed to shed light on the states of intermediate water using soft x-ray absorption/emission spectroscopy (XAS/XES), which is a powerful tool to determine the local hydrogen bond network of water.

Experimental

We prepared the PMEA brush on SiC substrate by grafting-to method. First we synthesized the PMEA with terminal thiol group (PMEA-SH, Fig. 1) by raft polymerization. The molecular weight of PMEA-SH was estimated to be 38,000 g/mol and molecular weight distribution was 1.1 from Gel Permeation Chromatography. The SiC substrate (Au coated) was dipped in PMEA-SH/MeOH solution (200 μmol/l) for 1 hour, and then rinsed with MeOH and dried. The graft density of obtained PMEA brush was c.a. 0.1 chains/nm^2.

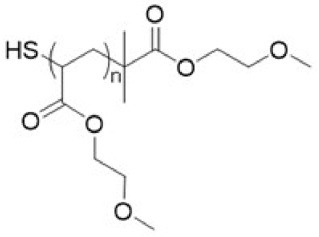

Fig. 1 Chemical structure of PMEA-SH

XAS/XES measurement was performed at BL07LSU HORNET Station in SPring-8. The humid air with controlled humidity was flowed on the sample to change the water contents in the brush sample.

Results and discussion

In the XES spectrum of bulk liquid water, basically two significant peaks are observed. One is around 525.6 eV indicating the presence of ordered (tetrahedrally coordinated) hydrogen bonds, and the other is around 526.8 eV corresponding to distorted hydrogen bonds. [2] As shown in Fig. 2(a), in the low humidity range below 65%RH, a broad profile peaked at the tetrahedrally-coordinated component dominates, along with a sharp peak at 527.1 eV which we consider water adsorbed on PMEA, Above 75%RH, slight increase in the distorted hydrogen bonds was observed and finally in 90%RH the spectrum is very similar to that of bulk water.

For more detailed consideration, the difference spectra between the neighboring XES spectra were calculated (Fig. 2(b)). We notice that the differential spectrum of 75%-65%

showed only a broad peak centered around the tetrahedrally coordinated hydrogen bond. We expect this is the feature of non-freezing water, which is strongly bounded to the adsorbed water on the polymer chain. In contrast, the difference spectrum of 90%-78% showed two peaks, which is very similar to the spectrum of bulk water. This is assigned to free water, which weakly interacts with the polymer chain. The spectrum of 78%-75% is particularly interesting. It showed a broad peak centered at the middle of ordered and distorted peaks. In XAS spectra (Fig. 3), we observed tetrahedrally coordinated behavior (increment of absorption intensity in post-edge region) of water at around 75%RH. These results indicate that the hydrogen bond network of water in PMEA, especially around 75%RH, is obviously different from that of free water and non-freezing water. We consider this is the unique characteristics of intermediate water.

We successfully detected the intermediate water in PMEA, whereas the origin of intermediate water is still unclear. Further investigation will be performed in our future work in order to clarify the essential feature of intermediate water and the role on biocompatibility.

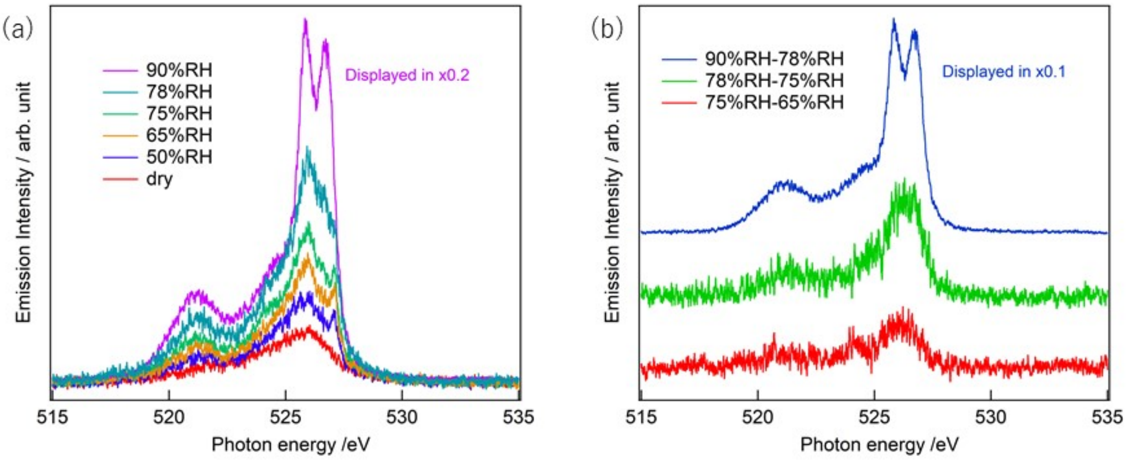

Fig. 2 (a) XES spectra of PMEA under the humidity control.
(b) Difference between the spectrum in each humidity.

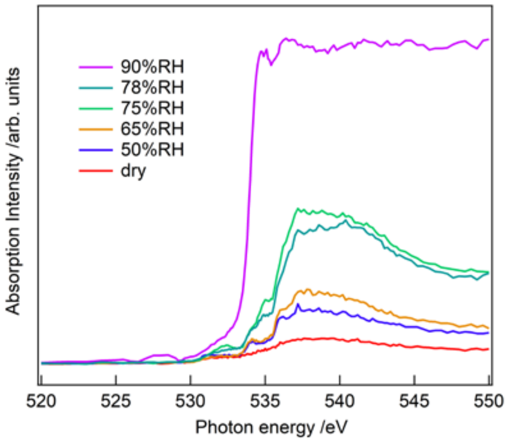

Fig. 3 (a) XAS spectra of PMEA under the humidity control.

References

[1] M. Tanaka et al. *Polymer Journal*, **2015**, *47*, 114.

[2] T. Tokushima et al. *Chemical Physics Letters*, **2008**, *460*, *387*

Dispersionless Charge Excitations for $La_{2-x}Sr_xNiO_{4+\delta}$ probed by Oxygen *K*-edge Resonant Inelastic X-ray Scattering

Kohei Yamagami[1], Kenji Ishii[2], Yasuyuki Hirata [1], Keisuke Ikeda[1], Jun Miyawaki[1],
Yoshihisa Harada [1], Shun Asano[3], Masaki Fujita[3], and Hiroki Wadati[1]

[1] *Institute for Solid State Physics, The University of Tokyo*
[2] *Synchrotron Radiation Research Center, National Institutes for Quantum and Radiological Science and Technology*
[3] *Institute for Materials Research, Tohoku University*

In order to investigate the correlation between the charge stripe state and high temperature superconductivity for $La_{2-x}Sr_xCuO_4$ (LSCO), the identification of the characteristics of the charge stripe state for layered-perovskite type Ni oxides $La_{2-x}Sr_xNiO_{4+\delta}$ (LSNO) is required since the charge stripe states for LSCO and LSNO are caused by the doped holes [1,2]. Since single spin-flip excitations are forbidden, charge excitations are mainly observed by not only Ni *K*-edge resonant inelastic X-ray scattering (RIXS)[3,4] but also the O *K*-edge RIXS. To directly observe the charge excitations due to the doped holes, in this study, we carried out O *K*-edge RIXS, which was already performed for LSCO and successfully revealed dispersive charge excitations [5], for LSNO.

Momentum resolved O *K*-edge RIXS for LSNO was measured at HORNET station in SPring-8 BL07LSU. The number of doped holes n_h ($\equiv x + 2\delta$) of LSNO was 0.1 (no charge stripe state) and 0.33 (with the charge stripe state), respectively. The figure shows the comparison among O *K*-edge RIXS spectra for n_h = 0.1 and 0.33 at incident energy ($h\nu_{in}$) of 528.7 eV. Four constant loss energy peaks were successfully observed, indicated by labels *a*-*d* in that figure. Peaks *b* and *c* correspond to charge excitations observed in the optical conductivity spectra [6,7]. Momentum resolved RIXS spectra indicate that the clear energy dispersions of charge excitations were not observed, reflecting the localized charge excitations. This dispersionless of charge excitations in LSNO are different from that of LSCO where the charge excitations have clear energy dispersion.

These localized charge excitations of doped holes are consistent with the insulating behavior in conductivity [6] and related to the size of polaron reported by the optical conductivity measurement [8]. The simple mean-field theory applied to a three-band Hubbard model predicts that the stabilization energy of the polaron originating from electron-phonon coupling is correlated with the charge transfer energy between nickel and oxygen ions [9] and it could be an origin of wider hole density of charge-stripe ordered phase in the nickelates than that in the cuprates [10].

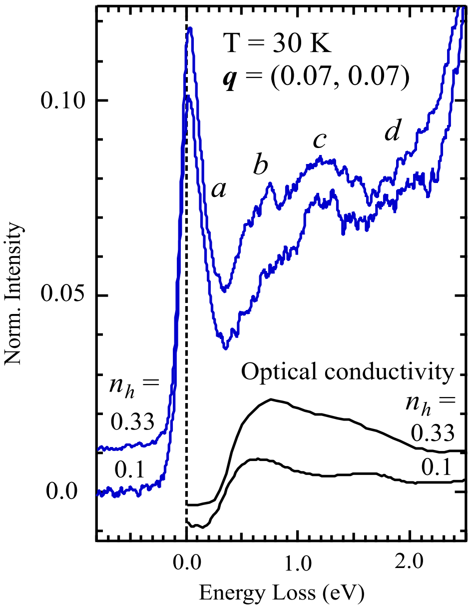

Figure: O *K*-edge RIXS spectra for LSNO (n_h = 0.1 and 0.33). Optical conductivity spectra for n_h = 0.1 and 0.33 are shown in the bottom [6,7].

REFERENCES

[1] J. M. Tranquada *et al.*, PRB **54**, 12318 (1996).
[2] H. Kimura *et al.*, PRB **67**, 140503(R) (2003).
[3] S. Wakimoto *et al.*, PRL **102**, 157001 (2009).
[4] L. Simonelli *et al.*, PRB **81**, 195124 (2010).
[5] K. Ishii *et al.*, PRB **96**, 115148 (2017).
[6] T. Katsufuji *et al.*, PRB **54**, 14230 (1996).
[7] T. Ido, *et. al.*, PRB **44**, 12094 (1991).
[8] X-X. Bi and P. C. Eklund, PRL **70**, 2625 (1993).
[9] J. Zaanen and P. B. Littlewood, PRB **50**, 7222 (1994).

[10] K. Ishizaka *et al.*, PRB **67**, 184418 (2003).

Charge Excitations for single- and bi-layered Manganate probed by Resonant Inelastic X-ray Scattering at Oxygen *K*-edge

Kohei Yamagami[1], Kenji Ishii[2], Jun Miyawaki[1], Yoshihisa Harada [1], Hideki Kuwahara[3], and Hiroki Wadati[1]

[1] *Institute for Solid State Physics, The University of Tokyo*
[2] *Synchrotron Radiation Research Center, National Institutes for Quantum and Radiological Science and Technology*
[3] *Department of Physics, Sophia University, Tokyo*

Effect of carrier doping into insulating transition-metal oxides is a central issue in strongly correlated transition-metal systems and parent insulators are categorized into two types: Mott insulators and charge-transfer insulators. In the latter, the energy of charge transfer from the oxygen 2*p* to the transition-metal *d* levels is smaller than the on-site Coulomb repulsion of the *d* electrons. Among them, the layered manganate $LaSr_2Mn_3O_7$ (LSMO327), $La_{0.5}Sr_{1.5}MnO_4$ (LSMO214) has the checkerboard-type charge ordering within the insulating due to the doped holes[1]. In particular, LSMO327 collapses/reorders charge ordering with decreasing temperature, not seen in LSMO214. In order to investigate the charge excitation originating from doped holes, being related to the charge ordering, we have performed the resonant inelastic X-ray scattering (RIXS) at oxygen *K*-edge for LSMO327 and LSMO214.

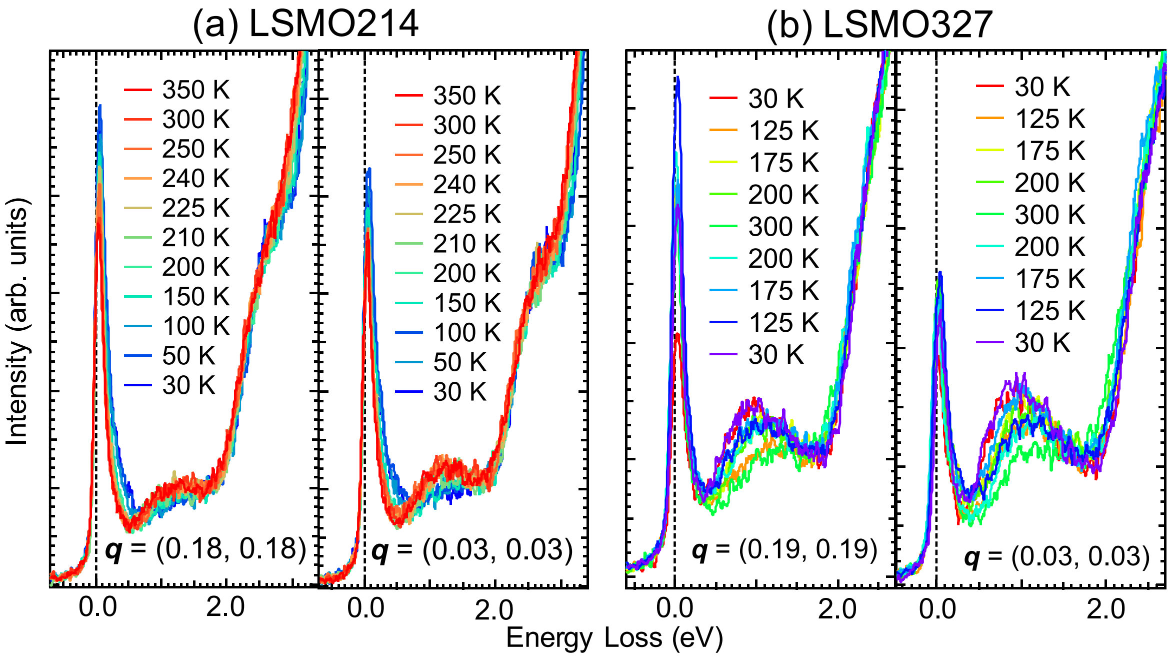

Fig.1 Temperature and momentum transfer (***q***) dependence of O *K*-edge RIXS spectra for (a) LSMO214 and (b) LSMO327. In LSMO327, the temperature is raised and lowered between 30 K and 300 K.

The O *K*-edge RIXS of single crystal LSMO327 and LSMO214 was carried out at HORNET station in SPring-8 BL07LSU. Figure 1 shows the O *K*-edge RIXS spectra for (a) LSMO214 and (b) LSMO327 at incident energy ($h\nu_{in}$) of 529.5 eV with σ-polarization parallel to the MnO_2 plane. Combining with the O *K*-edge X-ray absorption and $h\nu_{in}$ dependence of RIXS spectra, we judge that the excitations at 0 eV, 1.3 eV, and 2.5 eV are elastic including in phonons and magnons, fluorescence, and the charge excitation respectively. It is found that the charge excitation has energy dispersionless corresponding localized character. This can be considered that there is presence of short-range correlation such as the electron-lattice coupling due to the Jahn-Teller distortion. On the other hand, interestingly, the peak and intensity of fluorescence component depends on the temperature. The multi-gaussian fitting results indicates that this temperature behavior is associated with the electron resistivity, which reflects the electronic states at unoccupied conduction bands within LSMO214 and LSMO327, not being seen in $La_{2-x}Sr_xNiO_4$ in our previous O *K*-edge RIXS study.

Moreover, in LSMO327, the peak and intensity of fluorescence component depends on the momentum transfer ($\boldsymbol{q}$) at 125 K corresponding to the collapsing charge ordering. Since the superlattice reflection characteristic of orbital ordering has been observed around 125 K[2], we consider that the fluorescence component includes in the degree of freedom for e_g orbital. At present, we are discussing about the origin of temperature and $\boldsymbol{q}$ change that appears in the fluorescence components and the correlation with the orbital order being observed simultaneously within LSMO214 and LSMO327.

References

[1] J. Dho, *et al.,* J. Phys.: Condens. Matter, **13**, 3655 (2001).
[2] T. Kimura, *et al.,* Phys. Rev. B **58**, 11081 (1998).

Development of Coherent Soft X-ray Diffraction Imaging Technique for Observation of Ultra-fast Magnetic Dynamics

Yuichi Yamasaki[1,2,3], Kohei Yamamoto[4,5], Yuichi Yokoyama[1,6], Yasuyuki Hirata[4],
Hiroki Wadati4,7, and Taka-hisa Arima[3,8]

[1]*Research and Services Division of Materials Data and Integrated System (MaDIS),*
National Institute for Materials Science (NIMS)

[2]*PRESTO, Japan Science and Technology Agency (JST)*

[3]*RIKEN Center for Emergent Matter Science (CEMS)*

[4]*The Institute for Solid State Physics, University of Tokyo*

[5]*Department of Materials Molecular Science, Institute for Molecular Science*

[6] *Japan Synchrotron Radiation Institute (JASRI)*

[7]*Graduate School of Material Science, University of Hyogo*

8Department of Advanced Materials Science, University of Tokyo

Introduction:

Topological magnetic textures have attracted a great deal of attention and have been extensively studied in the recent years. In a chiral magnetic material with broken spatial inversion symmetry, a vortex-like stable magnetic structure called a magnetic skyrmion may emerge under certain temperatures and magnetic field conditions. A triangle crystal state of the magnetic skyrmion was first observed in the chiral magnet MnSi by using small-angle neutron scattering, and it was later observed in real space via Lorentz-type transmission electron microscopy. Since then, magnetic skyrmions have also been observed by using soft X-ray techniques, such as small-angle scattering, X-ray holography, and transmission soft X-ray microscope. Since a magnetic skyrmion behaves like an isolated particle in a magnetic material and can be controlled by an external field, it is a promising candidate for information media in next-generation spintronics devices. To understand its characteristics, such as its response to an applied external field, observing skyrmions in real space with high temporal and spatial resolution is important.

In the present study, we have developed a diffractometer of small-angle resonant soft x-ray magnetic scattering for performing the coherent x-ray magnetic imaging of magnetic textures at the undulator beamline BL07LSU, SPring-8. The apparatus is equipped with a vacuum chamber having a background pressure of $< 1 \times 10^{-5}$ Pa, a CCD camera (2048x2048 pixel, Princeton Instrument), a direct beam catcher, and a sample holder [Fig. 1]. In order to observe transmitted soft x-ray scattering, we prepared thin plate sample thinned by FIB method or magnetic thin films fabricated on Si_3N_4 substrates.

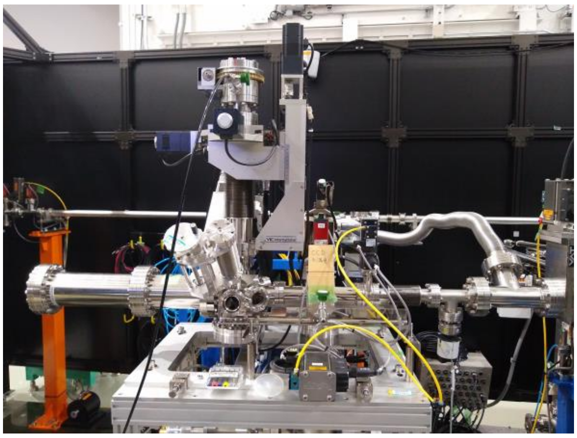

Figure 1: Diffractometer for resonant soft x-ray small-angle scattering developed at BL07LSU, SPring-8.

Results:

First, we measured the diffraction pattern from the pinhole in order to evaluate the performance of the instrument and the coherence of the incident soft x-rays. Figure 2 shows diffraction pattern and its line profile from a double pin hole of 0.5 μm in diameter. The striped diffraction pattern is derived from coherent diffraction of a double pinhole separated by 8 μm distance. As a result, it is suggested that the coherent length was at least 8 μm.

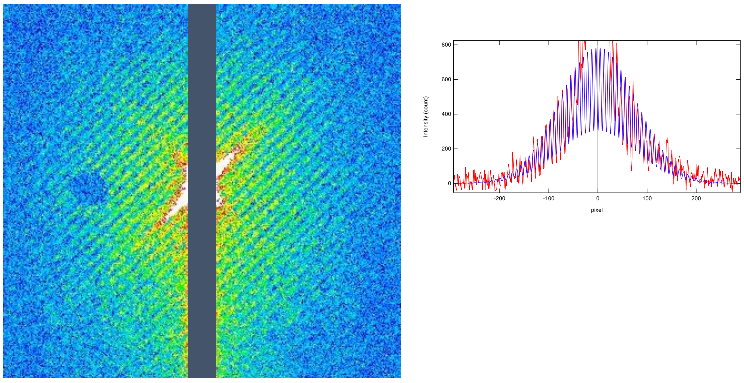

Figure 2: Coherent diffraction pattern (left) and its line profile (right) from a double pinhole, fabricated on Ta deposited Si_3N_4 membrane. The size of the pinholes are 0.5 μm in diameter, and their spacing is 8 μm. Red and blue lines indicate the observed and calculated curves, respectively.

Subsequently, diffraction patterns from magnetic multilayer thin films FdGd/Co and from magnetic thin film Co/Pt were measured at Fe L-edge (~702 eV) and at Co L-edge (~776 eV), respectively. The samples were placed over the pinhole to cut out the coherent light. When the light energies were changed to make it non-resonant, the diffraction pattern were observed to change, which suggested that magnetic scatterings reflecting ferromagnetic domain structure were observed.

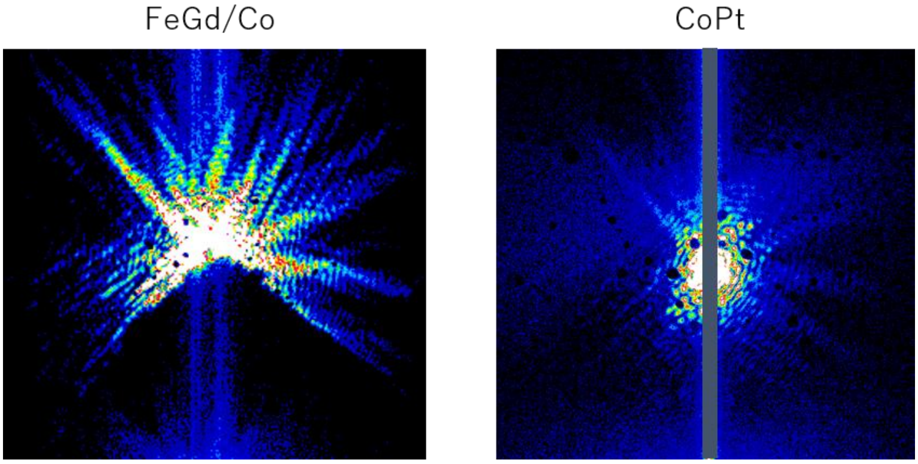

Figure 3: Magnetic diffraction pattern from magnetic thin films FeGd/Co and CoPt.

Conclusion:

In this study, we developed the equipment for resonant soft x-ray small angle scattering and succeeded in observing the magnetic scattering from the magnetic thin film. In the future, we aim to observe temporal variations of the magnetic structure in real space by combining the coherent soft x-ray diffraction imaging technique with time-resolved pump-probe measurement.

Development of time-resolved ambient pressure X-ray photoelectron spectroscopy system at SPring-8 BL07LSU

Susumu Yamamoto and Iwao Matsuda

The Institute for Solid State Physics, The University of Tokyo

Introduction

Operando spectroscopy of catalytic reactions is essential for our understanding of reaction mechanisms as well as the rational development guidelines for novel catalysts. Ambient pressure X-ray photoelectron spectroscopy (AP-XPS) is one of the most powerful *operando* spectroscopies, which permits the investigation of the electronic and chemical states of adsorbates and catalysts under gas atmospheres at near-ambient pressure. However, the typical temporal resolution of AP-XPS has been limited to ms, and thus the dynamic processes faster than ms could not be studied. At SPring-8 BL07LSU, we developed time-resolved X-ray photoelectron spectroscopy (tr-XPS) in ultrahigh vacuum by combining ultrafast optical laser with X-ray in a pump-probe fashion. tr-XPS allows one to monitor the time-evolution of electronic structures of samples in real time. The temporal resolution of tr-XPS is ~50 ps, which is determined by the pulse width of probe X-ray.

In this study, we aimed to develop a time-resolved ambient pressure X-ray photoelectron spectroscopy (tr-APXPS) by combining AP-XPS with tr-XPS. tr-APXPS will permit the monitoring of photocatalytic reactions in real time; all the players in photocatalytic reactions such as photo-excited carriers, adsorbates, substrates can be investigated by tr-APXPS.

Experimental

All the experiments were performed at the soft X-ray undulator beamline BL07LSU at SPring-8 [1]. AP-XPS experiments were carried out using an AP-XPS apparatus that combines a differentially pumped electron analyzer (SPECS, PHOIBOS 150 NAP) with an ambient-pressure gas cell [2]. A one-dimensional delay-line detector (DLD) is adopted as a detector of the electron analyzer.

Femtosecond (fs) laser systems were installed at SPring-8 BL07LSU. The fs laser pulses were synchronized to synchrotron radiation X-ray pulses, and the delay time of fs laser pump pulse relative to X-ray probe pulse can be controlled. There were two different fs laser systems; high pulse energy and low repetition rate (mJ, 1 kHz) and low pulse energy and high repetition rate (μJ, 208 kHz). Optical parametric amplifier (OPA) was installed in both laser systems, which can change the wavelength of fs laser. In the present study, high pulse energy and low repetition rate (mJ, 1 kHz) laser system was used.

Results and discussion

In the development of tr-APXPS, a new soft X-ray chopper was installed at SPring-8 BL07LSU. The repetition rate of probe X-ray was 208 kHz in the H-mode operation of SPring-8, which was much larger than that of pump laser (1 kHz). Soft X-ray chopper can reduce the repetition rate of probe X-ray to 1 kHz to match that of pump laser. Consequently, time-resolved XPS measurements became possible with the same experimental setup as in conventional static XPS measurements. Figure 1 shows a picture of a soft X-ray chopper installed at SPring-8 BL07LSU and its operation of pulse selection. Soft X-ray chopper blocks all the X-ray pulses that are not used in pump-probe time-resolved measurements. This decreases unnecessary burden on the sample and the detector. Thus, the photon flux can be increased by opening slits in X-ray beamline to improve measurement efficiency.

Test tr-APXPS measurements were performed on the naturally oxidized *p*-type Si(111) (SiO_2/*p*-Si(111)) surface in 1 mbar CO_2. As a result of excitation by pump laser (800 nm, 1 kHz), we could observe the energy shift of Si 2*p* core level due to surface photovoltage effect. In addition, we could detect the energy shift of CO_2 gas phase peak in O 1*s* core level. The energy shift of gas phase peak in AP-XPS reflects the change of the sample work function. Notably, the energy shift was different between Si 2*p* and O 1*s* core levels. The present preliminary experimental results of tr-APXPS demonstrate that this experimental method can provide a wealth of information in photo-excited systems and will be very suited to study various light-induced reactions including photocatalysts and plasmonic chemical reactions.

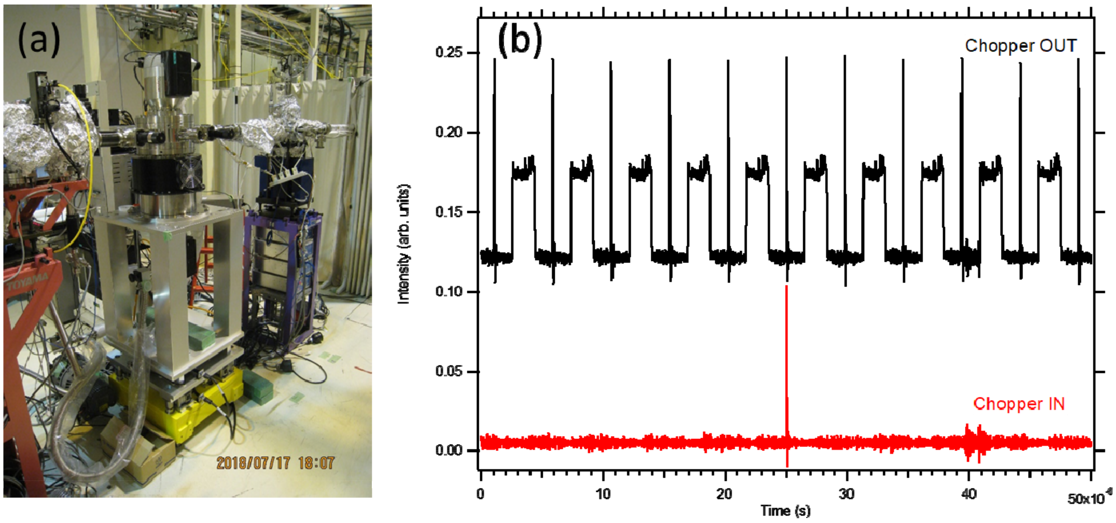

Figure 1. (a) Soft X-ray chopper installed at SPring-8 BL07LSU (b) Time structure of soft X-ray pulses with soft X-ray chopper OUT and IN. The repetition rate of soft X-ray pulses was decreased to 1 kHz.

REFERENCES

[1] S. Yamamoto *et al.*, J. Synchrotron Rad. **21**, 352-365 (2014).

[2] T. Koitaya, S. Yamamoto, *et al.*, Topics in Catalysis **59**, 526-531 (2016).

Sabatier reaction on a Ni/SiO$_2$ catalyst studied by *operando* soft X-ray spectroscopies

Susumu Yamamoto[1], Jun Miyawaki[1], Jiayi Tang[1,2], Takanori Koitaya[1,3,4], Takuma Tokunaga[1],
Yu Shibata[1], Yuka Kosegawa[1], Kosuke Yamazoe[1], Kozo Mukai[1], Shinya Yoshimoto[1],
Yoshihisa Harada[1], Jun Yoshinobu[1], Iwao Matsuda[1]

[1] *The Institute for Solid State Physics, The University of Tokyo*

[2] *Graduate School of Engineering, University of Hyogo*

[3] *Department of Materials Molecular Science, Institute for Molecular Science*

[4] *Japan Science and Technology Agency (JST),*
Precursory Research for Embryonic Science and Technology (PRESTO)

Introduction

Sabatier reaction, $CO_2 + 4H_2 \rightarrow CH_4 + 2H_2O$, is the hydrogenation reaction of CO_2 into CH_4. This catalytic reaction now attracts great interest as a key step in the "Power-to-Gas" technology that converts renewable electricity into gas fuels. Although the development of methane synthesis catalysts with higher catalytic activity and selectivity is now highly demanded, the lack of direct experimental observation of working catalysts impedes our understanding of reaction mechanisms as well as the rational development guidelines for novel catalysts.

In this study, we aimed to investigate Sabatier reaction on a silica-supported nickel (Ni/SiO$_2$) catalyst under reaction conditions using ambient-pressure soft X-ray photoelectron and absorption spectroscopies (AP-XPS/XAS). In the *operando* observation of Ni/SiO$_2$ catalyst, the catalytic activity was simultaneously monitored using mass spectrometer, and the chemical states of the working catalyst were clarified by soft X-ray spectroscopies.

Experimental

The experiments were performed at the soft X-ray undulator beamline BL07LSU at SPring-8 [1]. AP-XPS experiments were carried out using an AP-XPS apparatus that combines a differentially pumped electron analyzer (SPECS, PHOIBOS 150 NAP) with an ambient-pressure gas cell. The details of the AP-XPS apparatus can be found in our previous publication [2]. AP-XAS experiments were carried out at X-ray emission spectroscopy endstation at BL07LSU. AP-XAS spectra were measured in total electron yield and in partial fluorescence yield. Home-developed five stage differential pumping system allows the windowless delivery of soft X-ray photons to a sample even in atmospheric pressures.

Results and discussion

The catalytic activity of Ni/SiO_2 catalyst (64 wt% Ni) was studied as a function of temperature (Figure 1). The Ni/SiO_2 catalyst was exposed to the mixed gas of 0.7 mbar CO_2 and 2.1 mbar H_2, and the sample temperature was increased in a stepwise manner from 300 K to 373 K, 473 K, and 573 K. The change in gas composition with temperatures was monitored by mass spectrometer. When the sample temperature was increased from 373 K to 473 K and 573 K, the signals for the reactant gases (CO_2 and H_2) decrease in intensity; the signals for the product species (CH_4, CO, and H_2O) increase in intensity. Therefore, both Sabatier reaction and reverse water gas shift reaction occur on the Ni/SiO_2 catalyst in the reaction conditions studied here.

Next the chemical state of Ni nanoparticles during catalytic reactions was evaluated by Ni 2*p* XPS and Ni *L*-edge XAS spectra. The comparison with Ni reference spectra revealed that the chemical state of Ni particles was NiO before reactions and then converted into a mixed state of metallic Ni and NiO during reactions. The correlation between the chemical states of Ni and catalytic activities was thus experimentally established.

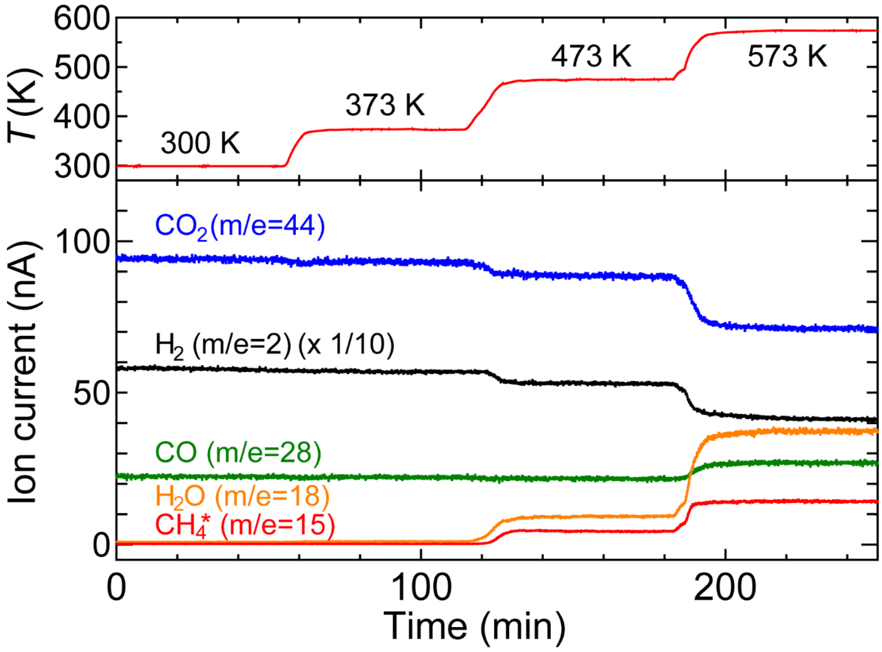

Figure 1. Catalytic activity measurements of Ni/SiO_2 catalyst. Gas composition was monitored by mass spectrometer, while the Ni/SiO_2 catalyst was heated in a stepwise manner from 300 K to 373 K, 473 K, and 573 K in the mixed gas of 0.7 mbar CO_2 and 2.1 mbar H_2.

REFERENCES

[1] S. Yamamoto *et al.*, J. Synchrotron Rad. **21**, 352-365 (2014).

[2] T. Koitaya, S. Yamamoto, *et al.*, Topics in Catalysis **59**, 526-531 (2016).

PHOTOEMISSION MICROSCOPY OF MOTT INSULATOR Ca_2RuO_4 UNDER ELECTRIC FIELD

Y. Takasuka[1], A. Hishikawa[1], D. Ootsuki[1], C. Sow[2], S. Yonezawa[2], Y. Maeno[2],
F. Nakamura[3], N. Nagamura[4], T. Yoshida[1]
[1]Grad. Sch. of Human & Environ. Studies., Kyoto Univ.,
[2]Dept. of Phys., Kyoto Univ., [3]Dept. Edu. Creat. Eng., Kurume Inst. Tech., [4]NIMS

Introduction

A Mott insulator Ca_2RuO_4 is known to show an insulator-to-metal transition (MIT), which is driven by chemical substitution, temperature, and applying hydrostatic pressure. Recently, Nakamura *et al*. reported that the MIT is also induced by applying a dry-battery level electric-field at room temperature [1]. Even more surprisingly, strong diamagnetism under electric current is discovered [2]. The diamagnetism is stronger than that in other nonsuperconducting materials. In strongly correlated electron systems, the domain structure is often observed in the vicinity of MIT. Indeed, the spatial growth of the current-induced metallic domain was observed by infrared nano-imaging and optical-microscopy measurements [3]. In this work, we have performed a soft x-ray photoemission microscopy in order to investigate the spatial dependence of the electronic structure for Ca_2RuO_4.

Experiments

Single crystals of Ca_2RuO_4 were grown by a floating zone method. The gold wires with a diameter of 100 µm were attached to the terminals both ends of the sample using silver epoxy. The electric field was applied parallel to the ab-plane. The voltage-current characteristics were measured *in situ* during the measurements by a two-probe method using a DC *V-I* source/monitor (Keithley 2450). The photoemission microscopy was performed using a three-dimensional nanoscale electron-spectroscopy chemical analysis (3D nano-ESCA) system that was installed at BL07LSU of SPring-8. The present data were acquired with linearly polarized light at $h\nu = 1000$ eV. The clean surfaces were obtained by *in situ* cleavage in vacuum with a base pressure better than 8.2×10^{-9} Pa. All data were collected at room temperature.

Results and discussion

Figure 1 (a) shows the *IV* curves at $T = 300$ K. The Ru $3d_{5/2}$ core-level photoemission spectra under the electric field are displayed in Figs. 1 (c) and (d). The spectra are integrated within the region (100×100 µm ^{2}) as shown in Fig. 1(b). Figure 1 (c) shows the current dependence of Ru 3 $d_{5/2}$ core-level spectra. The width of Ru $3d_{5/2}$ spectrum with current ($I = 50$ mA) becomes broad as compared with that without current ($I = 0$ mA), which indicates the appearance of the screened peak at lower binding energy than the main peak. This suggests that the screening electrons increase by applying electric-field. To investigate the spatial dependence of the electronic structure under current, we compared the spectra of the region A with that of the region B as shown in Fig.1 (d). The spectrum of the region A is slightly broader than that of the region B, suggesting that there is the inhomogeneous spatial distribution of the screening electrons.

Summary

In order to investigate the spatial dependence of the electronic structure, we have performed the soft x-ray photoemission microscopy for Ca_2RuO_4. We found the spatial dependence of the Ru $3d_{5/2}$ core-level spectra under electric current, suggesting the spatial growth of the current-induced metallic domain.

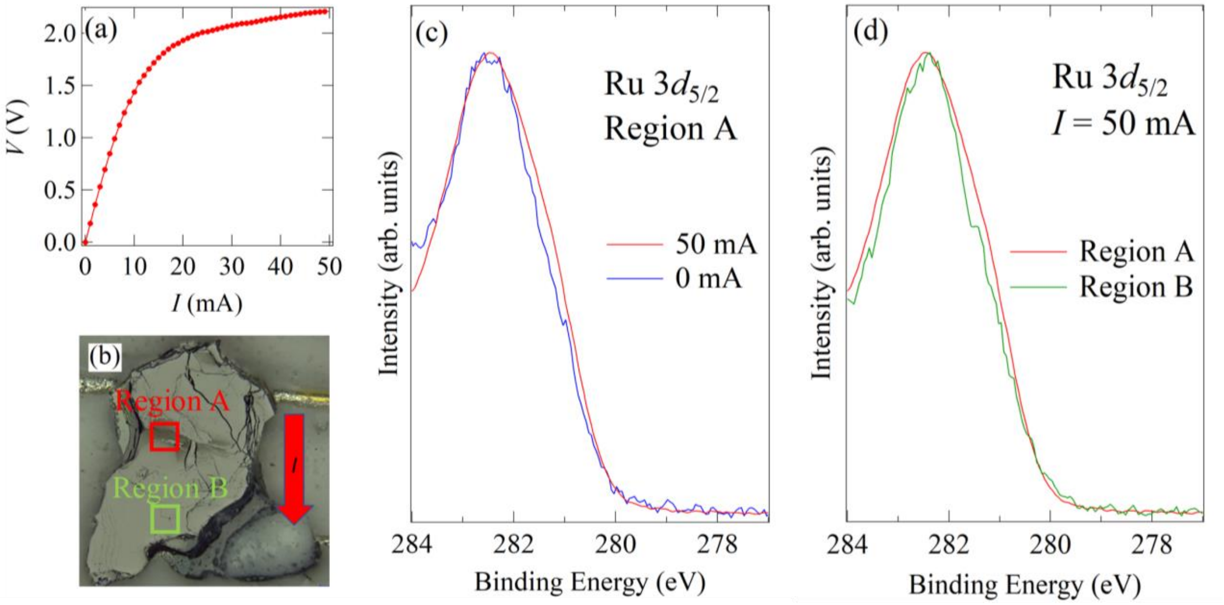

Fig. 1. (a) Current-voltage curve at T = 300 K. (b) Photo of Ca_2RuO_4 crystal. The square indicates the measured region. Arrow shows the direction of current. (c) Ru $3d_{5/2}$ core-level spectra with/without current in the region A of Fig. 1 (b). (d) Ru $3d_{5/2}$ core-level spectra of the region A and B with I = 50 mA.

REFERENCES

[1] F. Nakamura *et al.*, Sci. Rep. **3**, 2536 (2013).
[2] C. Sow *et al.*, Science **358**, 1084 (2017).
[3] J. Zhang *et al.*, Phys. Rev. X **9**, 011032 (2019).

OBSERVATION OF ELECTRONIC STRUCTURE FOR Ca_2RuO_4 UNDER ELECTRIC FIELD BY SOFT X-RAY ABSORPTION SPECTROSCOPY

Teppei Yoshida[1], Yukie Takasuka[1], Daisuke Shibata[1], Daiki Ootsuki[1], Jun Miyawaki[2],
Yoshihisa Harada[2], Chanchal Sow[3], Shingo Yonezawa[3], Yoshiteru Maeno[3],
Fumihiko Nakamura[4]
[1]*Graduate School of Human and Environmental Studies, Kyoto University*
[2]*Synchrotron Radiation Laboratory, The Institute for Solid State Physics, The University of Tokyo*
[3]*Graduate School of Science, Kyoto University*
[4]*Department of Education and Creation Engineering, Kurume Institute of Technology*

Recently, the correlated electronic states under electric field are receiving growing interest. It has been reported that a Mott insulator Ca_2RuO_4 shows an intriguing electric-field induced insulator to metal transition with a nonlinear conductivity [1]. The threshold electric field E_{th} of ~ 40 V/cm for Ca_2RuO_4 is weakest among the Mott insulators. Particularly, a giant diamagnetism under electric current has been reported by Sow *et al* [2]. Thus, it would be desirable to understand how the applied low electric field changes the insulating state of Ca_2RuO_4 and causes the giant diamagnetism.

The Mott insulator Ca_2RuO_4 undergoes the metal to insulator (MI) transition at T_{MI} = 357 K accompanied by structural deformation such as a rotation, tilt, and/or compression of the RuO_6 octahedra [3]. In the insulating phase of Ca_2RuO_4, two of the four Ru 4*d* electrons occupy the ground d_{xy} orbital and the two remaining electrons are located in the $d_{xz/yz}$ orbitals owing to the framework of the crystal field [4]. According to studies by angle-resolved photoemission spectroscopy and dynamical mean-field theory (DMFT), the paramagnetic insulating state of Ca_2RuO_4 was interpreted as an orbital-dependent band-Mott insulator, which is characterized by the coexistence of the band insulating state of d_{xy} orbital and the Mott insulating states of half-filled $d_{xz/yz}$ orbitals [5].

Here, we performed soft x-ray absorption spectroscopy (XAS) measurements on Ca_2RuO_4 under electric field at SPring-8 BL07LSU to investigate the current-induced evolution in the electronic structure. High-quality single crystals of Ca_2RuO_4 were grown by using the floating-zone method. The gold wires were attached to the terminals both ends of the sample using silver epoxy. In order to monitor the sample temperature under an electric field, the sample was mounted directly on a Pt thermometer. The sample and the thermometer were glued to sapphire substrate with silver epoxy and an insulating adhesive. The electric field was applied parallel to the *ab*-plane and the voltage-current characteristics were measured *in situ* during the XAS measurements. The sample temperature is controlled by liquid helium and the sample heating is less than 3 K during all measurements.

Figure 1 shows the *in situ* IV characteristics of the sample. The open squares denote the points at which the spectra were measured. Figures 1(a) and 1(b) are O 1*s* x-ray absorption spectra of Ca_2RuO_4 under current taken at 300 K and 200 K, respectively. The two peaks located at 528.5 and 529.1 eV are the t_{2g}-derived spectra and are transitions to apical and in-plane oxygen sites [6]. On the other hand, the structures at ~531 and 534 eV are the e_g-derived spectra and are assigned to be $d_{3z^2-r^2}$ and $d_{x^2-y^2}$ band, respectively [7]. With increasing current, the spectral intensity for the apical oxygen sites decreases while that for the in-plane oxygen sites increases. This trend is consistent with the previous XAS study under electric field and is suggestive of the increase in the number of d_{xy} holes with increasing current [8]. As for the e_g-derived region, the $d_{x^2-y^2}$ band shifts to the lower energy while the $d_{3z^2-r^2}$ band shifts to the higher energy with increasing current. The spectral change in the t_{2g}-derived spectra is relevant to the elongation of the RuO_6 octahedra [6]. Also the band shifts in the e_g-derived region indicates the change in the crystal-field splitting. These results suggest that the current-induced change in the electronic structure is related to the structural change of the octahedra and may give a hint to understand the origin of the diamagnetism.

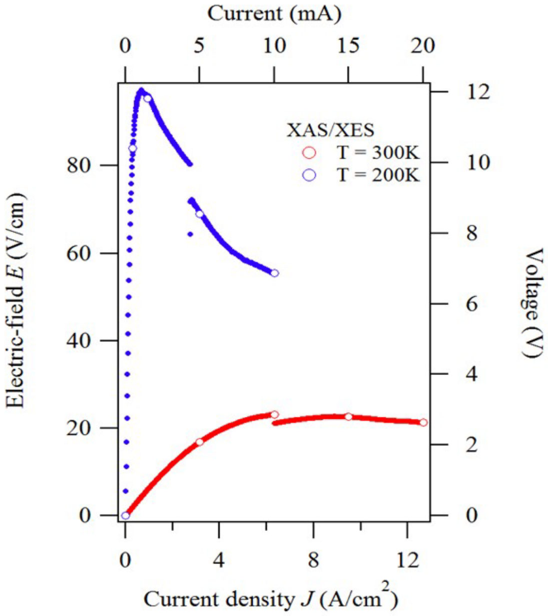

Figure 1. Current density J variations of the electric field E at T = 300 K and 200 K. The open circles indicate the points at which the x-ray absorption spectra were taken.

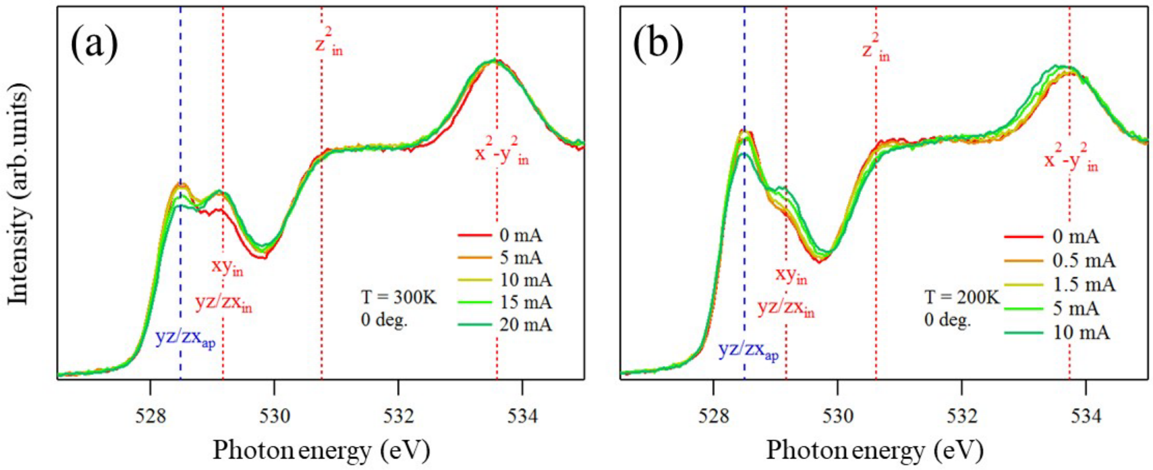

Figure 2. O 1s x-ray absorption spectra of Ca_2RuO_4 under current. The spectra are taken at 300 K (a) and at 200 K (b) at normal incidence.

REFERENCES

[1] F. Nakamura *et al.*, Sci. Rep., **3**, 2536 (2013).
[2] C. Sow *et al.*, Science, **358**, 6366 (2017).
[3] O. Friedt *et al.*, Phys. Rev. B **63**, 174432 (2001).
[4] E. Gorelov *et al.*, Phys. Rev. Lett. **104**, 226401 (2010).
[5] D. Sutter *et al.*, Nat. Commun. 8, 15176 (2017).
[6] T. Mizokawa *et al.*, Phys. Rev. Lett. **87**, 077202 (2001).
[7] H. J. Noh *et al.*, Phys. Rev. B **72**, 052411 (2005).
[8] M. Sakaki *et al.*, J. Phys. Soc. Jpn. **82**, 093707 (2013).

HYDROGENATION OF FORMATE SPECIES
ON A SINGLE ATOM ALLOY MODEL CATALYST Pd-Cu(111)
STUDIED BY AMBIENT PRESSURE XPS

Takuma Tokunaga, Susumu Yamamoto, Shion Nakano, Tomoki Matsuda, Kozo Mukai, Iwao Matsuda and Jun Yoshinobu
The Institute for Solid State Physics, The University of Tokyo

1. Introduction

In this research, we have prepared a single-atom alloy Pd-Cu(111) surface as a model catalyst for the hydrogenation of adsorbed formate species. Single-atom alloy catalyst (SAAC) has recently been attracting attention [1]. SAAC is an alloy catalyst in which a very small amount of foreign metal atoms are embedded in the surface of a substrate metal; the foreign atom gives an additional catalytic function keeping the main catalytic function of the substrate metal. In order to elucidate the chemical species and electronic states of the surface, we have observed the adsorption and reaction processes using ambient-pressure X-ray photoelectron spectroscopy (AP-XPS) and mass spectroscopy in operando conditions. High resolution XPS using synchrotron radiation can detect a very small amount (a few percent or less) of isolated metal atoms embedded in the surface of a host metal substrate. By operando observation using mass spectrometry and AP-XPS, the function of SAAC in the catalytic reaction would be elucidated.

Copper is a typical catalyst for methanol synthesis from CO and CO_2 [2]. However, copper is not very active for the dissociative adsorption of H_2. Here, we prepared the SAAC sample in which Pd was deposited on a Cu single crystal surface. The host Cu substrate is suitable for methanol synthesis reaction and water gas shift reaction. When a small amount of Pd atoms are deposited on the Cu (111) surface, hydrogen molecules are easily dissociated at the Pd site. The produced hydrogen atoms spill over on the Cu surface; these hydrogen atoms may be highly reactive [1]. We examined the reaction processes between hydrogen atoms and formate species on the Pd-Cu(111) surface by AP-XPS and mass spectroscopy.

2. Experiments

The present SAAC sample was prepared on Cu(111) at 380 K by vacuum deposition of Pd in an ultra-high vacuum chamber connected to the AP-XPS system at BL07 LSU, SPring-8. Gaseous formic acid was introduced on the Pd-Cu(111) SAAC sample at low temperature (~100 K). This sample was heated at 300 K to produce formate species (HCOO) on the surface. The adsorbed species and electronic states of the sample were investigated by high resolution XPS. Under hydrogen introduction, AP-XPS spectra were continuously measured.

3. Results and discussions

A small amount of Pd atoms were deposited on the Cu(111) surface at 380 K in order to prepare the present SAAC sample, and the surface was characterized by XPS. Figure 1 shows Pd 3d XPS spectra of the Pd-Cu(111) surface (hν = 680 eV). The single-component Pd $3d_{3/2}$ and $3d_{5/2}$ peaks are observed at 340.7 and 335.4 eV, respectively. Thus, we confirmed that

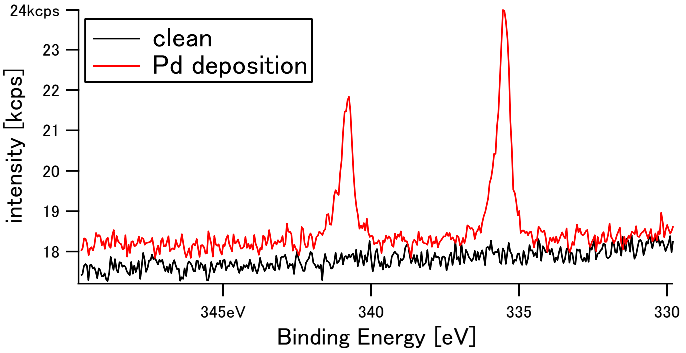

Figure 1 XPS spectra of Pd 3d region of clean Cu(111) and Pd-Cu(111) surfaces.

the Pd-Cu(111) SAAC was prepared. The Pd coverage was estimated to be about 0.04 ML.

Next, this Pd-Cu(111) sample was cooled at about 100 K and exposed to gaseous formic acid in the UHV chamber. By heating this sample at 300 K, most formic acid molecules were desorbed and a small amount of formate species of about 0.1 monolayer was produced, which is similar to the case of formic acid on Cu(111) [3]. The C1s and O1s of formate species on Pd-Cu(111) were observed at 287.6 eV and 531.2 eV.

Then, the sample was moved to the AP cell for AP-XPS measurement in 2 mbar H_2 at controlled temperature. During this process, simultaneous observation of AP-XPS and mass spectroscopy was conducted. From the AP-XPS measurement of C1s and O1s (Figure 2), it was found that the formate species hardly changed at 300 K to 350 K, but the formate species decreased in intensity above 370 K. On the other hand, our thermal desorption experiments have shown that decomposition and desorption of formate into CO_2 and H_2 occurs at 420 K on Pd-Cu(111). When hydrogen (2 mbar) was introduced to the formate on Pd-Cu (111), the decreased of formate species occurred at lower temperature. This might suggest the hydrogenation of formate occur and new chemical species desorb from the surface. However, we could not detect new intermediate adsorbed species or significant change in mass spectroscopy measurements. Thus, further experiments are necessary to determine if the formate is simply decomposed or reacted under ambient hydrogen.

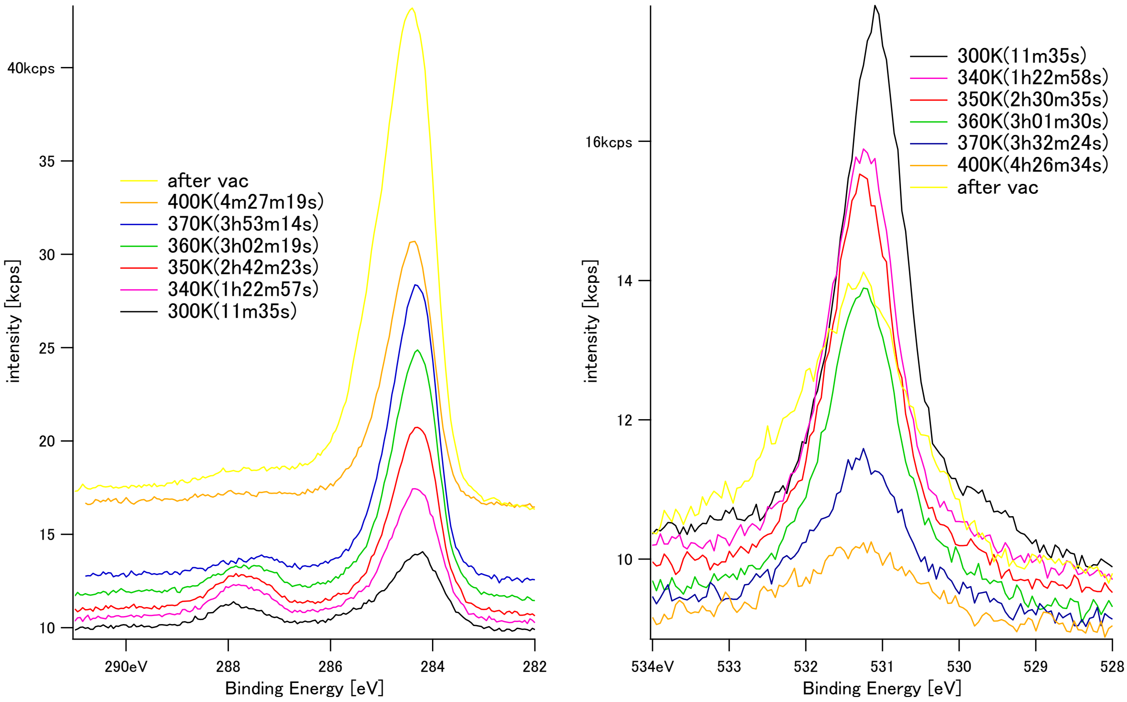

Figure 2 C 1s (left) and O 1s (right) XPS spectra of formate/Pd-Cu(111) under 2 mbar H_2 as a function of elevated temperature.

REFERENCES

[1] Georgios Kyriakou, Matthew B. Boucher, April D. Jewell, Emily A. Lewis, Timothy J. Lawton, Ashleigh E. Baber, Heather L. Tierney, Maria Flytzani-Stephanopoulos, and E. Charles H. Sykes, Science, **335,** 1209 (2012).

[2] L. Llyoyd, “Handbook of Industrial Catalysts”, Springer, 2011.

[3] Yuichiro Shiozawa, Takanori Koitaya, Kozo Mukai, Shinya Yoshimoto, and Jun Yoshinobu, J. Chem. Phys. **143**, 234707 (2015).

INVESTIGATING ANTIFERROMAGNETIC-FERROMAGNETIC PHASE TRANSITION IN GdBaCo$_2$O$_{5.5}$ THIN FILM BY RESONANT SOFT X-RAY MANGETIC DIFFRACTION

Yujun Zhang[1,2*], Yasuyuki Hirata[2], Kou Takubo[2], Kohei Yamagami[2], Kohei Yamamoto[2], Keisuke Ikeda[2], Tsukasa Katayama[3], Akira Chikamatsu[3], Tetsuya Hasegawa[3], Hiroki Wadati[1,2]

[1] *Graduate School of Materials Science, University of Hyogo, 3-2-1 Kouto, Kamigori-cho, Ako-gun, Hyogo 678-1297, Japan*

[2] *Institute for Solid State Physics, University of Tokyo, 5-1-5 Kashiwanoha, Chiba 277-8581, Japan*

[3] *Department of Chemistry, University of Tokyo, 7-3-1 Hongo, Bunkyo, Tokyo 113-0033, Japan*

1 Introduction

Entanglement of charge, spin, lattice and orbital degrees of freedom in transition metal oxide (TMO) systems have attracted much attention recently [1]. The electric and magnetic properties of TMOs, which are dominated by the partially filled *d* orbitals, could be strongly affected by the crystal field effect from the surrounding lattice and corresponding *d*-orbital occupation. With a strongly localized feature of *d* electrons in TMO systems (especially 3*d* TMO systems), variety of ordering phenomena like magnetic ordering, charge ordering and ferroelectricity can coexist and significantly couple with each other. Tantalizing physical phenomena with prospective applications, such as high-T_c superconductivity and colossal magnetoresistance, have emerged during the investigation of strongly correlated TMO systems.

Among 3*d* TMO systems, except the famous maganites and cuprates, cobaltites have also drawn much research attention due to their specific spin-state transition of Co ions. In many cobaltite systems, for instance the most simple case, perovskite LaCoO$_3$, the competition between crystal field splitting and Hund coupling can lead to various spin states of Co ions[2]. Take Co^{3+} as an example, with a strong octahedral crystal field, low-spin (LS, $t_{2g}^6e_g^0$, S=0) state is energetically preferable and high-spin (HS, $t_{2g}^4e_g^2$, S=2) state with occupied e$_g$ orbital is preferred when crystal field is weak. In spite of LS and HS states, there is also debate that intermediate-spin (IS, $t_{2g}^5e_g^1$, S=1) state can also be realized in various cobaltites. The spin state of Co ions is very sensitive to the external condition such as temperature, pressure, magnetic field and substrate strain, etc. It is intensely reported that the magnetic properties of cobatites are dominated by the spin state of Co ions and complicated magnetic structures could be observed in quite a few cobaltite systems.

Recently, *RE*BaCo$_2$O$_x$(5<x<6, *RE* is rare earth element) systems have been intensely investigated [3-5] for their intriguing physical properties such as high oxygen conductivity, metal-insulator transiton, giant magneto-resistance and spin-state ordering, etc.. The oxygen concentration in these systems is always variable, which leads to the high oxygen mobility within the lattice. When x=6, the cystal structure is standard double perovskite with *RE* and Ba sitting at A site, while Co sitting at B site. The nominal valence state of Co is +3.5. Due to the different ionic size of *RE* and Ba ions, A site is often ordered into layers with alternating *RE* and Ba layers. When x=5, a structure with ordered oxygen vacancy layers can be formed. When x=5.5, the oxygen vacancies order into columns along a axis, resulting in 4 non-equivalent Co sites coordinated by either normal oxygen octahedra or oxygen pyramids. With this oxygen concentration, the nominal valence state of Co is +3. In this case spin-state ordering is frequently observed. For example it is reported that in PrBaCo$_2$O$_{5.5+x}$ samples HS, IS and LS coexist and contribute to a complicated magnetic structure and magnetic phase transition [4].

On the other hand, phase transition with large resistivity change entangled with antiferromagnetic(AFM)-ferromagnetic (FM) transition and spin-state transition were also explored in GdBaCo$_2$O$_{5.5-x}$ system[5]. Magnetic ordering with an index of (0 0 1/2) was clearly observed by resonant x-ray magnetic diffraction (RXMD). However, there is no report about GdBaCo$_2$O$_{5.5-x}$ thin films. In this work, we prepared high-quality epitaxial GdBaCo$_2$O$_{5.5}$ (GBCO) thin film sample on SrTiO$_3$(001) (STO) substrate and conducted the soft x-ray RXMD measurement to investigate the AFM-FM phase transition behavior.

2 Experiment

We conducted soft x-ray RXMD experiments for GBCO thin film at BL07LSU of SPring-8. Horizontal (π) and vertical (σ) linearly polarized soft x-ray at Co *L* edge was employed. The measurement temperature was changed in range of 150 K to 260 K, where the AFM-FM transition occurs.

3 Results and Discussion

Fig. 1 shows the energy scan of the (0 0 0.5) RXMD peak at Co *L* edge. Polarization dependence of the diffraction clearly confirms the magnetic origin of this diffraction peak since π polarization has more intensity than σ polarization at Co L_3 edge, and the peak intensity strongly decreases when the temperature went across the phase transition temperature (~230 K). In this energy region we can also observe the resonant scattering of Ba *M* edge, as shown by the two sharp peaks in the figure. This peak shows much larger intensity forσ polarization thanπ polarization, which indicates a charge contribution to the scattering instead of magnetism. Note that the intensity of the peak at Ba *M* edge also decreases across the phase transition temperature. This indicates that there is some concomitant structural peak with the same Q. The peaks in energy scans does not go to 0 since there is small contribution from the reflectivity of the sample.

Fig. 2 shows temperature dependent L scan of the RXMD peak. It is clear that the peak vanishes while temperature increase beyond the phase transition temperature.

Our experimental results confirmed the AFM-FM phase transition behavior in our GBCO thin film samples. These results are important for discussion about the electronic structure and magnetic ordering in GBCO thin films.

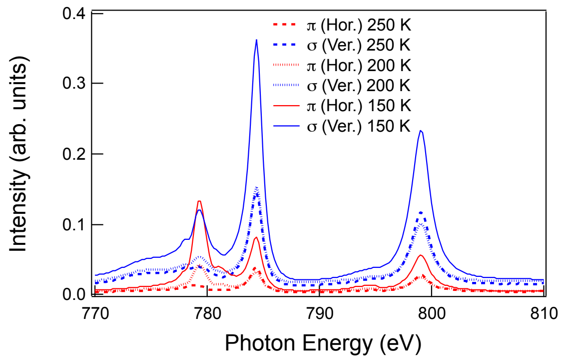

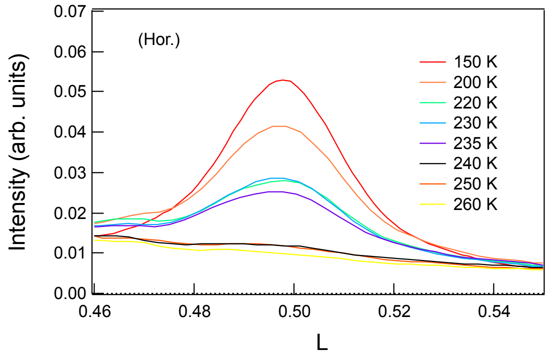

Fig.1. Energy scans of the (0 0 0.5) RMXD peak. Fig. 2. L scans of the (0 0 0.5) RMXD peak.

REFERENCES

[1] E. Dagotto. *Science* 309: 257-262 (2005).
[2] M. W. Haverkort, et al. *Phys. Rev. Lett.* 97: 176405 (2006).
[3] T. Katayama, et al. *J. Mater. Chem. C* 6: 3445 (2018).
[4] P. Miao, et al. *Phys. Rev. B* 95: 125123 (2017).
[5] M. García-Fernández, et al. *Phys. Rev. B* 78: 054424 (2008).
[6] A. A. Taskin, et al. *Phys. Rev. Lett.* 90: 227201 (2003).

Spin- and angle-resolved photoemission study of MAX phase compound V_2AlC

Takahiro Ito[1,2], Masashi Ikemoto[2], Damir Pinek[3], Koichiro Yaji[4], Masashi Nakatake[5],
Shik Shin[4], and Thierry Ouisse[3]

[1]Nagoya University Synchrotron radiation Research center (NUSR), Nagoya University, Nagoya 464-8603, Japan

[2]Graduate School of Engineering, Nagoya University, Nagoya 464-8603, Japan

[3]Grenoble Alpes, CNRS, Grenoble INP, LMGP, F-38000 Grenoble, France

[4]Institute for Solid State Physics, The University of Tokyo, 5-1-5 Kashiwanoha, Kashiwa, Chiba 277-8581, Japan

[5]Aichi Synchrotron Radiation Center, Aichi Science & Technology Foundation, Seto, Aichi 489-0985, Japan

MAX phases ($M_{n+1}AX_n$, where M is an early transition metal, A belongs to groups 13-15 and X is either C or N, n = 1 - 3) have recently attracted much attention due to their possible application to the production of a new class of two-dimensional (2D) systems called MXenes [1]. However, the bulk electronic structure of MAX phases has been studied mostly through *ab initio*, DFT calculations, mainly due to a lack of single crystalline samples. We have performed angle-resolved photoemission spectroscopy (ARPES) on several MAX phase single crystals to directly investigate the electronic structure of these systems [2,3]. Among the MAX phases, V_2AlC has been expected to be categorized as a high-symmetry point semi-metal with crossing point with some Dirac-like properties referred as "Dirac point (DP)" at the Fermi level (E_F) along ΓM line together with "nodal-line (NL)" around 0.2 eV from DFT calculation [3, 4]. To elucidate the electronic structure, especially, the existence of DP and spin-polarized states, we have performed spin - and angle - resolved ARPES (SARPES) with using a quasi - continuous - wave laser [5].

As a result, we have found the formation of the Dirac cone is consistent with DFT calculation (Fig.1). Furthermore, the SARPES clearly demonstrates spin-polarized branches (S+ and S-) in the larger electron pocket (eL), where the spin directions are opposite to each other and tangential to the Fermi surface along the ΓM line (Fig.2). Furthermore, missing of the out-of-plane spin polarization as well as inversion symmetry breaking at the observed

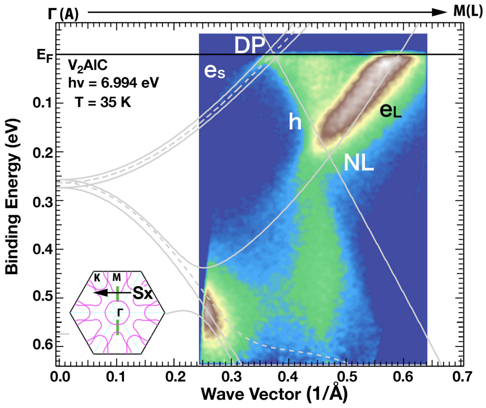

Fig. 1: Band structure along ΓM line of V_2AlC. Gray solid (dashed) lines are obtained from DFT calculation along the ΓM (AL) line. The definition of spin polarization axis in Fig. 2 is indicated by arrow on the DFT Fermi surface in the inset.

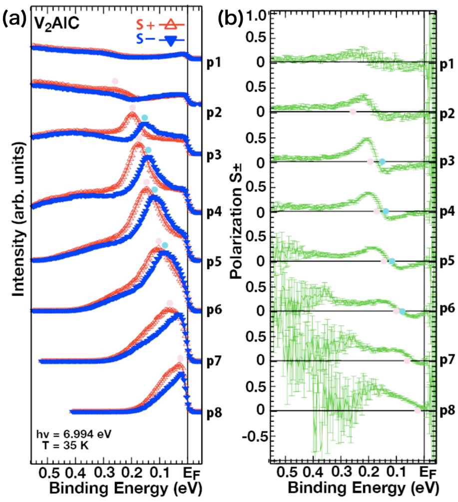

Fig. 2: SARPES spectra (S+:△; S–: ▼) (a) and spin-polarization (b) of V_2AlC at the momentum cut from p1 to p8 in Fig. 1.

spin-polarization with respect to the Γ point have been elucidated. There are at least two types of mechanism to understand the origin of the observed spin-textures. One is the existence of helical spin texture around the $\overline{\mathrm{M}}$ point with anti-parallel spin splitting due to Rashba effect [6]. The other is the formation of spin-polarized "drum-head surface states" connecting NL [7]. We expect that the present observation of the spin-textures on V_2AlC might suggest the potential of layered MAX phases as new series of topological materials.

REFERENCES

[1] M. Barsoum, MAX phases (Wiley, Weinheim 2013).
[2] T. Ito *et al.*, Phys. Rev. B **96**, 195168 (2017).
[3] D. Pinek *et al.*, Phys. Rev. B **98**, 035120 (2018).
[4] T. Zhang *et al.*, Nature **566**, 475 (2019).
[5] K. Yaji *et al.*, Rev. Sci. Instrum. **87**, 053111 (2016).
[6] V. Sunko *et al.*, Nature **549**, 492 (2017).
[7] G. Bian *et al.*, Phys. Rev. B **93**, 121113(R) (2016).

SPIN-ORBITAL TEXTURE IN QUASI-ONE-DIMENSIONAL GIANT RASHBA SYSTEM ON BI/INAS(110)-(2×1)

Takuto Nakamura[1], Yoshiyuki Ohtsubo[2,1], Ayumi Harasawa[3], Koichiro Yaji[3],

Shik Shin[3], Fumio Komori[3], Shin-ichi Kimura[2,1]

[1]*Department of Physics, graduate School of Science, Osaka University*
[2]*Graduate School of Frontier Bioscience, Osaka University*
[3]*The Institute for Solid State Physics, The University of Tokyo*

Low-dimensional electronic structures with helical spin-polarization due to spin-orbit interaction (SOI) have been extensively studied for not only basic physics but also applications to spintronic devices [1-3]. Recently, it is revealed that the spin texture of many spin-polarized two-dimensional (2D) surface states is not a simple helical one, but entangled with the orbital characters and symmetry operations of the ground states [4-6]. In such case, the spin polarization orientation of the photoelectrons drastically changes, even inverts its sign, depending on the polarization of the incident photons. So far, such spin-orbital entanglement effects have been studied in 2D systems but not extended in one-dimensional (1D) or Q1D systems yet.

In this study, we observed detailed spin-orbital texture of spin-polarized Q1D surface state on Bi/InAs(110)-(2×1) by using laser-based spin-resolved photoemission system (laser-SARPES) at ISSP. Since the surface state of this sample shows one of the largest sizes of Rashba-type spin splitting among Q1D systems [7], it is a suitable material to investigate the role of spin orbital entanglement in Q1D systems.

Figures 1 (a) and (b) show the band dispersions of the Bi/InAs(110)-(2×1) surface along Q1D chain direction measured by conventional (spin-integrated) channel of the laser-SARPE setup with p- and s- polarized photons, respectively. The pair of parabolic bands in both Figs 1 (a) and (b) lie slightly below the Fermi level. The photoelectron intensity of the parabolic band is strong overall the parabola in Fig. 1 (a), whereas its intensity decays around the centre of the surface Brillouin zone in (b), reflecting the difference in the orbital symmetry composing the parabolic band.

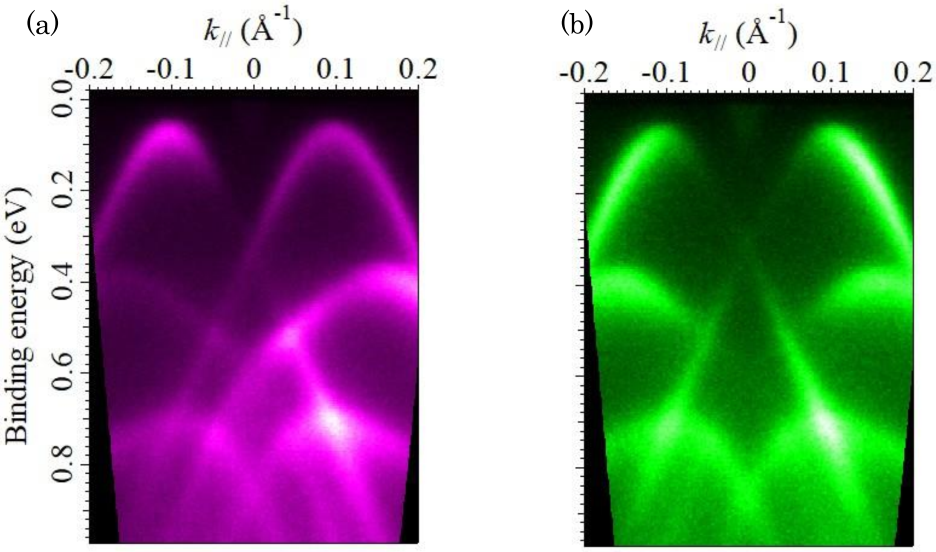

Figure 1. ARPES intensity plots of Bi/InAs(110)-(2×1) along $\overline{\Gamma}-\overline{\mathrm{X}}$ (parallel to the surface Bi chains) measured with (a) p-polarized and (b) s-polarized photons at 45 K.

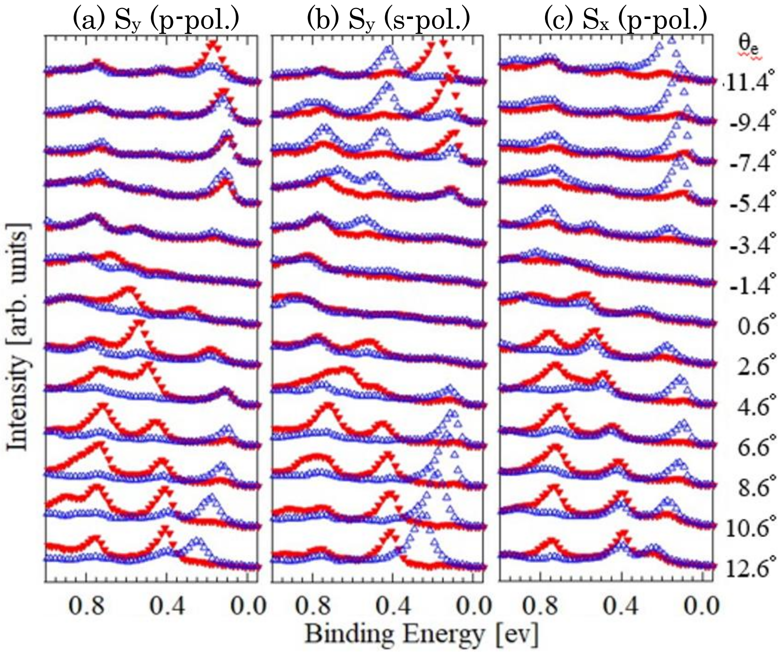

Figure 2. Spin-resolved energy distribution curves of Bi/InAs(110)-(2×1) along $\bar{\Gamma}$–$\bar{X}$ (parallel to the surface Bi chains). The solid (open) triangles correspond to spin polarization parallel (antiparallel) to (a-b) [001] and (c) [$\bar{1}$10] direction. $\theta_e = 10°$ corresponds to $k_{//} = 0.14$ Å^{-1}.

Figure 2 (a) and (b) show the spin-resolved energy distribution curves (EDCs) taken with p- and s-polarized lights, respectively. The peak positions of the EDCs agree well with the surface band dispersions shown in Fig. 1. The spin polarizations of the peaks in Figs. 2 (a) and (b) invert together with the sign inversion of the emission angles (θ_e), indicating that these spin polarizations obey time-inversion symmetry. The polarization orientations in Fig. 2 (b) are the same for one side of the emission angles. These spin-polarization is consistent with a typical, helical spin texture expected from the Rashba-type SOI. In contrast, the polarizations in Fig. 2 (a) inverts within the same parabola (*e.g.* see -5.4° and -11.4°). Based on our density-functional-theory (DFT) calculation, it would be because the fractional ratio of the orbital components changes depending on the $k_{//}$ positions; the p_z orbital of surface Bi is entangled with the opposite spin polarizations to the other orbitals. Figure 2 (c) shows spin-resolved EDCs for spin-polarization along [$\bar{1}$10], parallel to $k_{//}$. One can find clear polarizations whose sign do not change with the sign of emission angle. Apparently, such behaviour breaks the time-inversion symmetry. Since this sample has no magnetic order, this spin polarization should not from the spin polarization of the initial states but from photoexcitation process, so called final-state effect.

In summary, we have found many unconventional spin textures on Bi/InAs(110), which cannot be understood by a simple helical spin texture expected for Rashba effect. Detailed analysis including DFT calculations and spin-dependent photoexcitation processes are ongoing.

REFERENCES

[1] É. I. Rashba, Sov. Phys.-Solid State **2**, 1109 (1960).
[2] M. Z. Hasan and C. L. Kane, Rev. Mod. Phys. **82**, 3045 (2010).
[3] A. Manchon *et al.*, Nature Mat. 14, 871 (2015).
[4] K. Yaji *et al.*, Nat. Commun. **8** (2017) 14588.
[5] R. Noguchi *et al.*, Phys. Rev. B **95**, 041111(R).
[6] K. Kuroda *et al.*, Phys. Rev. B **94** (2016) 165162.
[7] T. Nakamura *et al.*, Phys. Rev. B **98**, 075431 (2018).

SPIN-POLARIZED QUASI-ONE-DIMENSIONAL METALLIC SURFACE ELECTRONIC STATE OF BI/GASB(110)-(2×1)

Takuto Nakamura[1], Yoshiyuki Ohtsubo[2,1], Kenta Kuroda[3], Ayumi Harasawa[3], Koichiro Yaji[3], Shik Shin[3], Fumio Komori[3], Shin-ichi Kimura[2,1]

[1]*Department of Physics, graduate School of Science, Osaka University*
[2]*Graduate School of Frontier Bioscience, Osaka University*
[3]*The Institute for Solid State Physics, The University of Tokyo*

Spin-polarized low-dimensional electronic structures due to Rashba effect and topological order at surfaces and interfaces are extensively studied for a fascinating playground for various spintronic phenomena [1-3]. Among them, one-dimensional (1D) or quasi-1D (Q1D) systems are expected to exhibit the interesting electronic behaviours such as the spin-dependent density-wave formation [4] and Majorana bound states at the junction with superconductors [5].

Recently, we have reported a semiconducting spin-polarized Q1D surface electronic structure of Bi/InAs(110)-(2×1) with a small bulk bandgap (~0.3 eV) [6]. As a next step for spintronic application and observation of spin-dependent electronic phenomena, to make this Q1D state metallic is desirable. In this work, we have tried to tune the Fermi-level (E_F) of the similar spin-polarized Q1D states on Bi/GaSb(110)-(2×1). The surface electronic structure of Bi/GaSb(110)-(2×1) was observed by laser-based angle-resolved photoelectron spectroscopy (ARPES) and spin-resolved ARPES (SARPES) at ISSP.

The GaSb(110) clean substrates were prepared by the repeated cycles of Ar sputtering (0.5 - 1 keV) and annealing up to 450 °C. After substrates cleaning, a few monolayers of Bi was evaporated. Subsequent annealing at 280 °C resulted in the sharp and low-background (2×1) low-energy electron diffraction patterns, suggesting the well-ordered surface atomic structure.

Figure 1 (a) is a Fermi contour of the Bi/GaSb(110)-(2×1) with the binding energy window of 0 ± 20 meV (E_F). As shown there, the metallic surface state is observed, forming a butterfly-like Fermi surface around the $\bar{Y}$ point. Figure 1 (b) shows an ARPES intensity plot along $\bar{Y}$-$\bar{M}$. The hole-bands with Rashba-type paired parabolic dispersions were observed. The obtained band dispersion is quantitatively the same as the Q1D surface states on Bi/InAs(110)-(2×1) [5].

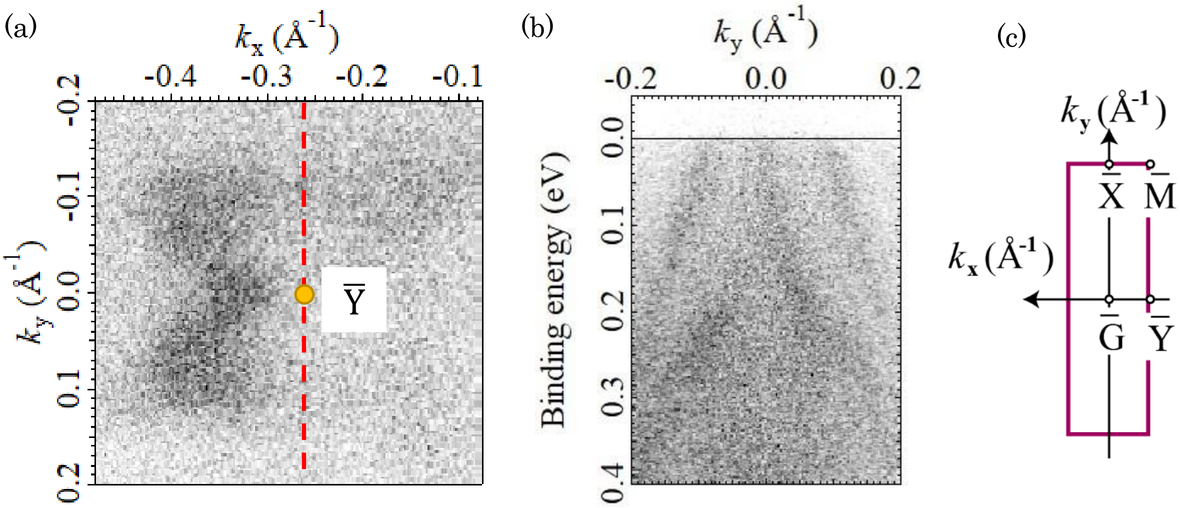

Figure 1. Electronic structure of Bi/GaSb(110)-(2×1) surface measured by ARPES at 14 K. (a) A constant-energy contour at a binding energy of 0 ± 20 meV. (b) Band dispersion along $\bar{Y}$-$\bar{M}$ (k_y = 0.26 Å^{-1}). (c) the surface Brillouin zone of Bi/GaSb(110)-(2×1).

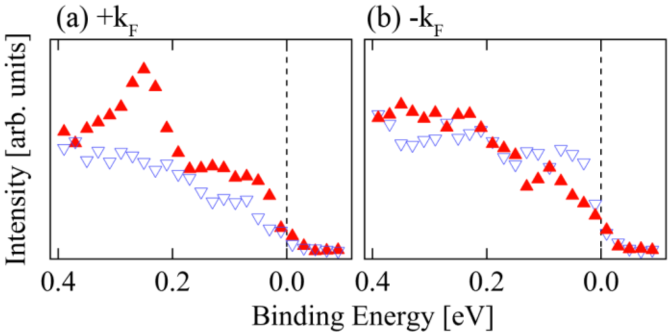

Figure 2. Spin- resolved energy distribution curves along $\overline{\mathrm{Y}}$-$\overline{\mathrm{M}}$ at 14 K. (a) +k_F (k_x = 0.10 Å^{-1}). (b) - k_F (k_x = -0.10 Å^{-1}). The filled (open) triangles correspond to spin polarization parallel (anti-parallel) to [001].

It would be due to the qualitatively common surface atomic structures of Bi/GaSb(110)-(2×1) and Bi/InAs(110)-(2×1), the “missing – row” model with the zig-zag Bi chains [7, 8].

Figures 2 shows the spin-resoled energy distribution curves (EDCs) at the Fermi wavevector (k_F) along $\overline{\mathrm{Y}}$-$\overline{\mathrm{M}}$ taken by SARPES. The spin-polarized peaks in Fig. 2 were clearly observed around E_F. These peak positions are consistent with the band dispersions in Fig. 1 (b). The spin polarization of these peaks inverts together with the signs of the wavenumbers, indicating the time-reversal symmetry, consistent with the Rashba-type spin-splitting.

These results suggest that Bi/GaSb(110)-(2×1) surface is the good Q1D candidate for following researches of spin-dependent phenomena, hosting a metallic and widely spin split surface states in Q1D.

REFERENCES

[1] É. I. Rashba, Sov. Phys.-Solid State **2**, 1109 (1960).
[2] M. Z. Hasan and C. L. Kane, Rev. Mod. Phys. **82**, 3045 (2010).
[3] A. Manchon *et al.*, Nature Mat. **14**, 871 (2015).
[4] B. Braunecker *et al.*, Phys. Rev. B **82**, 045127 (2010).
[5] V. Mourik *et al.*, Science **336**, 1003 (2012).
[6] T. Nakamura *et al.*, Phys. Rev. B **98**, 075431 (2018).
[7] M. G. Betti *et al.*, Phys. Rev. B **59**, 15760 (1999).
[8] S. C. A. Gay and G. P. Srivastava, Phys. Rev. B **61**, 2688 (2000)

MODIFICATION OF SURFACE STATE OF TOPOLOGICAL INSULATOR $\mathbf{Bi_2Se_3}$ BY ADSORPTION OF ORGANIC DONOR MOLECULE TTN

T. Kitazawa, K. Shimozawa, and Shin groups

Department of Physics, Faculty of Science and Technology, Tokyo University of Science

Synchrotron Radiation Laboratory, The Institute for Solid State Physics, The University of Tokyo

Topological Insulators (TI), whose surface states provide various exotic quantum phenomena, attract much attention in quantum matter physics. TI surface states (TSS) have a helical-spin texture and in which spin-locked electrons are topologically protected from back scattering due to the time reversal symmetry attributed by strong spin-orbital coupling. The spintronic devices taking advantage of TI features are now expected to be realized. Thus, controlling the TSS by creating interfaces between TI and other materials is an important problem for applying TIs for spintronics devices. Recently, many researchers have worked on the TI interface with another material [1]. However, few previous researches related to the TI interface with organic materials have been reported [2].

In our research, we aimed to control the TSS of $\mathrm{Bi_2Se_3(111)}$ surface, where a single Dirac Cone is located at the $\bar{\Gamma}$ point in SBZ, by adsorption of organic donor molecule TTN (Tetrathianaphthacene) onto the TI surface. To this end, we performed ARPES measurement by using angle-resolved photoelectron spectroscopy (ARPES) machine at the Laser and Synchrotron Research Center in the ISSP and studied the thickness dependence of TSS. The experiment was carried out at 140K using s-polarized VUV laser ($h\nu = 6.994\ \mathrm{eV}$) under ultrahigh vacuum conditions ($\sim 1 \times 10^{-8}$ Pa). The TTN molecule was deposited using Knudsen cell evaporator. The thickness of the molecule layer was estimated by using a quartz-crystal microbalance. The deposition process was performed in situ and at room temperature.

The experimental results are shown in Figure 1. The $\mathrm{Bi_2Se_3}$ single crystal synthesized by Yaguchi group in Tokyo University of Science shows clear Dirac Cone dispersion on its pristine (111) surface, where DP is located at $E - E_\mathrm{F} = -0.27$ eV. After TTN deposition of ~5Å, the TSS electronic structure changes dramatically. The DP shifts to higher binding energy ($E - E_\mathrm{F} = -0.39$ eV) and the Fermi surface area increases as the circular contour shape turns into the hexagonal warped one [3,4]. At the same time, the bulk conduction band (BCB) state appears inside the TSS with the clear band bottom edge. It appears that n-type doping due to the adsorption of TTN increases the density of surface electrons and consequently leads fermi level to move into the BCB (away from the DP). Moreover, it is speculated that the surface electrostatic potential is perturbed by n-type doping, which causes triangle-like downward band-bending of the bulk electronic bands close to the surface. We interpret the clear BCB bottom edge as an intensity of the electrons weakly localized near the surface.

At further TTN deposition of $10\mathrm{Å}$, the DP shifts to higher binding energy ($E - E_\mathrm{F} \approx -0.55$ eV) and Femi surface area gets larger, which means the TSS is further n-doped by TTN deposition. Besides, we observe the parabolic dispersion attributed to the BCB inside the TSS. This indicates that the relatively strong downward band-bending occurs at the TTN/$\mathrm{Bi_2Se_3}$ interface where the electrons are accumulated in the potential well forming a two-dimensional electron gas (2DEG) [5,6]. The flat feature lying in the lower energy region is attributed to the HOMO state of TTN. For the TTN deposition of $20\mathrm{Å}$, the electronic structure is virtually unchanged compared to $10\mathrm{Å}$ deposition. It is assumed that the TTN molecular layer achieved 1ML under the $10\mathrm{Å}$ thickness.

We need to perform other experiments to verify whether the charge transfer from TTN to $\mathrm{Bi_2Se_3}$ surface occurs or not and establish the adsorption structure.

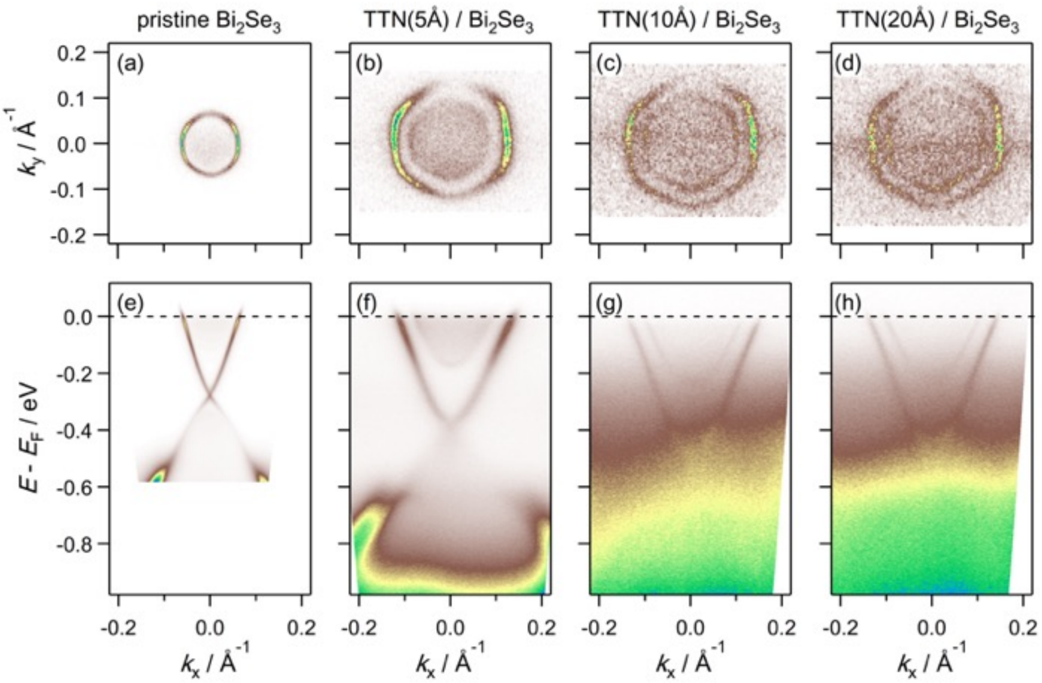

Figure 1. Measured ARPES spectra and Fermi surface maps for (a and e) pristine Bi_2Se_3, (b and f) TTN(5Å)/Bi_2Se_3, (c and g) TTN(10Å)/Bi_2Se_3, (d and h) TTN(20Å)/Bi_2Se_3 at 140K.

REFERENCES

[1] L. Wray *et al*, *Nature Physics*, **7**, 32-37(2011).
[2] J. Wang *et al*, *Journal of Physical Chemistry C*, **118**, 14860-14865(2014).
[3] L. Fu *et al*, *Phys. Rev. Lett.*, **103**, 266801(2009)
[4] K. Kuroda *et al*, *Phys. Rev. Lett.*, **105**, 076802(2010)
[5] M.S. Bahramy *et al*, *Nat. Commun.*, **3**, 1159(2012)
[6] M. Bianchi *et al*, *Nat. Commun.*, **1**, 128(2010)

AUTHORS

T. Kitazawa[a], K. Shimozawa[a], K. Yaji[b], Y. Ishida[b], K. Kuroda[b], A. Harasawa[b], H. Kondo[a], T. Yamanaka[a], H. Yaguchi[a], K. Mase[c], S. Shin[b], K. Akaike[d], K. Kanai[a]

[a]Tokyo University of Science
[b]ISSP
[c]KEK
[d]AIST

INVESTIGATION OF TOPOLOGICAL PROPERTIES IN SUPERCONDUCTING TASE3

Chun Lin[1], Ryo Noguchi[1], Kenta Kuroda[1], Peng Zhang[1], Shunsuke Sakuragi[1], Jiadi Xu[1],
Koichiro Yaji[1], Ayumi Harasawa[1], Shik Shin[1], Atsushi Nomura[2], Masahito Sakoda[3],
Masakatsu Tsubota[4], Satoshi Tanda[3], and Takeshi Kondo[1]

[1]*The Institute for Solid State Physics, The University of Tokyo*

[2]*Department of Physics, Tokyo University of Science*

[3]*Department of Applied Physics, Hokkaido University*

[4]*Department. of Physics, Gakushuin University*

Topological insulators (TIs), which are characterized by the fully gapped bulk states but gapless surface states [1], have attracted a lot of attentions in recent years. Moreover, the proposed topological superconductors [2], in which the Majorana states emerge within the superconducting gap, further boost the progress in this area owing to the potential applications in topological quantum computation. The attractive charge density waves (CDW) in transition-metal trichalcogenides MX_3 (M: Nb, Ta; X: S, Se) with layered quasi-1D chain-like structures [Fig. 1 (a)] have been extensively discussed in the early ages [3]. As one exception, $TaSe_3$ is appealing in that superconductivity emerges at ultra-low temperatures [4], differently from other analogues which undergo multiple CDW transitions [3]. It is considered that the anomaly stems from the poor nesting conditions in $TaSe_3$ due to more 3D electronic structures and competing CDW can be induced by Cu doping or in mesowires which reduce the dimensionality, as shown in Fig. 1 (b) [4-6]. Nevertheless, direct demonstrations of the electronic structures are still deficient. More interestingly, the recent first-principle calculations indicate that $TaSe_3$ actually belongs to a strong TI phase and moreover predict intriguing topological phase transitions among weak TI, strong TI, Dirac semimetal, and normal insulator phases through uniaxial strains, as shown in Fig. 1 (c) [7]. $TaSe_3$ thus not only offers a simple system to study the interplay between superconductivity and topological surface states (TSSs), but also provides an ideal platform for investigating topological phase transitions. A direct probing of the electronic structures via angle-resolved photoemission spectroscopy (ARPES) is consequently needed to elucidate the novel topological properties. So far, to our knowledge, there is only one direct measurement of the electronic structure of $TaSe_3$ by ARPES presenting blurred and inconclusive dispersions due to weak intensity and modest energy resolution [8].

In order to clearly reveal the electronic structure of $TaSe_3$ and confirm its topological properties [7], we have performed high-resolution laser spin-resolved ARPES measurements at the Institute for Solid State Physics, the University of Tokyo [9].

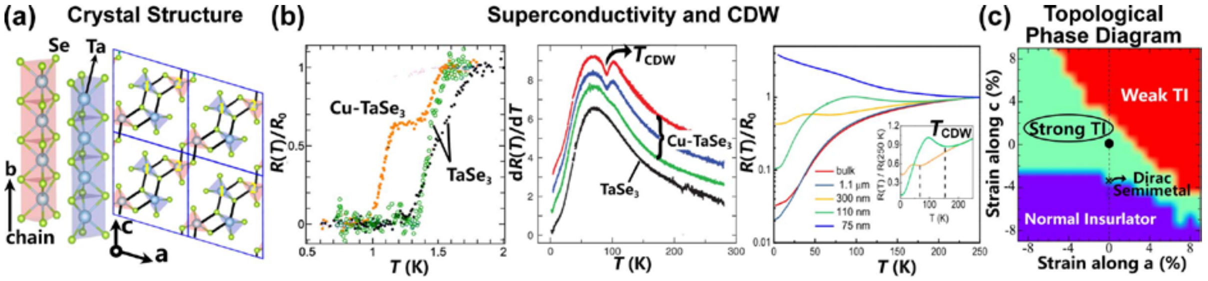

Fig. 1 (a) Crystal structure and unit cell of $TaSe_3$ [7]. (b) Superconductivity in pure and Cu-doped $TaSe_3$ (left) [4], CDW signature in Cu-doped $TaSe_3$ (middle) [5], and direct observation of CDW in mesowire $TaSe_3$ (right) [6]. (c) Strain-induced topological phase diagram of $TaSe_3$ including strong topological insulator (TI), weak TI, Dirac semimetal, and normal insulator phases [7].

For comparison with the calculation [7], Figure 2 (a) shows the 3D Brillouin zone and theoretical Fermi surface of $TaSe_3$, followed by the calculated TSSs at Γ and X points on (-101) surface in Fig. 2 (b). Figure (c) is schematic of the experimental ARPES setup [9] and typical sample size. In Fig. 2 (d) – (f), we show the observed Fermi surface and dispersions at Γ and X points on (-101) surface obtained using 7 eV laser at 10 K. Obviously, the observed band structure is in good agreement with the calculations shown in Fig. 2 (b) [7]. Figure 2 (g) shows one typical spin-revolved result at the cut on the sharp low-energy excitations indicated in Fig. 2 (f) by the dash line. One could clearly resolve the distinct signals from spin up and down states. Spin polarization [9] up to 30% has been detected in the low-energy excitations, which are possibly the TSSs.

In conclusion, we have performed laser spin-ARPES measurements on $TaSe_3$, the clearly resolved low-energy electronic structure qualitatively agrees with the calculated TSSs. The observation of spin polarization further implies that the sharp low-energy excitations are probably TSSs.

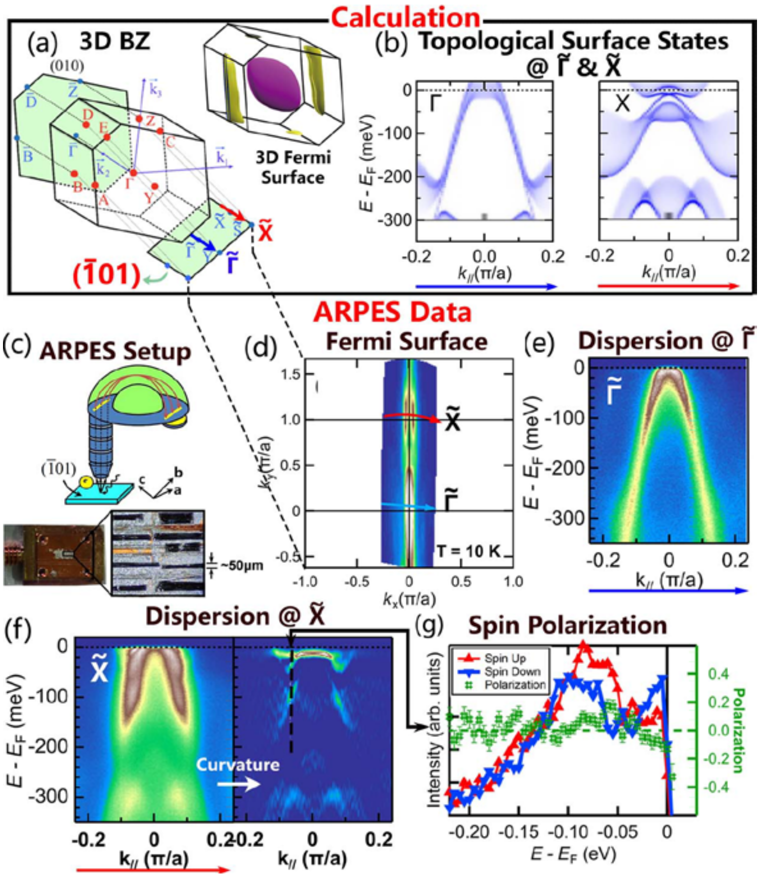

Fig. 2 (a) 3D Brillouin zone and calculated 3D Fermi surface of $TaSe_3$ [7]. (b) Calculated topological surface states at Γ and X points on (-101) surface [7]. Momentum cut positions are indicated in (a) with blue and red arrows, respectively. (c) ARPES setup. Typical samples size is ~ 1×0.1×0.01 mm. (d) Observed Fermi surface on (-101) surface at 10 K. Γ and X points are indicated by blue and red arrows, respectively. (e) Corresponding dispersion at Γ point. (f) Dispersion at X point and its curvature plot enhancing intensity maxima [10]. (g) Spin polarization along X direction at the cut indicated in (f) by a dash line. Red and blue curves are EDCs of spin up and down states, respectively. Up to 30 % spin polarization is detected

REFERENCES

[1] X.-L. Qi, S.-C. Zhang, Rev. Mod. Phys. **83**, 1057–1110 (2011).
[2] L. Fu and C. L. Kane, Phys. Rev. Lett. **100**, 096407 (2008).
[3] P. Monceau, Adv. Phys. **61**, 325–581 (2012).
[4] A. Nomura, et al., EPL. **124**, 67001 (2019).
[5] A. Nomura et al., EPL. **119**, 17005 (2017).
[6] J. Yang et al., ArXiv190609527 Cond-Mat (2019).
[7] S. Nie et al., Phys. Rev. B. **98**, 125143 (2018).
[8] A. Perucchi et al., Eur. Phys. J. B. **39**, 433–440 (2004).
[9] K. Yaji et al., Rev. Sci. Instrum. **87**, 053111 (2016).
[10] P. Zhang et al., Rev. Sci. Instrum. 82, 043712 (2011).

Observation of the interface state for Bi layer deposited on a MnGa thin film

M. Kobayashi[1,2], T. Takeda[2], N. H. D. Khang[3], M. Suzuki[4], A. Fujimori[4],
K. Kuroda[5], K. Yaji[5], S. Shin[5], M. Tanaka[1,2] and P. N. Hai[3]
[1]*Center for Spintronic Research Network, The University of Tokyo,*
[2]*Department of Electrical Engineering and Information Systems, The University of Tokyo*
[3]*Department of Electrical and Electronic Engineering, Tokyo Institute of Technology*
[4]*Department of Physics, The University of Tokyo*
[5]*Laser and Synchrotron Research Center, The Institute for Solid State Physics, The University of Tokyo*

Spin-orbit torque switching using the spin Hall effect has attracted much attention due to its potential application for ultra-high speed magnetoresistive random-access memories. Recently, spin-orbit torque switching using topological insulator $Bi_{1-x}Sb_x$ (BiSb) (x = 0.1) has been successfully developed [1]. Here, the BiSb(012) layer as a spin current source is grown on perpendicular ferromagnet $Mn_{0.6}Ga_{0.4}$ (MnGa) by molecular beam epitaxy (MBE) method. Since the topological state on the BiSb(012) surface has colossal spin Hall angle and high electric conductivity [1], the spin Hall conductivity of BiSb(012) is higher than that of conventional heavy metals [2-4] and other topological insulators [5]. Actually, the BiSb/MnGa heterostructure has demonstrated magnetization reversal via spin-orbit torque with extra-low current density that is one to two orders of magnitude lower than the current for conventional magnetization reversal. From comparison of spin Hall angles between the BiSb(001) and (012) surfaces, the number of Dirac cones (DCs) crossing the Fermi level (E_F), which is considered to contribute to the large spin Hall effect, in the (012) surface is larger than that in the (001) surface [6].

To understand the origin of the colossal spin Hall angle in topological insulators and ferromagnets, the band structure including the topological surface state of the BiSb/MnGa heterostructure has to be investigated. Therefore, we have performed spin- and angle-resolved photoemission spectroscopy (SARPES) measurements on a Bi/MnGa heterostructure.

A MnGa thin film was grown on a GaAs(001) substrate by the MBE method. The film was capped by amorphous Se layer to protect the surface from oxidization. Details of the film growth are described elsewhere [1]. The film was annealed at 550 °C under ultra-high vacuum better than 10^{-7} Pa to remove the Se capping layer. Bi layer was deposited on the clean MnGa surface at 150 °C with the thickness of about 1 bilayer. Clean surfaces of the thin films before and after Bi deposition were confirmed by low-energy electron-diffraction (LEED) measurements. ARPES with He-I (21.2 eV) and He-II (40.8 eV) light sources and 7eV-laser-based spin- and angle-resolved photoemission spectroscopy (Laser-SARPES) measurements were conducted with the ARPES instrument using DA-30 photoemission analyzer equipped with VLEED spin detector (Scienta Omicron, Inc.) at ISSP, University of Tokyo [7]. The measurements were performed at 30 K in a base pressure below 10^{-9} Pa. The polarization of the laser was linear-horizontal.

Figure 1(a) shows an angle-integrated photoemission spectrum of the Bi/MnGa thin film measured with the He-II source. The core-level peaks of Bi 5*d* (binding energy $E_B \sim 25$ eV) from the deposited Bi layer and Ga 3*d* ($E_B \sim 18$ eV) from the MnGa underlayer are observed. Since the thickness of the Bi layer is not large, photoemission signals from the MnGa layer are also detected. Figure 1(b) shows ARPES spectra along the Γ-X symmetry line of the Bi(012)/MnGa thin film taken with the He-I light source. The concave band around $E_B = 0.1\sim 0.5$ eV centered at the Γ point originates from the MnGa underlayer. Since the hole-like band crossing E_F near the Γ point appears after the Bi deposition, this band near the Γ point comes from the Bi layer.

The hole-like band near the Γ point has been investigated using Laser-SARPES. Figure 2(a) shows the ARPES spectrum along the Γ-X line taken with the 7-eV laser. While the band dispersion is unclear with the He-I source, the sharp dispersion can be seen near the Γ point in the Laser-ARPES spectrum due to the higher energy and momentum resolution. The dispersion of this band looks linear, as shown in Fig. 2(b). The SARPES measurements have revealed that the sharp band is spin-polarized along the direction perpendicular to the Γ-X line and the spin polarization is flipped with the momentum direction, as shown in Fig. 2(c). Based on the observations, the band near the Γ point is expected to be the DC state of the deposited Bi layer. Therefore, we have succeeded in observing the topological interface state between the Bi and MnGa layers using Laser-SARPES. Further electronic structure study such as the observations of the entire band structure and DC states near the Brillouin zone boundary will shed light on the origin of the large spin Hall angle of the interface between the topological insulator/ferromagnet heterostructures.

References

[1] N. H. D. Khang *et al.*, Nat. Mater. **17**, 808 (2018).
[2] L. Liu *et al.*, Science **336**, 555 (2012).
[3] C.-F. Pai *et al.*, Appl. Phys. Lett. **101**, 122404 (2012).
[4] L. Liu *et al.*, Phys. Rev. Lett. **106**, 036601 (2011).
[5] A. R. Melnik *et al.*, Nature **511**, 449 (2014).
[6] X.-G. Zhu *et al.*, New J. Phys. **15**, 103011 (2013).
[7] K. Yaji *et al.*, Rev. Sci. Instrum. **87**, 053111 (2016).

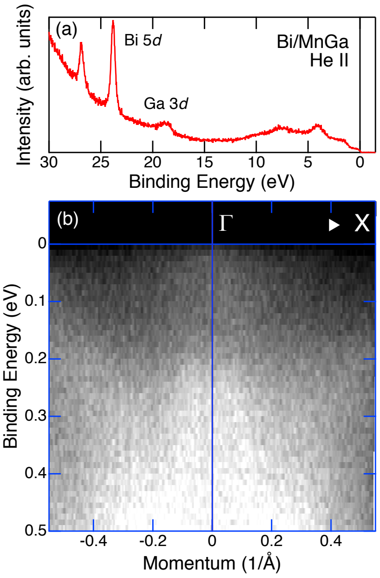

Fig.1. Photoemission spectra of Bi/MnGa thin film. (a) Angle-integrated spectrum taken with the He-II source. (b) ARPES spectrum along the Γ-X line taken with the He-I source.

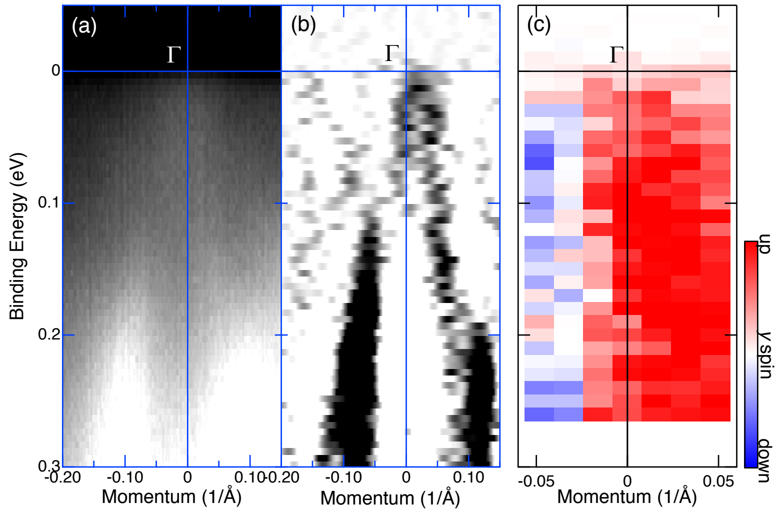

Fig.2. Laser-SARPES spectra of Bi/MnGa thin film. (a) ARPES spectrum along the Γ-X line taken with the 7-eV laser. (b) 2nd derivative ARPES spectrum. The derivation has been performed along the momentum direction. (c) SARPES spectrum. The spin direction is perpendicular to the Γ-X direction (*y* spin).

SWITCHABLE WEAK TOPOLOGICAL INSULATOR STATE IN QUASI-ONE-DIMENSIONAL BISMUTH IODIDE

R. Noguchi,[1] T. Takahashi,[2] K. Kuroda,[1] K. Yaji,[1] A. Harasawa,[1]
S. Shin,[1] T. Sasagawa,[2] T. Kondo[1]
[1]ISSP, University of Tokyo, [2]MSL, Tokyo Institute of Technology

A topological insulator (TI) is characterized by an insulating bulk with conductive edges determined by Z_2 topological invariants. In three dimensions, a TI is classified as either a strong TI (STI) or a weak TI (WTI) [1], and the STI phase was experimentally confirmed rapidly after the theoretical predictions through the observation of topological surface states (TSS) by angle-resolved photoemission spectroscopy (ARPES) [2]. In contrast, the WTI phase has so far eluded experimental verification, since TSSs emerge only on side surfaces, which are typically not cleavable and undetectable in real 3D crystals. In this work, we have investigated the WTI state in β-Bi$_4$I$_4$ with naturally cleavable top and side planes, which is necessary for the experimental confirmation of the WTI state.

β-Bi$_4$I$_4$ is predicted to be in proximity of three different topological phase by theoretical calculations: a STI (1;110) a WTI (0;001) or a normal insulator (0;000) phase is realized sensitively depending on the calculation parameters [3, 4]. By using laser-SARPES, we have demonstrated that a spin-polarized quasi-1D TSS exist in the bulk band gap of β-Bi$_4$I$_4$, indicating the WTI phase in the real crystal. In contrast, α-Bi$_4$I$_4$ is predicted to be topologically trivial and no TSS has been detected by ARPES in this compound. From these results, we expect that the phase transition between the WTI phase and the normal insulator phase occurs following the structural transition between the β-phase and the α-phase. However, one may wonder (i) why the observed Fermi surface shown in fig. 1(b) is quite anisotropic along k_y and (ii) whether the topological phase transition really happens in single crystal piece. Here, we discuss these points by using laser-(S)ARPES [5].

First, we investigated the photoemission intensity distribution of the topological surface states on the side surface by conducting light-polarization dependent ARPES. The experimental geometry for the ARPES measurements is shown in Fig. 1(a), where θ is the measurement angle for each ARPES image. With p-polarized light, the photoemission intensity distribution is clearly anisotropic both at the $\bar{\Gamma}$ point and the $\bar{Z}$ point of the (100) surface Brillouin zone as shown in Fig. 1(c) and 1(e), where one branch of the Dirac dispersion ($-k_F$) is clearly observed while the photoemission intensity of the other part ($+k_F$) is almost vanishing. In contrast, with s-polarized light, the photoemission intensities from both branches are almost the same as shown in Fig. 1(d) and 1(f). These results can be explained by the interference of photoemission

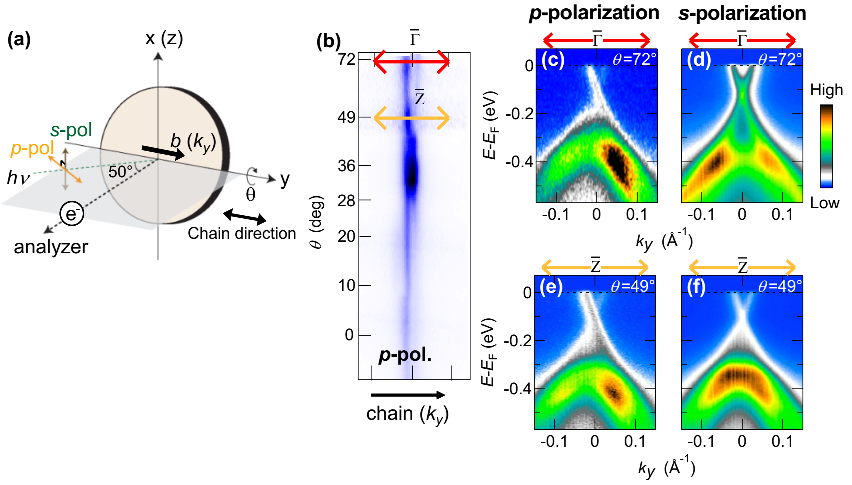

Fig. 1 (a) Experimental geometry of laser-ARPES. **(b)** The Fermi surface mapping obtained with p-polarized light. **(c, d)** ARPES band maps across the $\bar{\Gamma}$ point of the (100) surface taken with p-polarized light and s-polarized light, respectively. **(e, f)** Same as (c) and (d), but for the momentum cut across $\bar{Z}$ point of the (100) surface.

processes. Since the p-pol. light has both of in-plane and out-of-plane components [Fig. 1(a)], it excites electrons with different orbitals at the same time if the TSS is composed of multiple orbitals. Generally, TSS consists in Bi-based topological insulators of Bi $6p_{x,y,z}$ orbitals due to the strong spin-orbit coupling of bismuth [6], and hence the observed photoemission intensity anisotropy is attributed to the result from the interference of photoelectrons from Bi $6p_y$ (in-plane) and $6p_x$ (out-of-plane) orbitals excited by p-pol. light. In the case of ARPES with s-pol. light, the interference effect becomes smaller because s-pol. light has smaller out-of-plane component and excites only Bi $6p_x$ orbital.

Second, we show that the topological phase transition between the WTI phase and normal insulator phase follows the structural phase transition between β- and α-Bi_4I_4, and thus the topological phase is switchable in this material. The procedure for demonstrating the phase transition in single piece of Bi_4I_4 crystal is shown in Fig. 2(a) and 2(d). To unambiguously investigate the effect of the structural transition, the same crystal pieces have been cleaved twice after mild cooling and after rapid cooling. As shown in the ARPES images, quasi-1D TSS observed after rapid cooling [Fig. 2(b)] disappeared after mild cooling [Fig. 2(c)], showing the phase transition from the WTI phase to the normal insulator phase. In addition, the band gap observed after mild cooling [Fig. 2(e)] was gapped with the appearance of TSS after quenching [Fig. 2(f)], reflecting the phase transition from the normal insulator phase to the WTI phase. From these results, it is concluded that the topological phase transition in fact follows the structural phase transition and hence the topological phase in Bi_4I_4 can be controlled by temperature.

In conclusion, these results support the switchable WTI phase in Bi_4I_4 observed in our previous measurements. Since the bulk of Bi_4I_4 is insulating, the TSSs can be probed not only by ARPES but also by transport measurements. Importantly, the capability of controlling the topological phase using structural phase transition is beneficial to making devices such as spin-transistor. Our work will thus stimulate further in-depth study on exotic properties of the WTI state and put the foundation for future WTI-based spintronic applications.

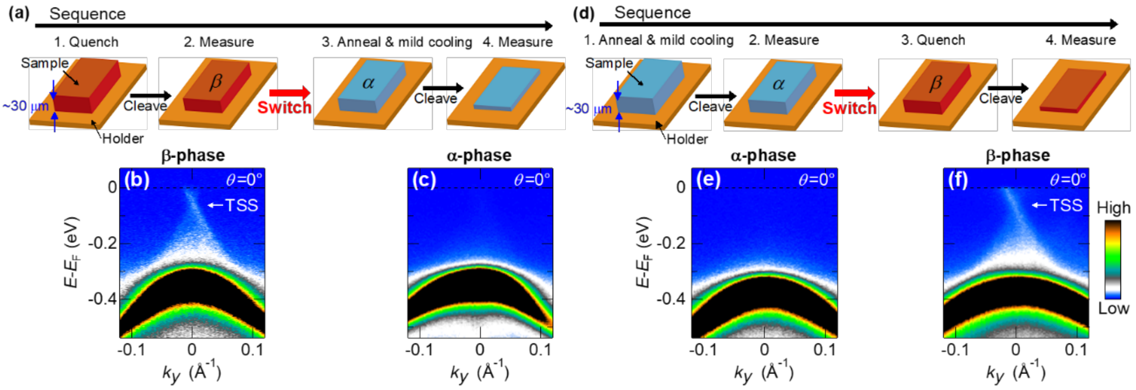

Fig. 2 **(a)** Experimental sequence to demonstrate the topological phase transition following the structural phase transition from the β-phase to the α-phase using the same crystal piece. **(b, c)** ARPES images at θ=0° after quenching (b) and after mild cooling (c) for the same crystal piece. **(d)** Same as (a), but from the α-phase to the β-phase. **(e, f)** ARPES images at θ=0° after mild cooling (e) and after quenching (f) for the same crystal piece.

REFERENCES

[1] L. Fu, C. L. Kane, and E. J. Mele, Phys. Rev. Lett., **98**, s106803 (2007).
[2] Y. Xia *et al.*, Nat. Phys. **5**, 398 (2009).
[3] G. Autès *et al.*, Nat. Mater. **15**, 154 (2015).
[4] C.-C. Liu *et al.*, Phys. Rev. Lett. **116**, 66801 (2016).
[5] R. Noguchi *et al.*, Nature **566**, 518 (2019).
[6] H. Zhang, C.-X. Liu, and S.-C. Zhang, Phys. Rev. Lett. **111**, 066801 (2013).

Electronic and spin structure of heavy element thallium single crystal thin films

Yoshitaka Nakata[1], Takahiro Kobayashi[1], Koichiro Yaji[2], Kazuyuki Sakamoto[1,3,4]

[1]*Department of Materials Science, Chiba University*
[2]*Institute for Solid State Physics, the University of Tokyo, Kashiwa*
[3]*Molecular Chirality Research Center, Chiba University*
[4]*Department of Material and Life Science, Osaka University*

Introduction

In solid bulk, the two bands with opposite spins are usually degenerated due to the presence of both the time-reversal and space-inversion symmetries. However, in case of surface or interface, where the space-inversion symmetry is broken, the spin degeneracy is lifted by the spin-orbit coupling (SOC). This is called the Bychkov-Rashba effect or simply the Rashba effect [1]. In the early studies, the observation of giant Rashba effects on surface alloys formed by the adsorption of 1/3 ML of high-Z elements Bi or Pb on the Ag(111) surface [2,3] has attracted a lot of interest. The spin-split was discussed based on a simple Rashba effect in these studies. More recently, several peculiar Rashba spins have been observed, and their origins were discussed based on e.g., the symmetry of the surface [4]. Tl atomic layers formed on Si surfaces are one of such exotic systems. Together with this interesting spin-related phenomenon, Tl is also known to exhibit superconductivity at below 2.4 K in crystal phase [5]. However, due to the difficulty to create a single Tl crystal that is large enough to perform photoemission measurements, there is no experimental report on its band structure so far. Moreover, since a Tl single crystal film would show spin-split bands and thus has the possibility of becoming a topological superconductor [6], we planned to create a Tl single crystal film and measure its band structure.

Experimental details

The Ag(111) surface was first sputtered with Ar^+ with an accelerating voltage of 500 V in high vacuum ($5x10^{-3}$ Pa) to obtain a clean surface. The quality of the Ag(111) surface was confirmed by the observation of sharp LEED spots and a clear surface state. The Tl single crystal film was then prepared by the deposition of 2 ML of Tl on the Ag(111) clean surface. The LEED pattern of the Tl/Ag(111) surface is shown in Fig. 1. Clear and sharp spots originating from the Tl double-layer single crystal are observed. ARPES and SARPES were performed using the laser-SARPES machine developed at ISSP [7]. All PES measurement was carried out at a sample temperature of 35 K under ultra-high vacuum (ca.1×10^{-8} Pa).

Results and discussion

As shown in Fig. 1, Tl double-layer single crystal thin film has two domains that are rotated ± 4° from the symmetric axis of Ag(111). This make the fermi surface and band structure complicated as shown in Figs. 2 (a) and (b). By considering the number of surface states observed in the band dispersion along the $\bar{\Gamma} - \bar{K}_{\mathrm{Ag}}$ direction, we found that the Tl single crystal film has two metallic bands (as shown in Fig. 2 (a) the bands of Tl are degenerated in the $\bar{\Gamma} - \bar{K}_{\mathrm{Ag}}$ direction). Of the two metallic bands, the one with lower binding energy at the $\bar{K}$ point of the Tl Brillouin zone shows a clear split in the energy direction. In order to investigate the origin of this splitting, we performed SARPES measurement, and found that the split at the $\bar{K}$ point is a spin split, and the spin-polarization vector point along the wave vector directions. This means that the origin of this spin-split is not an ordinary Rashba effect, and we are now tackling this problem by considering other possible origins.

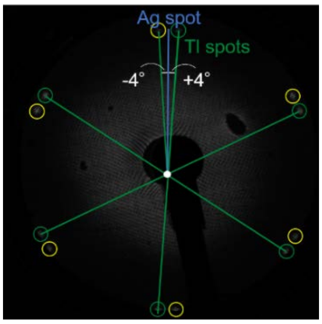

Fig. 1 LEED pattern of Tl/Ag(111) obtained with an electron energy of 85 eV.

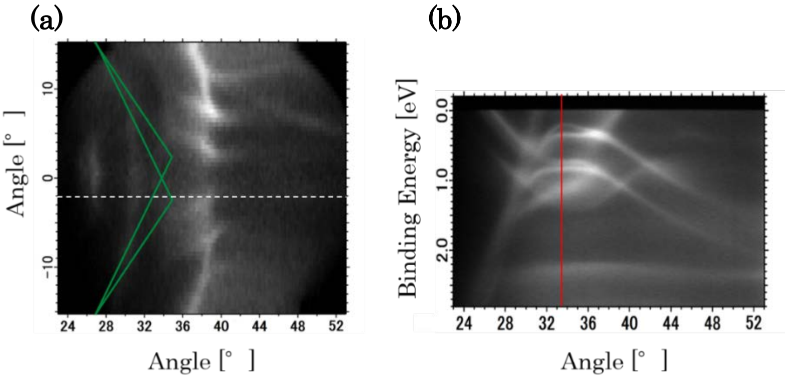

Fig. 2 (a) Fermi surface around the $\bar{K}$ point of the Brillouin zone of Tl. Green lines indicate the Brillouin zones of Tl from the two domains. (b) Band structure cut at the white dashed line in (a).

Summary

We obtained a Tl double-layer single crystal film on a Ag(111) surface that is large enough to measure its band structure. The presence of two metallic bands and a split of one of them at the $\bar{K}$ point of the Tl Brillouin zone was confirmed by ARPES. This split is a spin-split, and the spin-polarization vector point along the wave vector directions.

References

[1] Y. A. Bychkov and E. I. Rashba, JETP Lett. **39**, 78 (1984).
[2] C. R. Ast *et al.*, Phys. Rev. Lett. **98**, 186807 (2007).
[3] F. Meier, H. Dil, J. Lobo-Checa, L. Patthey, and J. Osterwalder, Phys. Rev. B **77**, 165431 (2008).
[4] for example, E. Annese *et al.*, Phys. Rev. Lett. **117**, 016803 (2016).
[5] T. Imamura, K. Okamoto, M. Saito, and M. Ohtsuka. J. Phys. Soc. Jpn, **40**, 1256 (1976).
[6] J. D. Sau *et al.*, Phys. Rev. Lett. **104**, 040502 (2010).
[7] K. Yaji *et al.*, Rev. Sci. Instrum., **87**, 053111 (2016).

SPIN-POLARIZED BANDS OF AN IN BYLAYER FILM FORMED ON Si(111)

Takahiro Kobayashi[1], Yoshitaka Nakata[1], Koichiro Yaji[2], Shunsuke Yoshizawa[4], Fumio Komori[2], Shik Shin[2], Takashi Uchihashi[3], Kazuyuki Sakamoto[1,4,5]

[1]*Department of Materials Science, Chiba University*
[2]*The Institute for Solid State Physics, the University of Tokyo*
[3]*National Insutitute for Materials Science*
[4]*Molecular Chirality Research Center, Chiba University*
[5]*Department of Material and Life Science, Osaka University*

Introduction

In two-dimensional (2D) systems such as surfaces or heterointerfaces, the electron bands are split due to spin-orbit coupling and the space inversion asymmetry along the direction perpendicular to the plane. This effect is called the Rashba effect [1], which leads the spin-polarization vectors to be parallel to the 2D plane and perpendicular to the wave vector in an ideal 2D system. This Rashba effect was observed on the surface of heavy elements [2], heavy element atomic layers formed on solid surfaces [3] and so on. One of the main motivations of these early studies was to create a system with large Rashba splitting that can be used as a material for spintronics devices. In this project, motivated by the theoretical work reported by Sau *et al.* [4], we focus on the spin-polarized band induced in such atomic layers that has potential to become topological superconductor. The system that we studied is the In/Si (111)-($\sqrt{7} \times \sqrt{3}$) surface, a system that is formed by the adsorption of 2.4 ML of In ontop of Si(111) [5] and shows superconductivity below ca. 3 K [6].

Experimental details

Angle-resolved photoelectron spectroscopy (ARPES) and spin-resolved ARPES (SARPES) measurements were performed with the laser-SARPES machine developed at ISSP [7]. A laser light source with a photon energy ($h\nu$) of 6.994 eV was used as the excitation light, and a Scienta Omicron DA30-L analyzer equipped with a VLEED spin detector was used for PES measurements. An n-type doped Si(111) wafer with a resistivity of < 0.01Ω•cm was first annealed at 1520 K to obtain a clean Si(111)-(7×7) surface. Following the adsorption of slightly more than 2.4 ML of In, the sample was annealed at 570 K to obtain the In/Si (111)-($\sqrt{7} \times \sqrt{3}$) surface. The quality of the sample and the presence of a single ($\sqrt{7} \times \sqrt{3}$) domain was confirmed by low-energy electron diffraction (LEED) (Fig. 1) and the observation of clear surface states. All PES measurement was carried out at a sample temperature of 35 K under ultra-high vacuum (ca.1×10^{-8} Pa).

Results and discussion

By using ARPES, we observed a circular Fermi surface together with a butterfly shape one. Although these Fermi surfaces shows good agreement with those reported previously on In/Si (111)-($\sqrt{7} \times \sqrt{3}$) [8,9], thanks to the high k-resolution of the present setup ($\Delta k = 1.4 \times 10^{-3}$ Å^{-1}), we could observed a clear split as shown in Fig. 2 (note that not only the circular Fermi surface shown in Fig. 2 but also the butterfly shape one shows a clear split). Since this split might originate from the Rashba effect, we have performed SARPES measurements to obtain information about the spin polarization of the split Fermi surfaces. Of the two Fermi surfaces, the spin-polarization vector of the circular one was parallel to the surface and perpendicular to the wave vector. This result indicates that the spin-split of the circular Fermi surface might originate from the Rashba effect. In contrast to the circular Fermi surface, the spin-polarization vector of the butterfly shape Fermi surface was completely different, and cannot be explained by the Rashba effect. The spin-polarization vector of the butterfly shape Fermi surface was parallel to the surface, and also parallel to the wave vector. Since the peculiar spin-polarization vector of the butterfly shape Fermi surface was observed at k point without any symmetry (a k point with symmetry means a point like the Γ point of the Brillouin zone), this cannot be a peculiar spin originated from the symmetry of the surface like those observed in our former studies [10] as well. We are now tackling this problem by considering other possible origins, and hope to get the answer soon.

Summary

By using a high-energy and high-k resolution SARPES system, we succeeded to observe the spin splits Fermi surfaces of In/Si (111)-($\sqrt{7} \times \sqrt{3}$), a system that becomes superconductor at below 3 K. The spin-polarization vector of one of the observed Fermi surfaces cannot be explain by neither a simple Rashba effect nor a symmetry induced peculiar Rashba effect.

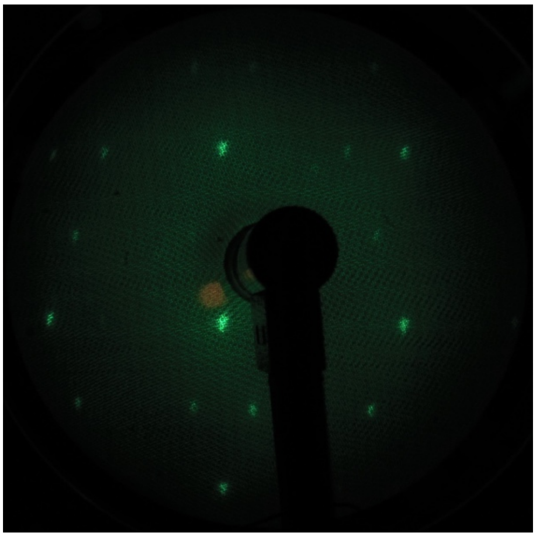

Fig. 1. LEED image of the In/Si (111)-($\sqrt{7} \times \sqrt{3}$) surface obtained with an electron energy of 85 eV.

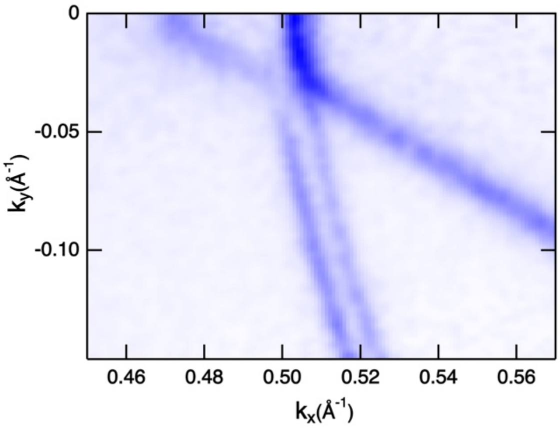

Fig. 2. Fermi surface of In/Si (111)-($\sqrt{7} \times \sqrt{3}$). The circular Fermi surface shows a clear split.

REFERENCES

[1] Y. A. Bychkov and E. I. Rashba, JETP Lett. **39**, 78 (1984).
[2] for example, G. Nicolay, F. Reinert, S. Hüfner, and P. Blaha, Phys. Rev. B **65**, 033407 (2001).
[3] for example, C. R. Ast et al., Phys. Rev. Lett. **98**, 186807 (2007).
[4] J. D. Sau *et al.*, Phys. Rev. Lett. **104**, 040502 (2010).
[5] K. Uchida *et al.*, Phys. Rev. B **87**, 165433 (2013).
[6]T. Uchihashi *et al.*, Phys. Rev. Lett.. **107**, 207001 (2011).
[7] K. Yaji *et al.*, Rev. Sci. Instrum., **87**, 053111 (2016).
[8] E. Rotenberg *et al.*, Phys. Rev. Lett.. **91**, 246404 (2003).
[9] S. Yoshizawa *et al.*, Nano Lett. **17**, 2287 (2017).
[10] for example, K. Sakamoto *et al.*, Phys. Rev. Lett. **102**, 096805 (2009), **117**, 106803 (2016).

MULTIPLE TOPOLOGICAL STATES IN IRON-BASED SUPERCONDUCTORS

Peng Zhang[1], Zhijun Wang[2], Xianxin Wu[3], Koichiro Yaji[1], Yukiaki Ishida[1], Yoshimitsu Kohama[1], Guangyang Dai[4], Yue Sun[1], Cedric Bareille[1], Kenta Kuroda[1], Takeshi Kondo[1], Kozo Okazaki[1], Koichi Kindo[1], Xiancheng Wang[4], Changqing Jin[4], Jiangping Hu[4], Ronny Thomale[3], Kazuki Sumida[6], Shilong Wu[6], Koji Miyamoto[6], Taichi Okuda[6], Hong Ding[4], G. D. Gu[7], Tsuyoshi Tamegai[5], Takuto Kawakami[8], Masatoshi Sato[8] and Shik Shin[1]

[1]Institute for Solid State Physics, University of Tokyo, Kashiwa, Japan. [2]Department of Physics, Princeton University, Princeton, NJ, USA. [3]Theoretical Physics, University of Wurzburg Am Hubland, Wurzburg Germany [4]Institute of Physics, Chinese Academy of Sciences, Beijing, China. [5]Department of Applied Physics, University of Tokyo, Tokyo, Japan. [6]Hiroshima Synchrotron Radiation Center, Hiroshima University, Higashi-Hiroshima, Japan. [7]Brookhaven National Laboratory, Upton, NY, USA. [8]Yukawa Institute for Theoretical Physics, Kyoto University, Kyoto, Japan.

Topological materials and unconventional iron-based superconductors are both important areas of study but, to date, relatively little overlap has been identified between these two fields. However, the combination of topological bands and superconductivity promises the manifestation of exotic superconducting states, including Majorana fermions, the central component of topological quantum computation. Here, using high-resolution spin-resolved ARPES, we have identified both topological insulator (TI) and Dirac semimetal (TDS) states near the Fermi energy in different iron-based superconducting compounds, potentially allowing access to several different superconducting topological states in the same material. These results reveal the generic coexistence of superconductivity and multiple topological states in iron-based superconductors, indicating that this broad class of materials is a promising platform for high-temperature topological superconductivity.

The topological insulator and Dirac semimetal states in Li(Fe,Co)As.

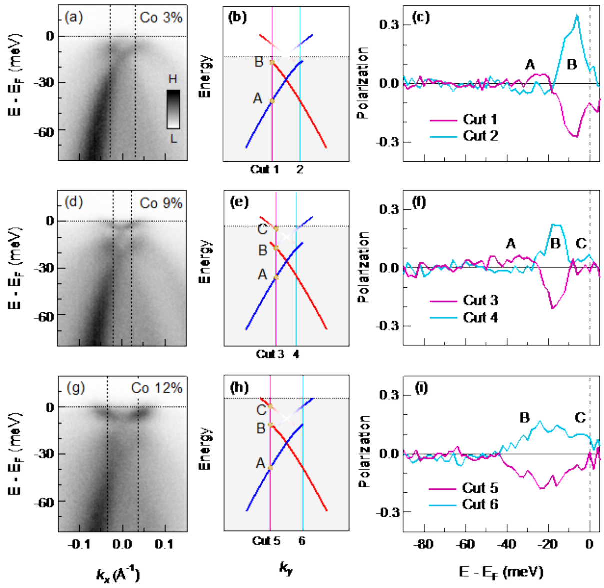

Figure 1 Spin polarization of the Dirac cones from TI and TDS states in Li(Fe$_{1-x}$Co$_x$)As. (a) Intensity plot along k$_x$ for x = 3% sample with a 7-eV laser. (b) Sketch of the spin-polarized surface bands. The blue and red lines stand for opposite spin polarizations, as confirmed by the data in (c). (c) Spin polarization along x direction at Cut 1 and Cut 2, which are indicated by two vertical lines in (a) and (b). (d–f) Same as (a–c), but for samples with x = 9%. (g-i) same as (a–c), but for samples with x = 12%.

We studied a series of Li(Fe,Co)As samples with different Co content by using laser-based ARPES. On the x = 3% samples, only one Dirac band was observed below Fermi level (Fig. 1(a)), similar to the case of Fe(Te,Se) [1,2]. By doping more electrons, we further observed another Dirac cone in the x = 9% and 12% samples, as shown in Fig. 1(d,g), which is above Fermi level in the parent compound. The two Dirac cones are consistent with the DFT calculations: the upper cone comes from the the surface component of the TDS states, while the lower cone comes from the TI surface states. Because of their surface nature, both Dirac cones should be spin-polarized, and the calculated spin patterns are sketched in Fig. 1(b,e,h). We further carried out spin-resolved measurements to check their surface nature. A pair of spin-polarized energy distribution curves along k_y was measured, as indicated in Fig. 1(b,e,h). For both $x = 3\%$ and 9% samples, the spin polarization of the TI Dirac cone is resolved (Fig. 1(c,f)), and consistent with theoretical calculations. For $x = 9\%$ and 12% samples, the spin polarization of the TDS surface cone is observed, as shown in Fig. 1(f,i). Due to the the weak intensity of the upper part of the TDS cone, only the spin polarization of the lower part is resolved.

The topological Dirac semimetal states in Fe(Te,Se).

The TI surface states in Fe(Te,Se) was observed previously in Ref. [2]. The TDS cone in Fe(Te,Se) cannot be resolved directly, because of the difficulty to dope this sample. However, we may obtain some evidences of the TDS bands in Fe(Te,Se) by measuring the associated surface states, as shown in Fig. 2(a). The spin-resolved intensity plots of Fe(Te,Se) are shown in Fig. 2(b). We measured four cuts with high resolution at high symmetry lines, as indicated in Fig. 2(c). Fig. 2(d-g) display the spin polarization curves for the four cuts. The magnitude of spin polarization of the band is about 50%, indicating coexistence of unpolarized bulk and polarized surface states. The results are consistent with the spin-resolved spectrum from calculations in Fig. 2(a), thus support the existence of the TDS states above E_F in Fe(Te,Se).

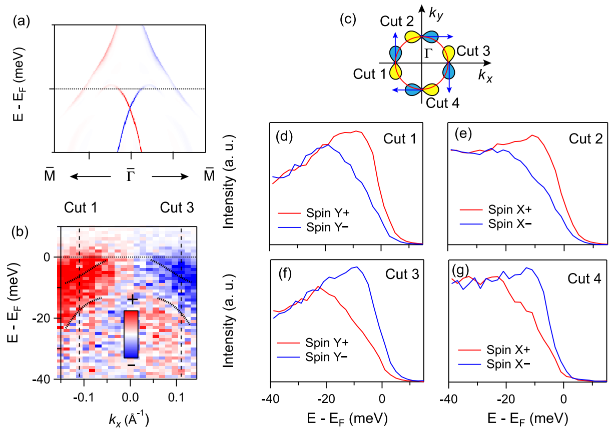

Figure 2 Spin polarization of the band at E_F and its Dirac semimetal origin in Fe(Te,Se). (a) Spin-resolved (001) surface spectrum from a $k{\cdot}p$ model calculation. (b) Spin-resolved intensity plot at Γ with a 7-eV laser. (c) Sketch of the spin-orbit pattern from model calculations. (d-g) Spin-resolved energy distribution curves at Cuts 1–4. Because of the matrix element effect, Cuts 1,3 and 2,4 are taken with *s*-polarized and *p*-polarized photons, respectively.

Our findings of the TI and TDS states in Li(Fe,Co)As and Fe(Te,Se) prove the generic existence of different types of topological states in iron-based superconductors. Their simple structures, multiple topological states, and a tunable Fermi level make iron-based superconductors ideal platforms for the study of topological superconductivity, Majorana bound states, and as such, potentially, topological quantum computation.

References:

[1] Z. Wang et al., Phys. Rev. B 92, 115119 (2015).

[2] P. Zhang et al., Science 360, 182 (2018).

[3] P. Zhang et al., Nature Phys. 15, 41 (2019).

ELECTRONIC BAND STRUCTURE OF TRANSFER GRAPHENE ON SI(111) SUBSTRATE

Koichiro Yaji, Fumio Komori and Shik Shin
Synchrotron Radiation Laboratory, The Institute for Solid State Physics, The University of Tokyo

Electronic band structure of graphene, which has a linear dispersion around a K point, has attracted much attention not only because of fundamental interest but also possible applications of their electronic conduction. The epitaxial graphene has been experimentally made on substrates by several methods so far. For example, the graphene grown on Si-terminated surface of SiC(0001) has been well known and established. In contrast to the former studies, in the present study, we have fabricated the single-layer graphene on a Si(111) substrate by transfer method and have investigated the electronic band structure of the transfer graphene by angle-resolved photoemission spectroscopy (ARPES).

We used monolayer graphene film made for transfer that was commercially available. The Si(111) substrate was cut from a wafer. The transfer procedure was as follows: The sacrificial-layer/graphene was put in deionized water. The Si(111) substrate was introduced into the deionized water and scoop the sacrificial layer/graphene from below. After that the sacrificial-layer/graphene was deposited on the Si(111) substrate [Fig. 1(a)]. Then, the sacrificial layer/graphene/substrate was taken out from the water and let it dry 30 minutes in air. Subsequently, the sample is heated in an oven at 150°C for 1.5h. And then, the sample is stored in a vacuum desiccator for 24h to avoid detachment of the graphene from the substrate. The sacrificial layer is removed in acetone for 1h, and then the sample is put into ethanol for 1h. After this procedure, the sample was introduced into the UHV chamber. And then, the sample were annealed at 400C for 30 min. The surface quality was checked by low energy electron diffraction, where we observed a ring pattern due to the multi domain structure of the transfer graphene. Here, the average size of one domain is approximately several micrometers.

ARPES measurements were performed at the Institute for Solid State Physics, The University of Tokyo [1]. The photoelectrons were excited by 21.2-eV photons from a He lamp and were analyzed with a ScientaOmicron DA30-L analyzer. The sample temperature was set to 40K during the measurements.

Figure 1(b) shows the ARPES image of the transfer graphene on Si(111) around the K point. We find a Dirac-cone like band for which the spectral width is broadened due to the multi domain structure of the surface. The Dirac point is located at the binding energy of 0.2-0.3 eV. The doping level of the p-band is smaller than that of the graphene on SiC(0001) substrate [2]. In the present ARPES measurements, the spot size of our He lamp is 0.5 mm on the sample. We could observe a clear band image if we would use the excitation light with the spot size on the order of micrometers.

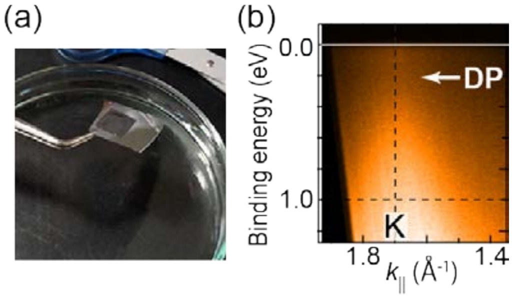

Fig. 1(a) Photo of the sacrificial-layer/graphene scooping on the Si(111) substrate. (b) ARPES image of the transfer graphene on Si(111).

REFERENCES

[1] K. Yaji *et al*., Rev. Sci. Instrum. **87**, 053111 (2016).
[2] K. Nakatsuji *et al*., Phys. Rev. B **82**, 045428 (2010).

STUDY ON ELECTRONIC STRUCTURES IN HALF-METALLIC FERROMAGNET CoS_2 BY HIGH-RESOLUTION SPIN- AND ANGLE-RESOLVED PHOTOEMISSION SPECTROSCOPY

Hirokazu Fujiwara[1], K. Terashima[2], T. Wakita[2], Y. Yano[1], W. Hosoda[1], N. Kataoka[1], A. Teruya[3], M. Kakihana[3], M. Hedo[4], T. Nakama[4], Y. Ōnuki[4], K. Yaji[5], A. Harasawa[5], K. Kuroda[5], S. Shin[5], Y. Muraoka[1,2], and T. Yokoya[1,2]

[1]*Graduate School of Natural Science and Technology, Okayama University, Okayama 700-8530, Japan*
[2]*Research Institute for Interdisciplinary Science, Okayama University, Okayama 700-8530, Japan*
[3]*Graduate School of Engineering and Science, University of the Ryukyus, Nishihara, Okinawa 903-0213, Japan*
[4]*Faculty of Science, University of the Ryukyus, Nishihara, Okinawa 903-0213, Japan*
[5]*Institute for Solid State Physics, The University of Tokyo, Kashiwa, Chiba 277-8581, Japan*

CoS_2 is a ferromagnetic metal whose ordered moment is reported to be approximately 0.9 μ_B/Co with an easy-axis along the [111] direction [1–3]. The ordered moment is close to 1 μ_B/Co in a low-spin state of Co^{2+} (configuration: $t_{2g}^6 e_g^1$), suggesting that CoS_2 has a half-metallic electronic structure including completely spin polarized e_g bands crossing the Fermi level (E_F). The half-metallicity has been also supported by theoretical band structure calculated within generalized gradient approximation (GGA) and experimental studies using de Haas–van Alphen (dHvA) effect [4,5]. On the other hand, the results of band calculation within local spin-density approximation (LSDA) and photoemission spectroscopy measurements indicated that CoS_2 has a "nearly" half-metallic electronic structure in which a bottom of the minority spin e_g band touches or slightly crosses E_F near the R point [6]. So far, comprehensive understanding of half-metallicity of CoS_2 has not been obtained. In this work, we performed high-resolution spin- and angle-resolved photoemission spectroscopy (SARPES) measurements on a high-quality CoS_2 single crystal in order to reveal the half-metallicity.

Single crystals of CoS_2 were synthesized by the vapor transport method,[3] and were used for SARPES measurements. Laser-based SARPES experiments were performed at the Institute for Solid State Physics, The University of Tokyo [7]. The *p*-polarized light with $h\nu$ = 6.994 eV was used to excite the photoelectrons. Photoelectrons were analyzed with a combination of a ScientaOmicron DA30L analyzer and a very-low-energy-electron-diffraction (VLEED) type spin detector. The energy and angular resolutions were set to 6 meV and 0.3° (corresponding to ~0.005 Å) for spin-integrated ARPES and 10 meV and 1° (corresponding to ~0.02 Å) for SARPES, respectively. Calibration of E_F for the samples was achieved using a gold reference. The data were taken at T = 40 K. Clean surfaces for all measurements were obtained by *in situ* cleaving of the samples.

Our high-resolution SARPES results are summarized in Fig. 1. By the 7-eV laser, we observed bands located at –1 eV, –0.5 eV, –50 meV, near E_F, and a dispersive hole band. The bands located around –1 eV are assigned to t_{2g} bands based on a photoemission spectroscopy study [6].

For the e_g bands located between –0.5 eV and E_F, we obtained the spin-polarized band structure clearly. We named the e_g bands as shown in Figs. 1 (a) and (d). At –0.5 eV, the SARPES intensity map for the majority spin bands has a clear structure corresponding to the α band, although that for the minority spin bands has no structure at –0.5 eV. In the same way, it is identified that the β band has the majority spin character. The result that the majority spin character of the α and β bands is consistent with the theoretical band structures.[4] On the other hand, the SARPES intensity map for the minority spin bands has clear band dispersion corresponding to the γ and δ bands.

Here, we discuss the half-metallicity of CoS_2. We observed both of the majority and minority spin bands crossing E_F, as shown in Fig. 1, providing spectroscopic evidence for 'normal' ferromagnetic metallicity, not half-metallicity, of CoS_2. This result is consistent with claims by a photoemission studies.[6] The non-half-metallicity is also supported by the fact that the ordered moment $\mu_s \sim 0.9\ \mu_B$/Co at 2 K[3] is not exactly $\mu_s = 1\ \mu_B$/Co which is the expected ordered moment when the e_g electrons are completely spin-polarized.

In summary, we performed high-resolution SARPES in order to reveal the electronic structure of ferromagnetic CoS_2. We observed t_{2g} bands and highly spin-polarized e_g bands. We observed a minority spin band crossing E_F, demonstrating that CoS_2 is not a half-metallic ferromagnet at least above 40 K. This report demonstrates that the high-resolution SARPES is a powerful tool to identify half-metallicity of theoretically proposed borderline half-metallic ferromagnets.

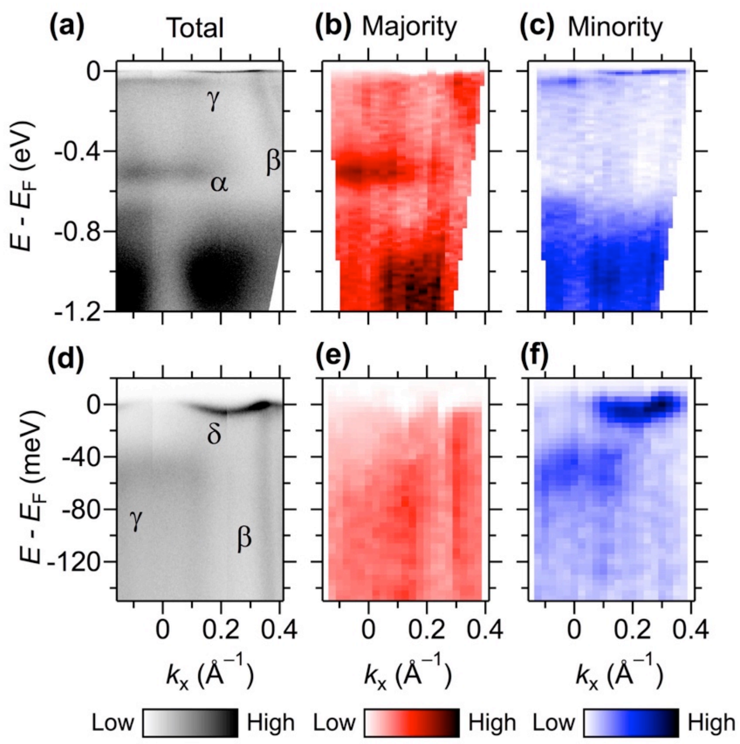

Fig. 1. (a)–(c) ARPES (a) and SARPES ((b) Majority spin bands; (c) Minority spin bands) intensity maps as a function of energy to E_F and k_x. **(d)–(f)** Same as (a)–(c) but measured in the vicinity of E_F.

REFERENCES

[1] H. S. Jarrett *et al.*, Phys. Rev. Lett. **21**, 617 (1968).
[2] H. Hiraka *et al.*, J. Phys. Soc. Jpn. **63**, 4573 (1994).
[3] A. Teruya *et al.*, J. Phys. Soc. Jpn. **85**, 064716 (2016).
[4] T. Shishidou *et al.*, Phys. Rev. B **64**, 180401(R) (2001).
[5] R. Yamamoto *et al.*, Phys. Rev. B **59**, 7793(R) (1999).
[6] Takahashi *et al.*, Phys. Rev. B **63**, 094415 (2001).
[7] K. Yaji *et al.*, Rev. Sci. Instrum. **87**, 053111 (2016).

ANGLE-RESOLVED PHOTOEMISSION SPECROSCOPY STUDY OF TYPE-II WEYL SEMIMETAL WTe2

Yuxuan Wan[1,2], Lihai Wang[3], Keisuke Koshiishi[1], Masahiro Suzuki[1], Jaewook Kim[4], Kenta Kuroda[2], Koichiro Yaji[2], Ryo Noguchi[2], Ayumi Harasawa[2], Shik Shin[2], Sang-Wook Cheong[3], Takeshi Kondo[2], Atsushi Fujimori[1]

[1] *Department of Physics, The School of Science, The University of Tokyo*

[2] *The Institute for Solid State Physics, The University of Tokyo*

[3] *The Center for Quantum Materials Synthesis, Rutgers University*

Introduction

So far, no example of a Weyl fermion has been observed in particle physics research. But some topological materials can host electrons behaving as Weyl fermions, which are called Weyl semimetals. In Weyl semimetals, there are bands crossing linearly near Weyl points, which means that electrons near Weyl points have zero-mass [1-3].

In some Weyl semimetals, the hole- and electron-like pockets touch each other at several Weyl points, and these kinds of Weyl semimetals are called type-II Weyl semimetals. Weyl points are topologically protected, and topological surface states (Fermi arcs) connected a pair of Weyl points with opposite chirality. WTe_2 is a kind of quasi-2D type-II Weyl semimetal. The space inversion symmetry along *c*-axis is broken, and the top and bottom surfaces are different. According to theoretical calculation, the surface electronic states of the two surfaces are different [4]. However, so far there is no experimental research showing the differences between the two surface states. On the other hand, some of Weyl points in WTe_2 locate above the Fermi level (E_F), which cannot be observed by angle-resolved photoemission spectroscopy directly, and neither the Fermi arcs above E_F have been observed. On the other hand, it is difficult to say whether the band structure is topological surface state or not by ARPES. Spin-ARPES can provide more evidence.

Experiment

The single crystals of WTe_2 with large domains were grown via the iodine vapor transport method [4]. We cut one piece of WTe_2 sample into two halves and turn one of them upside down. We cleaved them *in situ.*

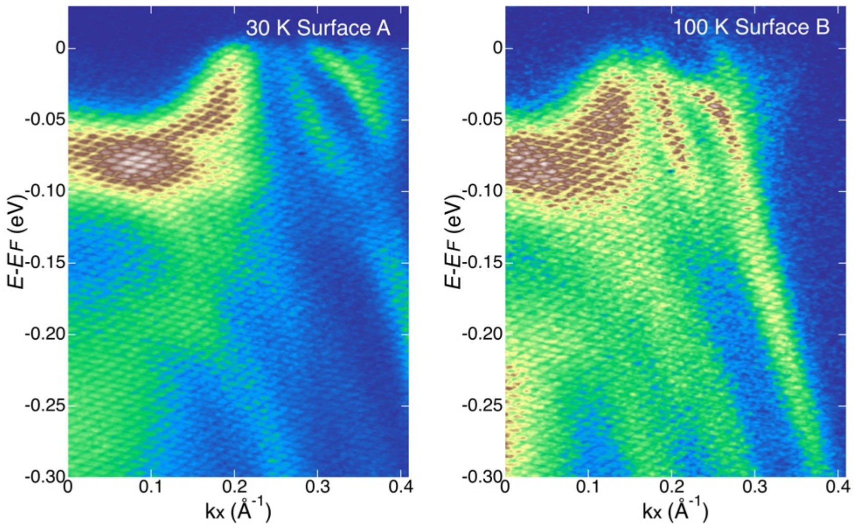

Fig.1 Band dispersion on surface A and B of WTe_2 measured by laser ARPES. The surface states connect the bulk electron- and hole-like pocket.

The experiment was carried out with the spin-resolved laser ARPES (SARPES) at ISSP, the University of Tokyo. The light source is 7 eV laser from KBBF crystal. We measured two kinds of surfaces of WTe_2: surface A and B. We used the 7 eV laser ARPES to map the energy contours and measured the band structures. To observe the topological Fermi arcs are surfaces states which connect hole and electron pockets, and parts of them are above the E_F, we measured the samples at a high temperature (over 150 K) which unoccupied states about 30 meV above E_F could be seen. SARPES measurements on candidate topological surface states were taken after the ARPES measurements.

Results

We measured two kinds of surfaces of WTe_2: surfaces A and B with 7 eV laser-ARPES. In Fig. 1, we can see the band structures where the surface state connected the hole- and electron-like bulk states on both surface A and B. The surface states of the opposite surfaces are supposed to be different.

Figure 2 and 3 show the SARPES results of the candidate topological surface states. For surface A (Fig. 2), clear spin reversal could be observed for the surface states for both x- and y-direction. The surface state for surface A is spin-polarized. For surface B (Fig.3), the spin-polarization along x-direction could be observed, but no clear evidence showing that the surface state on surface B is spin-polarized along y-direction.

We observed two kinds of surfaces of type-II Weyl semimetal WTe_2 with laser-ARPES. Clear surface states which connect the bulk hole- and electron-like pockets could be seen. By SARPES measurements, we found that the surface states are all spin-polarized, which is important evidence for that the observed surface states are topological Fermi arcs.

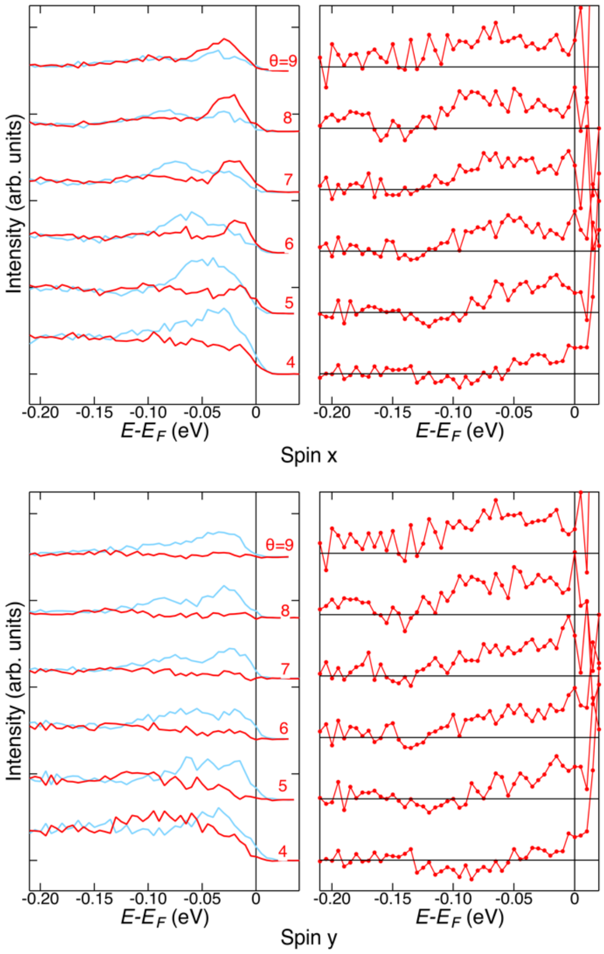

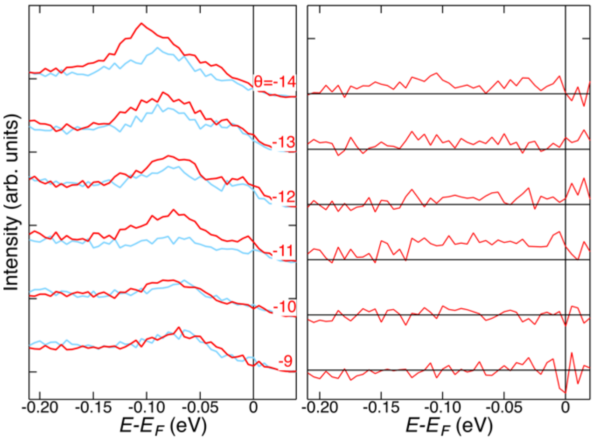

Fig.2 (Left)The spin-polarization along x- and y-direction on surface A of WTe_2.

Fig.3 (Right) The spin-polarization along x-direction on surface B of WTe_2.

REFERENCES

[1] A.Soluyanov *et al*. *Nature* 527.7579 (2015).
[2] Y.Wu *et al*., *Phy. Rev. B* 94, 121113(R) (2016).
[3] F.Y.Bruno *et al*., *Phy. Rev. B* 94, 121112(R) (2016)
[4] W.Zhang *et al*., *Phy. Rev. B* 96, 165125 (2017)

６．Staff

Director: SHIN Shik, Professor
KOMORI Fumio, Professor
HARADA Yoshihisa, Professor
MATSUDA Iwao, Associate Professor
WADATI Hiroki, Associate Professor
YAMAMOTO Susumu, Research Associate
YAJI Koichiro, Research Associate
MIYAWAKI Jun, Research Associate
HIRATA Yasuyuki, Research Associate
FUKUSHIMA Akiko, Technical Associate
HARASAWA Ayumi, Technical Associate
SHIBUYA Takashi, Technical Associate
KUDO Hirofumi, Technical Associate

Technical Assistant: FUJISAWA Masami
KOSEGAWA Yuka
ARAKI Mihoko

Secretary: AIHARA Yumiko
HARADA Misa
YOSHIZAWA Motoko
TSUTSUMI Yumiko
IKEDA Kuniko
HIROMOTO Chiho

Graduate Student: ITO Suguru
YAMAMOTO Kohei
IKEDA Keisuke
TSUKADA Tomoyuki
WATANABE Ryusuke
UGALINO Ralph John

Contract Researcher: OSHIMA Masaharu
TAKUBO Kou
CUI Yitao
AKADA Keishi
YAMAZOE Kosuke
YAMAGAMI Kohei
ZHANG Yujun
OHDAIRA Takeshi (2018.5~)
EL Moussaoui Souliman (2018.9~)

---Harima---

Paper

No.	Title	Authors	Journal	Vol	Page	Year
1	Operando measurement of single crystalline Li4Ti5O12 with octahedral-like morphology by microscopic X-ray photoelectron spectroscopy	Keishi Akada, Takaaki Sudayama, Daisuke Asakura, Hirokazu Kitaura, Naoka Nagamura, Koji Horiba, Masaharu Oshima, Eiji Hosono, and Yoshihisa Harada	J.Electron Spectrosc.Relat. Phenom.	233	64-68	2019
2	Operando measurement of single crystalline Li4Ti5O12 with octahedral-like morphology by microscopic X-ray photoelectron spectroscopy	Keishi Akada, Takaaki Sudayama, Daisuke Asakura, Hirokazu Kitaura, Naoka Nagamura, Koji Horiba, Masaharu Oshima, Eiji Hosono, and Yoshihisa Harada	J.Electron Spectrosc.Relat. Phenom.	233	64-68	2019
3	Semimetallicity of free-standing hydrogenated monolayer boron from MgB2	I. Tateishi, N. T. Cuong, C. A. S. Moura, M. Cameau, R. Ishibiki, A. Fujino, S. Okada, A. Yamamoto, M. Araki, S. Ito, S. Yamamoto, M. Niibe, T. Tokushima, D. E. Weibel, T. Kondo, M. Ogata, and I. Matsuda	Phys. Rev. Materials	3	024004 (1-8)	2019
4	Mass transport in the PdCu phase structures during hydrogen adsorption andabsorption studied by XPS under hydrogen atmosphere	Jiayi Tang, Susumu Yamamoto, Takanori Koitaya, Akitaka Yoshigoe, Takuma Tokunaga,Kozo Mukai, Iwao Matsuda, Jun Yoshinobu	Appl. Surf. Sci.	480	419-426	2019
5	Enhanced Photoresponsivity of Fullerene in the Presence of Phthalocyanine: A Time-Resolved X-ray Photoelectron Spectroscopy Study of Phthalocyanine/C60/TiO2(110)	Kenichi Ozawa, Susumu Yamamoto, Marie D'angelo, Yuto Natsui, Naoya Terashima, Kazuhiko Ma, and Iwao Matsuda	J. Phys. Chem. C	123	4388-4395	2019
6	Hydrogen adsorption and absorption on a Pd-Ag alloy surface studied using in-situ X-ray photoelectron spectroscopy under ultrahigh vacuum and ambient pressure	J. Tang, S. Yamamoto, T. Koitaya, Y. Yoshikura, K. Mukai, S. Yoshimoto, I. Matsuda, J. Yoshinobu	Appl. Surf. Sci.	463	1161-1167	2019
7	Site-sensitive X-ray photoelectron spectroscopy of Fe3O4 by photoelectron diffraction	Yusuke Hashimoto Munetaka Taguchi Shun Fukami Hiroki Momono Tomohiro Matsushita Hiroyuki Matsuda Fumihiko Matsui Hiroshi Daimon	Surface and Interface Analysis	51	115-119	2019
8	Operation Mechanism of GaN-based Transistors Elucidated by Element-Specific X-ray Nanospectroscopy	Keiichi Omika, Yasunori Tateno, Tsuyoshi Kouchi, Tsutomu Komatani, Seiji Yaegassi, Keiichi Yui, Ken Nakata, Naoka Nagamura, Masato Kotsugi, Koji Horiba, Masaharu Oshima, Maki Suemitsu & Hirokazu Fukidome	Scientific Reports	8	13268	2018
9	Monatomic Two-Dimensional Layers: Modern Experimental Approaches for Structure, Properties, and Industrial Use (Micro and Nano Technologies)	Iwao Matsuda	Elsevier		222 pages	2018
10	Femtosecond resonant magneto-optical Kerr effect measurement on an ultrathin magnetic film in a soft X-ray free electron laser	Sh. Yamamoto, Y. Kubota, K. Yamamoto, Y. Takahashi, K. Maruyama, Y. Suzuki, R. Hobara, M. Fujisawa, D. Oshima, S. Owada, T. Togashi, K. Tono, M. Yabashi, Y. Hirata, S. Yamamoto, M. Kotsugi, H. Wadati, T. Kato, S. Iwata, S. Shin, I. Matsuda1. Sh. Yamamoto, Y. Kubota, K. Yamamoto, Y. Takahashi, K. Maruyama, Y. Suzuki, R. Hobara, M. Fujisawa, D. Oshima, S. Owada, T. Togashi, K. Tono, M. Yabashi, Y. Hirata, S. Yamamoto, M. Kotsugi, H. Wadati, T. Kato, S. Iwata, S. Shin, I. Matsuda	JJAP	57	09TD02	2018
11	Interfacial carrier dynamics of graphene on SiC, traced by the full-range time-resolved core-level photoemission spectroscopy	T. Someya, H. Fukidome, N. Endo, K. Takahashi, S. Yamamoto, I. Matsuda	Appl. Phys. Lett.	113		2018
12	Probing the Valence Electronic Structure of Low-Spin Ferrous and Ferric Complexes Using 2p3d Resonant Inelastic X-ray Scattering (RIXS).	A. W. Hahn, B. E. Van Kuiken, V. G. Chilkuri, N. Levin, E. Bill, T. Weyhermüller, A. Nicolaou, J. Miyawaki, Y. Harada and S. DeBeer	Inorg. Chem.	57	9515–9530	2018
13	Electronic States of Quinones for Organic Energy Devices: The Effect of Molecular Structure on Electrochemical Characteristics	Naoka Nagamura, Ryosuke Taniki, Yuta Kitada, Asuna Masuda, Hiroaki Kobayashi, Nobuto Oka, and Itaru Honma	ACS Applied Energy Materials	1	3084-3092	
14	Effect of amino group protonation on the carboxyl group in aqueous glycine observed by O 1s X-ray emission spectroscopy.	Y. Horikawa, T. Tokushima, O. Takahashi, Y. Harada, A. Hiraya and S.Shin	Phys. Chem. Chem. Phys	20	23214-23221	2018

15	Enhancement of CO2 adsorption on oxygen-functionalized epitaxial graphene surface under near-ambient conditions	S. Yamamoto, K. Takeuchi, Y. Hamamoto, R.-Y.Liu, Y. Shiozawa, T. Koitaya, T. Someya, K. Tashima, H. Fukidome, K. Mukai, S. Yoshimoto, M.Suemitsu, Y. Morikawa, J. Yoshinobu and I.Matsuda	Phys. Chem. Chem. Phys	20	19532-19538	2018
16	Electronic Structure of Ce-Doped and -Undoped Nd2CuO4 Superconducting Thin Films Studied by Hard X-Ray Photoemission and Soft X-Ray Absorption Spectroscopy	M. Horio, Y. Krockenberger, K. Yamamoto, Y. Yokoyama, K. Takubo, Y. Hirata, S. Sakamoto, K. Koshiishi, A. Yasui, E. Ikenaga, S. Shin, H. Yamamoto, H. Wadati, and A. Fujimori	Phys. Rev. Lett.	120	257001 (1-6)	2018
17	Electronic States of Quinones for Organic Energy Devices: The Effect of Molecular Structure on Electrochemical Characteristics	Naoka Nagamura, Ryosuke Tanik, Yuta Kitad, Asuna Masuda, Hiroaki Kobayash, Nobuto Oka, and Itaru Honma	ACS Appl. Energy Mater	1	3084-3092	2018
18	Photoelectron Nano-spectroscopy of Reactive Ion Etching-Induced Damages to the Trench Sidewalls and Bottoms of 4H-SiC Trench-MOSFETs	Masaharu Oshima, Daisuke Mori, Aki Takigawa, Akihiko Otsuki, Naoka Nagamura, Shun Konno, Yoshinobu Takahashi, Masato Kotsugi, Hiroshi Nohira	e-Journal of Surface Science and Nanotechnology	16	257-261	2018
19	Element Selectivity in Second-Harmonic Generation of GaFeO3 by a Soft-X-Ray Free-Electron Laser	Sh. Yamamoto, T. Omi, H. Akai, Y. Kubota, Y. Takahashi, Y. Suzuki, Y. Hirata, K, Yamamoto, R. Yukawa, K. Horiba, H. Yumoto, T. Koyama, H. Ohashi, S. Owada, K. Tono, M. Yabashi, E. Shigemasa, S. Yamamoto, M. Kosugi, H. Wadati, H. Kumigashira, T. Arima, S. Shin, I. Matsuda	Phys. Rev. Lett.	120	223902 (1-5)	2018
20	Electronic Spectra of Iron-Sulfur Complexes Measured by 2p3d RIXS Spectroscopy	Benjamin E. Van Kuiken, Anselm W. Hahn, Brahamjot Nayyar, Christine E. Schiewer, Sonny C. Lee, Franc Meyer, Thomas Weyhermüller, Alessandro Nicolaou, Yi-Tao Cui, Jun Miyawaki, Yoshihisa Harada, and Serena DeBeer	Inorg. Chem.	57	7355–7361	2018
21	Tensile-Strain Dependent Spin States in Epitaxial LaCoO3 Thin Films	Y. Yokoyama, Y. Yamasaki, M. Taguchi, Y. Hirata, K. Takubo, J. Miyawaki, Y. Harada, D. Asakura, J. Fujioka, M. Nakamura, H. Daimon, M. Kawasaki, Y. Tokura and H. Wadati	Phys. Rev. Lett.	120	206402 (1-5)	2018
22	Alkali-metal induced band structure deformation investigated by angle-resolved photoemission spectroscopy and first-principles calculations	S. Ito, B. Feng, M. Arita, T. Someya, W.-C. Chen, A. Takayama, T. Iimori, H. Namatame, M. Taniguchi, C.-M. Cheng, S.-J. Tang, F. Komori, and I. Matsuda	Phys. Rev. B	97	155423 (1-8)	2018
23	Highly Reversible Oxygen-Redox Chemistry at 4.1 V in Na4/7−x[□1/7Mn6/7]O2 (□: Mn Vacancy)	Benoit Mortemard de Boisse Shin-ichi Nishimura Eriko Watanabe Laura Lander Akihisa Tsuchimoto Jun Kikkawa Eiichi Kobayashi Daisuke Asakura Masashi Okubo Atsuo Yamada	Advanced Energy Materials	8	1800409	2018
24	Correlation between Photocatalytic Activity and Carrier Lifetime: Acetic Acid on Single-Crystal Surfaces of Anatase and Rutile TiO2	K. Ozawa, S. Yamamoto, R. Yukawa, R.-Y. Liu, N. Terashima, Y. Natsui, H. Kato, K. Mase, I. Matsuda	J. Phys. Chem C	122	9562-9569	2018
25	Time-Resolved Photoelectron Spectroscopy	Iwao Matsuda	Encyclopedia of Interfacial Chemistry: Surface Science and Electrochemistry		8 pages	2017
26	Direct observation of Cr3+ 3d states in ruby: towards experimental mechanistic evidence of metal chemistry	Myrtille O.J.Y. Hunault, Yoshihisa Harada, Jun Miyawaki, Jian Wang, Andries Meijerink, Frank M.F de Groot, and Matti M. van Schooneveld	J. Phys. Chem. A	122	4399-4413	2018
27	Resonant Inelastic X-ray Scattering	Yoshihisa Harada	Sync. Rad. News	31	2	2018
28	Commensurate versus incommensurate charge ordering near the superconducting dome in Ir1−xPtxTe2 revealed by resonant x-ray scattering	K. Takubo, K. Yamamoto, Y. Hirata, H. Wadati, T. Mizokawa, R. Sutarto, F. He, K. Ishii, Y. Yamasaki, H. Nakao, Y. Murakami, G. Matsuo, H. Ishii, M. Kobayashi, K. Kudo, and M. Nohara	Phys. Rev. B	97	205142	2018
29	Controlling the surface photovoltage on WSe2 by surface chemical modification	R.-Y. Liu, K. Ozawa, N. Terashima, Y. Natsui, B. Feng, S. Ito, W.-C. Chen, C.-M. Cheng, S. Yamamoto, H. Kato, T.-C. Chiang, I. Matsuda	Appl. Phys. Lett.	112	211603-1,-5	2018
30	Resonant Inelastic X-Ray Scattering	Yoshihisa Harada	Compendium of Surface and Interface Analysis		531-537	2018
31	Time-Resolved Photoelectron Spectroscopy	Iwao Matsuda	Compendium of Surface and Interface Analysis		8 pages	2018

32	Thickness dependence and dimensionality effects of charge and magnetic orderings in La1/3Sr2/3FeO3 thin films	K. Yamamoto, Y. Hirata, M. Horio, Y. Yokoyama, K. Takubo, M. Minohara, H. Kumigashira, Y. Yamasaki, H. Nakao, Y. Murakami, A. Fujimori, H. Wadati	Phys. Rev. B	97	075134 (1-6)	2017
33	Single-Layer Dual Germanene Phases on Ag (111)	C.H.Lin, A.Huang, W.W.Pai, W.C.Chen, T.R.Chang, R.Yukawa, C.M.Cheng, C.Y.Mou, I.Matsuda, T.C.Chiang, H.T.Jeng, S.J.Tang	Phys. Rev. Materials	2	024003 (1-8)	2018
34	Peculiar bonding associated with atomic doping and hidden honeycombs in borophene	Chi-Cheng Lee, Baojie Feng, Marie D'angelo, Ryu Yukawa, Ro-Ya Liu, Takahiro Kondo, Hiroshi Kumigashira, Iwao Matsuda, and Taisuke Ozaki,	Phys. Rev. B	97	075430 (1-5)	2018
35	A table-top formation of bilayer quasi-free-standing epitaxial-graphene on SiC(0001) by microwave annealing in air	K.S.Kim, G.H.Park, H.Fukidome, T.Someya, T.Iimori, F.Komori, I.Matsuda, M.Suemitsu	Carbon	130	792-798	2018
36	Strong Hydrogen Bonds at the Interface between Proton-Donating and -Accepting Self-Assembled Monolayers on Au(111)	H.S.Kato, S.Yoshimoto, A.Ueda, S.Yamamoto, Y.Kanemitsu, M.Tachikawa, H.Mori, J.Yoshinobu, I.Matsuda	Langmuir	34	2189-2197	2018
37	Electronic Structure and Magnetic Properties of the Half-Metallic Ferrimagnet Mn2VAl Probed by Soft X-ray Spectroscopies	K. Nagai, H. Fujiwara, H. Aratani, S. Fujioka, H. Yomosa, Y. Nakatani, T. Kiss, A. Sekiyama, F. Kuroda, H. Fujii, T. Oguchi, A. Tanaka, J. Miyawaki, Y. Harada, Y. Takeda, Y. Saitoh, S. Suga, and R. Y. Umetsu	Phys. Rev. B	97	35143	2018
38	Raman and fuorescence-like components in resonant inelastic x-ray scattering on LaAlO3/SrTiO3 heterostructures	F. Pfaff, H. Fujiwara, G. Berner, A. Yamasaki, H. Niwa, A. Gloskovskii, W. Drube, O. Kirilmaz, A. Sekiyama, J. Miyawaki, Y. Harada, S. Suga, M. Sing, and R. Claessen	Phys. Rev. B	97	035110	2018

---E-Labo---

Paper

No	Title	Authors	Journal	Vol.	Page	Year
1	Surface electronic states of Au-induced nanowires on Ge(001)	Koichiro Yaji, Ryu Yukawa, Sunghun Kim, Yoshiyuki Ohtsubo, Patrick Le Fèvre, François Bertran, Amina Taleb-Ibrahimi, Iwao Matsuda, Kan Nakatsuji, Shik Shin and Fumio Komori	J. Phys.: Condens. Matter	30	075001	2018
2	Optical spin control of photoexcited electrons using a polarization-controllable laser (in Japanese)	Koichiro Yaji, Kenta Kuroda, Fumio Komori, Shik Shin	Journal of Japan Laser Processing Society	25	39	2018
3	Observation of topological superconductivity on the surface of iron-based superconductor	Peng Zhang, Koichiro Yaji, Takahiro Hashimoto, Yuichi Ota, Takeshi Kondo, Kozo Okazaki, Zhijun Wang, Jinsheng Wen, G. D. Gu, Hong Ding, and Shik Shin	Science	360	182	2018
4	Optical spin control in photoexcitation process revealed by laser-based spin- and angle-resolved photoelectron spectroscopy (in Japanese)	Koichiro Yaji, Kenta Kuroda, Fumio Komori, Shik Shin	Japanese Journal of Optics	47	142	2018
5	Experimental Methods for Spin- and Angle-Resolved Photoemission Spectroscopy Combined with Polarization-Variable Laser (Video Jounal)	Kenta Kuroda, Koichiro Yaji, Ayumi Harasawa, Ryo Noguchi, Takeshi Kondo, Fumio Komori, Shik Shin	J. Vis. Exp.	136	e57090	2018
6	Rashba spin splitting of L-gap surface states on Ag(111) and Cu(111)	Koichiro Yaji, Ayumi Harasawa, Kenta Kuroda, Ronghan Li, Binghai Yan, Fumio Komori, and Shik Shin	Phys. Rev. B	98	041404(R)	2018
7	Giant Rashba splitting of quasi-one-dimensional surface states on Bi/InAs(110)-(2×1)	Takuto Nakamura, Yoshiyuki Ohtsubo, Yuki Yamashita, Shin-ichiro Ideta, Kiyohisa Tanaka, Koichiro Yaji, Ayumi Harasawa, Shik Shin, Fumio Komori, Ryu Yukawa, Koji Horiba, Hiroshi Kumigashira, and Shin-ichi Kimura	Phys. Rev. B	98	075431	2018
8	Origins of Thermal Spin Depolarization in Half-Metallic Ferromagnet CrO_2	Hirokazu Fujiwara, Kensei Terashima, Masanori Sunagawa, Yuko Yano, Takanobu Nagayama, Tetsushi Fukura, Fumiya Yoshii, Yuka Matsuura, Makoto Ogata, Takanori Wakita, Koichiro Yaji, Ayumi Harasawa, Kenta Kuroda, Shik Shin, Koji Horiba, Hiroshi Kumigashira, Yuji Muraoka, and Takayoshi Yokoya	Phys. Rev. Lett.	121	2572201	2018